

Calculation of oscillation probabilities
of atmospheric neutrinos
with additional sterile mass states
using nuCraft

Denise Hellwig and Marius Wallraff

IceCube Internal Report

March 2013

This internal report deals with the calculation and analysis of signatures of sterile neutrinos with squared mass differences of about 1 GeV^2 . In large parts it is a translation of Denise Hellwig's bachelor thesis, available in German at <http://www.physik.rwth-aachen.de/>. The introductory chapters dealing with astrophysics and IceCube have been skipped in this translation, and the chapter regarding the calculation of weights with nuCraft has been extended by Marius Wallraff.

Contents

1	Theory	1
1.1	Neutrino oscillations	1
1.1.1	In vacuum	1
1.1.2	In matter	3
1.1.3	With CP violation	4
1.2	Mass hierarchies and sterile parameters	5
2	Calculation of the oscillation probabilities	7
2.1	Density profile	7
2.2	nuCraft	8
2.3	Conventions used in this work	10
3	3+1 model	12
3.1	$\sin^2(\theta_{14}) = \sin^2(\theta_{24}) = \sin^2(\theta_{34}) = 0$	12
3.2	$\sin^2(\theta_{24}) \neq 0$, where $\sin^2(\theta_{34}) = \sin^2(\theta_{14}) = 0$	14
3.3	$\sin^2(\theta_{34}) \neq 0$, where $\sin^2(\theta_{24}) = \sin^2(\theta_{14}) = 0$	21
3.4	$\sin^2(\theta_{24}), \sin^2(\theta_{34}) \neq 0$, where $\sin^2(\theta_{14}) = 0$	21
3.5	$\sin^2(\theta_{24}), \sin^2(\theta_{34}), \sin^2(\theta_{14}) \neq 0$	34
3.6	CP-violating phases	35
3.7	Errors on the known parameters	41
4	3+2 model	42
4.1	Impact of θ_{45}	42
4.2	Impact of the relative sign of Δm_{41}^2 and Δm_{51}^2	42
4.2.1	$\sin^2(\theta_{24}) = \sin^2(\theta_{25}) \neq 0, \sin^2(\theta_{ij}) = 0$ with $i = 1, 3, j = 4, 5$	42
4.2.2	General unsymmetrical case	47
4.3	Impact of the ratio $\Delta m_{41}^2 \div \Delta m_{51}^2$	52
4.3.1	$\Delta m_{41}^2, \Delta m_{51}^2 > 0$ or $\Delta m_{41}^2, \Delta m_{51}^2 < 0$	52
4.3.2	$(\Delta m_{41}^2 < 0 \wedge \Delta m_{51}^2 > 0)$ or $(\Delta m_{41}^2 > 0 \wedge \Delta m_{51}^2 < 0)$	56
4.4	Impact of the angle distribution	57
4.4.1	$\Delta m_{41}^2, \Delta m_{51}^2 > 0$ or $\Delta m_{41}^2, \Delta m_{51}^2 < 0$	57
4.4.2	$(\Delta m_{41}^2 < 0 \wedge \Delta m_{51}^2 > 0)$ or $(\Delta m_{41}^2 > 0 \wedge \Delta m_{51}^2 < 0)$	61
5	Conclusion	63
5.1	3+1 model	63
5.2	3+2 model	64

A	3+1 model	65
A.1	$\sin^2(\theta_{14}) = \sin^2(\theta_{24}) = \sin^2(\theta_{34}) = 0$	65
A.2	$\sin^2(\theta_{24}) \neq 0$, where $\sin^2(\theta_{34}) = \sin^2(\theta_{14}) = 0$	66
A.3	$\sin^2(\theta_{34}) \neq 0$, where $\sin^2(\theta_{24}) = \sin^2(\theta_{14}) = 0$	71
A.4	$\sin^2(\theta_{24}), \sin^2(\theta_{34}) \neq 0$, where $\sin^2(\theta_{14}) = 0$	72
A.5	$\sin^2(\theta_{24}), \sin^2(\theta_{34}), \sin^2(\theta_{14}) \neq 0$	78
A.6	CP-violating phases	81
B	3+2 model	86
B.1	Impact of the relative sign of Δm_{41}^2 and Δm_{51}^2	86
B.2	Impact of the ratio $\Delta m_{41}^2 \div \Delta m_{51}^2$	95
B.3	Impact of the angle distribution	96
	Bibliography	II

icecube/201303001-v2

Chapter 1

Theory

1.1 Neutrino oscillations

1.1.1 In vacuum

Flavor states of neutrinos are defined by their behavior under the weak interaction. Since sterile neutrinos do not take part in it, they actually do not have a flavor state. If a flavor state is associated with sterile neutrinos in this work, it is their state in the base the known flavor states exist.

The flavor states of the known neutrinos are not necessarily identical with their mass eigenstates, but in general are a linear combination of the mass eigenstates instead. One can express the flavor eigenstates by the mass eigenstates by making use of a mixing matrix:

$$|\nu_{\text{Flavor}}\rangle = U |\nu_{\text{Mass}}\rangle . \quad (1.1)$$

For this, U has to be an element of the special unitary group $SU(N)$. $SU(N)$ is defined by $SU(N) = \{ U \in \mathbb{C}^{(N \times N)} \mid U \cdot U^\dagger \equiv U \cdot U^{*\text{T}} = \mathbf{1} \text{ (unitarity)} \wedge \det(U) = 1 \}$. Applying these definitions for example on the 3+1 model yields:

$$|\nu_{\text{Flavor}}\rangle = \begin{pmatrix} \nu_e \\ \nu_\mu \\ \nu_\tau \\ \nu_s \end{pmatrix} \quad \text{und} \quad |\nu_{\text{Mass}}\rangle = \begin{pmatrix} \nu_1 \\ \nu_2 \\ \nu_3 \\ \nu_4 \end{pmatrix} . \quad (1.2)$$

The extension to more dimensions is done by adding additional sterile states. The mentioned matrix U is named Pontecorvo-Maki-Nakagawa-Sakata matrix, or briefly PMNS matrix [1]. For now, possible CP violation phases will be neglected; they will be introduced in section 1.1.3. Due to the unitarity, U has only $\frac{N(N-1)}{2}$ free parameters for N neutrino types. Usually, the PMNS matrix is represented by a product of rotation matrices like

$$R_{13} := R_{13}(\theta_{13}) = \begin{pmatrix} \cos(\theta_{13}) & 0 & \sin(\theta_{13}) & 0 \\ 0 & 1 & 0 & 0 \\ -\sin(\theta_{13}) & 0 & \cos(\theta_{13}) & 0 \\ 0 & 0 & 0 & 1 \end{pmatrix} , \quad (1.3)$$

here again exemplary for four neutrino types. The generalization is given by $(R_{ij})_{mn} = \delta_{mn}(1 - (1 - \cos(\theta_{ij}) \cdot (\delta_{im} + \delta_{jm}))) + \sin(\theta_{ij}(\delta_{mi} - \delta_{nj}))$. With this choice, the required conditions are fulfilled. There are as many mixing angles as free parameters of the matrix.

Because rotation matrices in general do not commute, many possibilities for equivalent parametrization exist [2]. Therefore it is important to declare the parametrization of the PMNS matrix.

The time evolution of the states is given by

$$i \frac{d}{dt} |\nu(t)\rangle = H |\nu(t)\rangle \quad , \quad (1.4)$$

where $\hbar = c = 1$ [3]. In the mass base the Hamiltonian H is diagonal and can be evolved to

$$H_{ii} = \sqrt{p^2 + m_i^2} \approx E_\nu + \frac{m_i^2}{2E_\nu} \quad (1.5)$$

[3], because $p \gg m_i$ applies and therefore also $p_i \approx p_j \approx p$. E_ν is the neutrino energy. The momentum p is irrelevant for the transition probability $|\langle \nu | \nu' \rangle|$ because it just leads to a global phase. If we use $x \approx c \cdot t$, we get

$$i \frac{d}{dx} |\nu_{\text{mass}}\rangle = \frac{1}{2E_\nu} \cdot M |\nu_{\text{mass}}\rangle \quad . \quad (1.6)$$

Here, M is a diagonal matrix, its entries are the squares of the masses ($(M)_{ij} = \delta_{ij} m_i^2$). Alternatively, the parametrization $(M)_{ii} = m_i^2 - m_1^2$ can be chosen, because all parts that are proportional to the identity matrix just change the global phase. Therefore, the absolute mass scale does not affect the oscillation probabilities. The notation

$$\Delta m_{ji}^2 := m_j^2 - m_i^2 \quad (1.7)$$

is common.

In order to get the time evolution in the flavor base, we have to make the transformation

$$\tilde{M} = U \cdot M \cdot U^\dagger \quad . \quad (1.8)$$

This results in

$$i \frac{d}{dx} |\nu_{\text{flavor}}\rangle = \frac{1}{2E_\nu} \cdot \tilde{M} |\nu_{\text{flavor}}\rangle \quad . \quad (1.9)$$

The transition probability $P(\alpha \rightarrow \beta)$ of the flavor states α and β between the starting point and the point \vec{x} can be calculated by

$$P(\alpha \rightarrow \beta) = |\langle \nu_\alpha(\vec{0}) | \nu_\beta(\vec{x}) \rangle| \quad . \quad (1.10)$$

In case of two flavors and $\alpha \neq \beta$ [3],

$$P(\beta \rightarrow \alpha) = \sin^2(2\theta_{\beta\alpha}) \cdot \sin^2 \left(1.267 \frac{L \Delta m_{\beta\alpha}^2}{E_\nu} \frac{\text{GeV}}{\text{km eV}^2} \right) \quad , \quad (1.11)$$

where E is the energy of the neutrinos and L is the path length through the Earth. Due to the factor of $\sin^2(2\theta_{\alpha\beta})$, large effects are not possible in vacuum for small mixing angles. Independent of the number of states, there is no difference between particles and antiparticles. Overall – in vacuum as well as in matter – particle number preservation applies:

$$\sum_{k=1}^N P(\alpha_j \rightarrow \alpha_k) = 1 \quad . \quad (1.12)$$

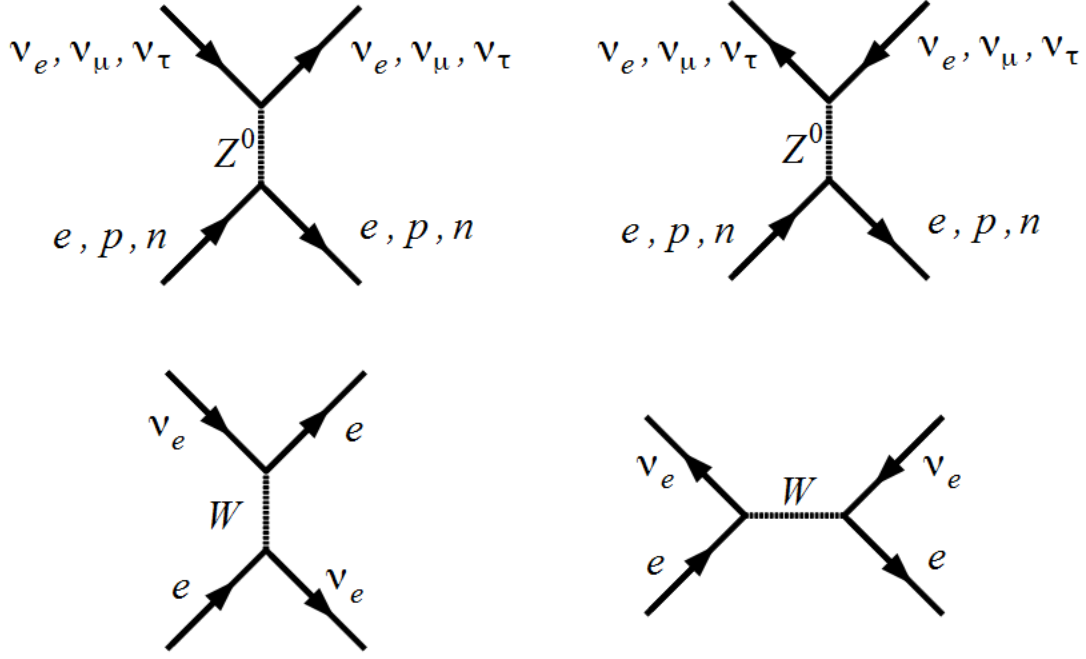


Figure 1.1: Feynmann graphs for the interaction possibilities of the different flavor states; timescale from the left to the right

1.1.2 In matter

Neutrinos can interact with matter if they move through it. This results in the so called matter effects [1]. (1.9) has to be modified to [4]

$$i \frac{d}{dx} |\nu_{\text{Flavor}}\rangle = \frac{1}{2E_\nu} \cdot (\tilde{M} + A) |\nu_{\text{Flavor}}\rangle \quad . \quad (1.13)$$

A has entries on the main diagonal to take into account the possibilities of the neutrino types to interact with matter. Sterile neutrinos do not interact with it per definition. Fig. 1.1 demonstrates the interaction possibilities of the known states. All conventional flavors are able to exchange Z^0 bosons with matter. This causes coherent forward scattering. Additionally, electron neutrinos (and electron antineutrinos) are able to interact with matter by exchange of W^\pm bosons. As already explained above, terms that are proportional to the identity matrix do not change the oscillation probabilities. For this reason

$$A = \text{diag}(A_{CC}, 0, 0, -A_{NC}, -A_{NC}, \dots) \quad (1.14)$$

can be chosen [5]. The illustrative meaning of A is that of an induced squared mass [5] [4]. It can be shown that for non-electron neutrinos and antineutrinos, the squared masses induced by electrons and protons cancel out each other and only the terms induced by the neutron number density remain. Therefore,

$$A_{CC} = \pm 2\sqrt{2}G_F\rho N_A Y_e E_\nu \quad \text{and} \quad A_{NC} = \mp \sqrt{2}G_F\rho N_A Y_n E_\nu \quad (1.15)$$

applies [5], where ρ is the density of the matter and $Y_e = Y_p$ the electron fraction that equals the proton fraction. $Y_n = 1 - Y_e$ is the neutron fraction, G_F the Fermi constant,

and N_A the Avogadro number. The upper sign holds for particles, the lower sign for antiparticles. Due to the unequal signs in (1.15), the effects are no longer symmetric in particles and antiparticles.

In matter, resonances are possible even for very small mixing angles. To illustrate this, effective mixing parameters are introduced frequently at this point. Expressed by these new *matter parameters*, (1.13) has the same pattern as (1.9). The matter parameters solve the equation

$$U \cdot M \cdot U^\dagger + A = U_{\text{Mat}} \cdot M_{\text{Mat}} \cdot U_{\text{Mat}}^\dagger \quad , \quad (1.16)$$

where M_{Mat} originates from M by the replacement $\Delta m_{ji}^2 \rightarrow \Delta m_{ji,\text{Mat}}^2$. The mixing angles can be transformed analogously.

Provided that the situation can be described as a two-flavor oscillation [5]:

$$(\Delta m_{ji,\text{Mat}}^2) = \sqrt{(\Delta m_{ji}^2 \cos(2\theta_{ij}) - A_M)^2 + (\Delta m_{ji}^2 \sin(2\theta_{ij}))^2} \quad , \quad (1.17)$$

$$\sin(2\theta_{ij,\text{Mat}}) = \sin(2\theta_{ij}) \frac{\Delta m_{ji}^2}{\Delta m_{ji,\text{Mat}}^2} \quad , \quad (1.18)$$

where [5]

$$A_M = A_{ii} - A_{jj} \quad . \quad (1.19)$$

Maximum resonance for the transition $i \rightarrow j$ occurs under the condition $\sin(2\theta_{ij,\text{Mat}}) = 1$. Using (1.18), this can be rewritten as

$$A_M = \Delta m_{ji}^2 \cos(2\theta_{ij}) \quad . \quad (1.20)$$

This condition can only be fulfilled if the signs on both sides are equal, so there is a resonance either in the particle or in the antiparticle channel. Because of $A_M \sim E_\nu$ for constant density, only a single resonance energy $E_{\nu,\text{res}} \sim \Delta m_{ji}^2$ exists in this case. Especially with $\theta_{ij} \rightarrow \theta_{ij,\text{Mat}}$ and $\Delta m_{ji}^2 \rightarrow \Delta m_{ji,\text{Mat}}^2$ for constant densities, the transition probabilities follow the same pattern as in vacuum. Equation (1.11) is applicable.

1.1.3 With CP violation

If the CP invariance is not kept, the parametrization of the PMNS matrix alters. The PDG standard representation for the three known flavors arises in this case as [1]:

$$\begin{aligned} U &= R_{23}(\theta_{23}, 0) \cdot R_{13}(\theta_{13}, \delta) \cdot R_{12}(\theta_{12}, 0) \cdot V(e^{i \cdot 0.5 \cdot \alpha_1}, e^{i \cdot 0.5 \cdot \alpha_1}) \\ &= \begin{pmatrix} 1 & 0 & 0 \\ 0 & c_{23} & s_{23} \\ 0 & -s_{23} & c_{23} \end{pmatrix} \begin{pmatrix} c_{13} & 0 & s_{13}e^{i\delta} \\ 0 & 1 & 0 \\ -s_{13}e^{-i\delta} & 0 & c_{13} \end{pmatrix} \\ &\quad \begin{pmatrix} c_{12} & s_{12} & 0 \\ -s_{12} & c_{12} & 0 \\ 0 & 0 & 1 \end{pmatrix} \begin{pmatrix} e^{i \cdot 0.5 \cdot \alpha_1} & 0 & 0 \\ 0 & e^{i \cdot 0.5 \cdot \alpha_2} & 0 \\ 0 & 0 & 1 \end{pmatrix} . \end{aligned} \quad (1.21)$$

From here on, the following abbreviations will be used

$$s_{ij} = \sin(\theta_{ij}) \quad \text{and} \quad c_{ij} = \cos(\theta_{ij}) \quad . \quad (1.22)$$

The evolution of the states is still given by (1.13). $\delta \neq 0$ is only possible if neutrinos are Dirac fermions, and $\alpha_1, \alpha_2 \neq 0$ only if they are Majorana fermions. If the CP invariance

is kept, all phases vanish. Whether neutrinos are Dirac or Majorana fermions is not clear yet.

Majorana particles are their own antiparticles. For neutrinos this means that it is possible to transform them into antiparticles regarding the weak interaction by stopping and then boosting them in the opposite direction, because only left-handed particles and right-handed antiparticles take part in the weak interaction. In case of Dirac fermions, this produces right-handed particles that do not interact weakly. The Majorana phases do not modify the matrix \tilde{M} , because diagonal matrices commute with other diagonal matrices.

In the following, only Dirac phases will be considered. Per redefinition of global phases, the parametrization can be constructed in such a way that it just contains

$$N_\delta = \frac{(N-1)(N-2)}{2} \quad (1.23)$$

phases for N neutrino types [1]. There are other ways to insert them [2], but it is advisable to use the PDG convention. Especially every construction of a mixing matrix that deals with more than three flavors should pass into the PDG convention for three flavors, if all unconventional mixing angles are set to zero.

1.2 Mass hierarchies and sterile parameters

To explain the LSND and MiniBooNE data and at the same time stay consistent with well-measured conventional oscillation parameters, mass-squared differences of about 1 eV are needed (more precise s. e.g. [6]). Generally $\Delta m_{21}^2 > 0$ is established, but the sign of Δm_{32}^2 is unclear [1]. Any signs of Δm_{i1}^2 with $i > 2$ are possible as long as this does not lead to a negative mass. The upper mass limit by tritium decay is $m_{\bar{\nu}_e} \lesssim 2 \text{ eV}$ [7]. Considering the results of oscillation experiments,

$$m_{\bar{\nu}_e} \approx m_{1,2,3} \lesssim 2 \text{ eV} \quad (1.24)$$

follows. Depending on experiment and model the limit can differ [1]. So sterile states in the eV range can be either heavier or lighter than the known flavor states. Fig. 1.2 shows all possible mass hierarchies in the 3+1 model. A convention how to include the n sterile states into the mathematical description is needed, because there are many ways to arrange the sterile states among the known states in the state vector and the PMNS matrix, and in general, these various constructions are not equivalent, because the matrices R_{ij} do not commute in general. W.l.o.g., $|m_{i1}|^2 < |m_{j1}|^2$ for $i < j$ is assumed. This definition is consistent with the PDG convention for three known states and will be motivated in chapter 4.

To not violate current exclusion limits, the mixing angles of the sterile states must be very small (s. [6]). In this work, large mixing angles at the boundary of the permitted values are presented for demonstration reasons, because the effects can be transferred to smaller values.

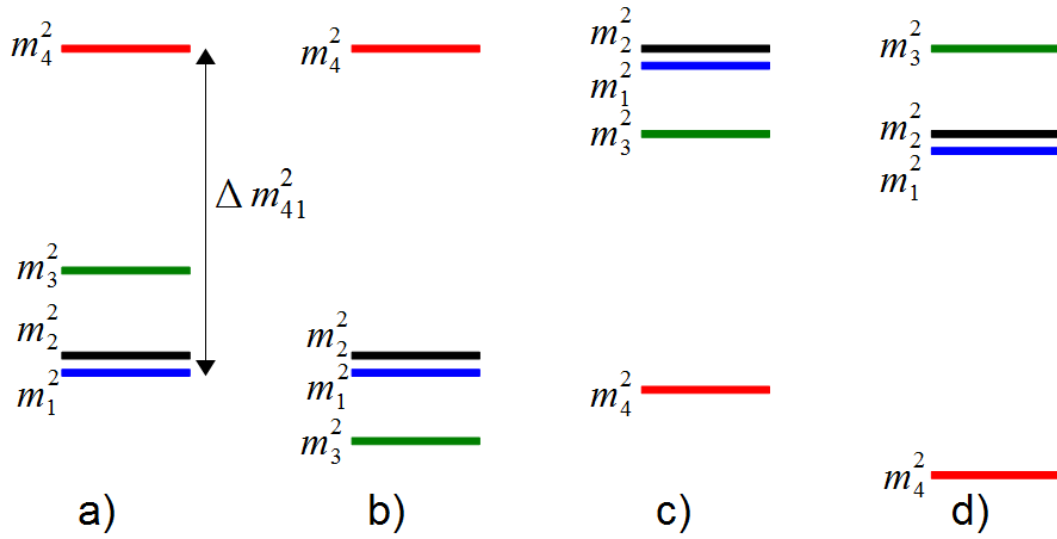


Figure 1.2: Possible mass hierarchies in the 3+1 model (not true to scale)
 a): $\Delta m_{41}^2, \Delta m_{32}^2 > 0$; b): $\Delta m_{41}^2 > 0, \Delta m_{32}^2 < 0$; c): $\Delta m_{41}^2, \Delta m_{32}^2 < 0$;
 d): $\Delta m_{41}^2 < 0, \Delta m_{32}^2 > 0$

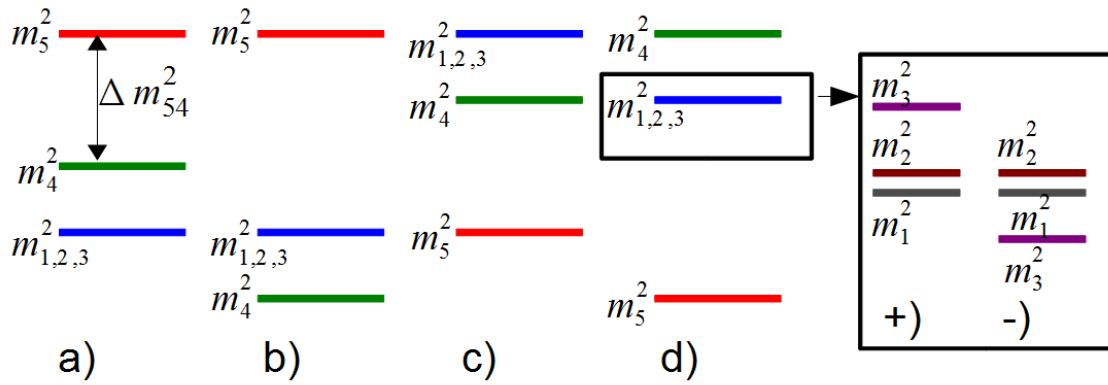


Figure 1.3: Possible mass-hierarchies in the 3+2 model (not true to scale)
 a): $\Delta m_{41}^2, \Delta m_{51}^2 > 0$; b): $\Delta m_{51}^2 > 0, \Delta m_{41}^2 < 0$; c): $\Delta m_{51}^2, \Delta m_{41}^2 < 0$;
 d): $\Delta m_{51}^2 < 0, \Delta m_{41}^2 > 0$; each with +): $\Delta m_{32}^2 > 0$; -): $\Delta m_{32}^2 < 0$

Chapter 2

Calculation of the oscillation probabilities

2.1 Density profile

The density of the matter along the neutrino trajectory is needed for the calculation of the oscillation probabilities since it enters in (1.15). In this work, the PREM profile has been taken as a basis for the density distribution. PREM (*Preliminary Reference Earth Model*) is a frequently used model of the Earth. It was published in 1981 by Adam M. Dziewonski and Don L. Anderson. The PREM profile describes the Earth as a radially symmetric sphere with a radius of 6371 km. Besides the data for the mass density it also contains data for seismic velocities inside the Earth among others. The Earth is divided into nine zones. The main ones are the inner core, the outer core, the mantle, the crust, and the ocean [8]. Fig. 2.1 shows the mass density ρ in dependence of the radius of the Earth R .

There is a significant jump in the density at about 3480 km. At this point the core ends and the mantle begins, and with this, the elementary composition of the Earth changes dramatically. As shown in Sec. 1.1.2, the relevant quantities are the electron and neutron number densities instead of the mass density given by PREM. Hence, the Earth was divided in two regions, $R < 3480$ km and $R \geq 3480$ km. The core mainly consists of iron ($\approx 80\%$) and nickel ($\approx 10\%$) with traces of lighter elements such as oxygen, silicon, and possibly heavier elements such as gold and platinum [9]. On average, $Y_e \approx 0.47$. The main elements in the outer region are oxygen ($\approx 45\%$), silicon ($\approx 22\%$), and magnesium ($\approx 23\%$) [9], which results in $Y_e \approx 0.5$.

Originally, the PREM mass density is given as a piecewise polynomial function. The data used in this work is obtained from a piecewise linear interpolation between points sampled from these polynomials [10]. These points are marked in fig. 2.1, where two more points with a density of $\rho = 0$ were added in order to describe the atmosphere.

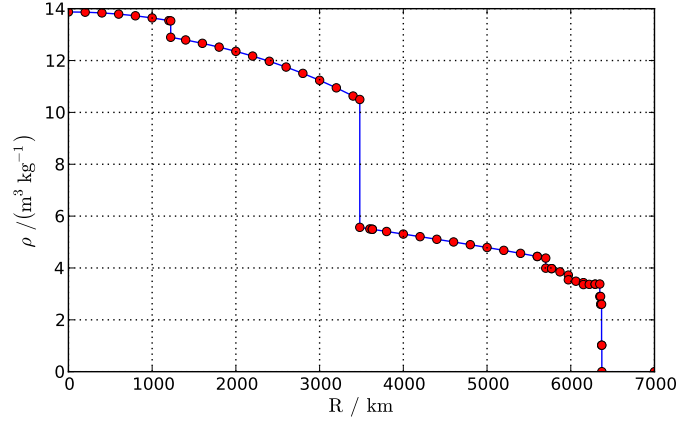


Figure 2.1: Mass density distribution in the PREM profile

2.2 nuCraft

The program which was used to calculate the oscillation probabilities is the Python tool *nuCraft*, created by Marius Wallraff. It allows for the calculation of oscillation probabilities of neutrinos with an arbitrary number of flavors, including sterile neutrinos. It relies on NumPy [11] and SciPy [12] and employs a SciPy wrapper around the algorithm ZVODE [13] to numerically solve the Schrödinger equation (1.13). The calculation of the transition probabilities follows by using (1.10). In its development, high priority is given to the accuracy and precision of the results as well as to easy and flexible usage and reasonable CPU requirements.

The tool can solve the Schrödinger equation in either the flavor base ((1.13)) or in the interaction base, in which vacuum oscillations are represented by a constant function:

$$|\tilde{\nu}\rangle = e^{i\tilde{M}t} |\nu_{\text{Flavor}}\rangle \quad (2.1)$$

$$\tilde{A} = e^{i\tilde{M}t} A e^{-i\tilde{M}t} \quad (2.2)$$

$$i \frac{d}{dx} |\tilde{\nu}\rangle = \frac{1}{2E_\nu} \cdot \tilde{A} |\tilde{\nu}\rangle \quad (2.3)$$

Calculating \tilde{A} in every step costs some additional matrix multiplications. However, for all problems that are not heavily dominated by matter effects, these costs are overcompensated by a much smoother potential for which ZVODE needs less steps, increasing performance and reducing numerical errors [14]. The calculation and usage of matter parameters as defined by (1.16) would give no advantages while increasing the computational effort.

The program is able to calculate the transition probabilities $3+n$ flavors. In order to do so, only the dimension of the PMNS matrix has to be adapted and the required parameters have to be defined.

By default, the Earth is modeled according to the model described in Sec. 2.1. The detector is positioned 2 km below the surface by default, which is the approximate depth of the center of IceCube. It is assumed to be point-like, because a variation on the scale of 1 km is negligible compared to the uncertainty of the generation height in the atmosphere. The generation height of the neutrinos depends on the mode in which nuCraft is used. At the time at which the thesis this report is based on was completed, all neutrinos were

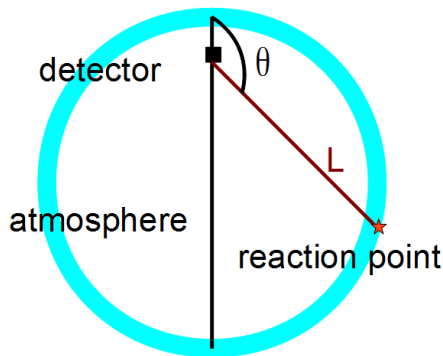


Figure 2.2: Calculation of the neutrino path length

generated at a fixed height of 20 km (configurable), see fig. 2.2. By now, more modes have been implemented to better model the Earth's atmosphere. They are based on the parametrizations in [15]. No closed-form representations of the parametrizations could be found, so numerical solutions were approximated by log-normal distributions, whose parameters were parameterized by sums of power functions in the cosine of the zenith angle, which was modified by a third-degree polynomial addend to keep it from becoming smaller than 0.05, which is the lowest value for which the original solutions were given. This way, the solutions are smooth at the horizon, which is the expected behavior.

The energy dependence of the original solutions was dropped for simplicity. Instead, the functions were evaluated at 1 GeV, which approximately is the upper energy for which the exact atmospheric profile matters for oscillations of atmospheric neutrinos. The lower energy is about 10 MeV, below which oscillations are smeared out equally for all realistic energy profiles. The flavor dependency is kept in form of discrete solutions for either muon and electron neutrinos.

The approximations show minor deviations from the original solutions, but they are good enough, given the fact that the original solutions had to be interpolated in the zenith angle between the six data points given in [15]. Also, the original solutions contain empirical values, which were only given for the two geomagnetic locations of Kamioka in Japan and Sudbury in Canada, both of which differ from the South Pole and show slight deviations from each other.

The calculation results agree well with those in [5], [16], [17], and [18].

As explained in Sec. 1.1.1, the parametrization of the PMNS matrix determines the meaning of the mixing angles. In this work, the convention used in [5] is used; in general, nuCraft supports all possible permutations of rotation matrices, including CP-violating phases. According to [5], for the 3+1 model U is defined by

$$U = R_{34}R_{24}R_{23}R_{14}R_{13}R_{12} \quad . \quad (2.4)$$

One should take note that this choice is mathematically identical to

$$U = R_{34}R_{24}R_{14}R_{23}R_{13}R_{12} \quad (2.5)$$

since R_{14} and R_{23} commute. In the 3+2-Model,

$$U = R_{45}R_{35}R_{34}R_{25}R_{24}R_{15}R_{14}R_{23}R_{13}R_{12} \quad (2.6)$$

was used, which passes into the 3+1 parametrization if one of the sterile states is not mixing.

2.3 Conventions used in this work

This work focuses on signatures of sterile neutrinos at energies higher than about 100 GeV, where oscillations between the conventional neutrinos play almost no role. Variations within the uncertainties of the relatively well-known parameters Δm_{21}^2 , Δm_{32}^2 , and θ_{12} , θ_{13} , and θ_{23} were seen to almost not influence the oscillation signatures of sterile neutrinos at high energies (see sec. 3.7). For this reason, these parameters remain fixed for this work.

For the mass parameters, $\Delta m_{21}^2 = 7.59 \cdot 10^{-5} \text{ eV}^2$ and $\Delta m_{31}^2 = 2.43 \cdot 10^{-3} \text{ eV}^2$ were chosen. These are the PDG values of 2010 [19]. For the mixing angles, a combination of PDG 2010[19] values and those of the Daya-Bay experiment was preferred [20][21]. In detail, these are: $\sin(\theta_{13}) = \sin(0.154)$, $\sin(\theta_{23}) = \sin(0.685)$, and $\sin(\theta_{12}) = \sin(0.60)$.

If not noted otherwise, inverted mass hierarchies are formed by the transition $\Delta m_{ji}^2 \rightarrow -\Delta m_{ji}^2$. The advantages of this method is that it is simple and easily reproducible, the drawback is that the resulting values are distinct from the current best-fit values for inverted mass hierarchies. Because of the relatively weak impact of the standard parameters on the studied high-energy signatures, it was decided that this is acceptable for this study.

In this work, two-dimensional plots of transition probabilities are presented. These transition probabilities are shown in dependence of the neutrino energy and of the path length L of a neutrino before reaching the detector. The path length was calculated for points equidistant in $\cos(\theta)$. The calculated energy values were chosen to be equidistant on a logarithmic scale.

The plots are visualizations of two-dimensional functions on 60000 grid points. In contrast to histograms, there is no averaging over the rectangles; instead, every rectangle represents the value of the function at its lower left corner.

In many plots an interference effect between the grid and the oscillation lengths of the neutrinos can be observed. This interference effect is known as moiré effect [22]. The pattern due to this effect does not correspond to physical oscillation probabilities. In fact, physical patterns exist in these areas, but due to the resolution of the grid they can not be resolved anymore.

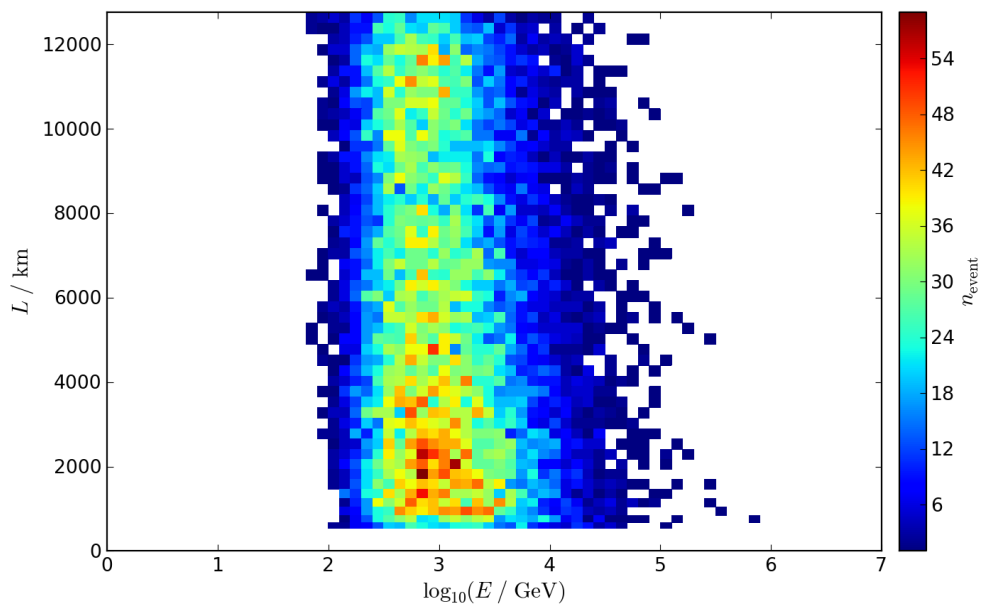


Figure 2.3: Simulated event distribution of the dataset intended for a future analysis (IC59, full year). n_{event} is the expected number of events over one year, L the path length of the neutrinos through Earth, and E the neutrino energy.

Chapter 3

3+1 model

This chapter deals with the impact of the existence of one sterile state in addition to the known states. The 3+1 model is the base for the study of models with more than one sterile state; for this reason it is quite useful to study it. Furthermore, the best fit value of WMAP is $3 + n = 4.34 \pm 0.87$ [23]. Despite this, the 3+1 model can not completely explain the MiniBooNe and LSND data [6].

Oscillations between muon and tau neutrinos and especially between muon and electron neutrinos are strongly suppressed for energies of about one TeV or more. Therefore, oscillation effects for muon neutrinos at this energy range would be a very strong hint for additional sterile states.

In order to offer a base for comparison, first of all, the oscillation effects that occur without sterile states are shown. Unless otherwise mentioned, $\Delta m_{32}^2, \Delta m_{41}^2 > 0$, i.e., the normal mass hierarchy a) in fig. 1.2, is assumed. Afterwards, the focus will be on the case that only muon neutrinos are mixing with sterile neutrinos, next on the case that only tau neutrinos do so. Then muon neutrino mixing is added again, and finally electron neutrino mixing is. All this is at first done with the assumption that there is no CP violation, but the last part of this chapter deals with non-zero CP-violating phases.

3.1 $\sin^2(\theta_{14}) = \sin^2(\theta_{24}) = \sin^2(\theta_{34}) = 0$:

Sterile neutrinos do not mix with the known states

IceCube can not discriminate between particles and anti-particles. Therefore, the fluxes of muon neutrinos and muon antineutrinos have to be treated together to give an indication of measurable effects. As approximation, the fluxes of muon neutrinos and antineutrinos are assumed to be equal.

The averaged probability over muon and muon antineutrinos produced in the atmosphere to be in beginning state is named $\frac{1}{2}(P_{\mu \rightarrow \mu} + P_{\bar{\mu} \rightarrow \bar{\mu}})$ in this work. It is shown in fig. 3.1 for the case in which sterile states are not mixing with the known. Regarding oscillation effects, non-mixing is the same as non-existence. L is the path length of the neutrino from its vertex in the atmosphere to the center of the detector as described in sec. 2.3. E the neutrino energy. The notation $s_{ij}^2 := \sin^2(\theta_{ij})$ is used.

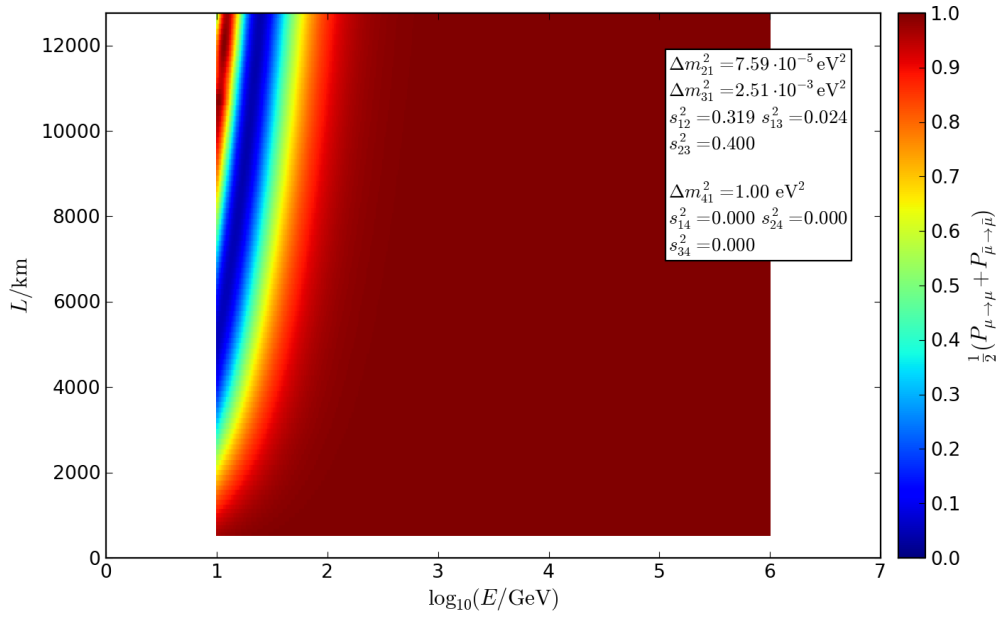


Figure 3.1: Probability $\frac{1}{2}(P_{\mu \rightarrow \mu} + P_{\bar{\mu} \rightarrow \bar{\mu}})$, averaged over muon neutrinos and antineutrinos, for a particle generated in the atmosphere to reach the detector in the same state in which it was generated. L is the path length through the Earth (s. fig. 2.2), E is the neutrino energy.

The minimum at $10 \text{ GeV} \lesssim E \lesssim 10^{1.7} \text{ GeV}$ – depending on the travel distance – is caused by muon-tau oscillations resp. those of the corresponding antiparticles. The muon-tau oscillation is similar to the vacuum oscillation. Although the neutrinos are moving through the Earth from their point of view this situation almost equals the vacuum situation. The reason for that is that both of them have the same possibilities to interact with matter and hence A in 1.14 has zero-entries for both of them. Electron neutrino contributions cause small corrections that result in differences to the vacuum situation at energies just below the first oscillation minimum. Nevertheless the resulting probabilities are almost symmetric in particles and antiparticles (s. fig. A.1).

The results for $\Delta m_{32}^2 < 0$ are almost the same. Figure 3.2 shows the difference in the probability $\frac{1}{2}(P_{\mu \rightarrow \mu} + P_{\bar{\mu} \rightarrow \bar{\mu}})$ between the cases $\Delta m_{32}^2 > 0$ and $\Delta m_{32}^2 < 0$. It is caused by the electron neutrinos, because $|\Delta m_{31}^2|$ is not the same in these two cases (s. fig. 1.2).

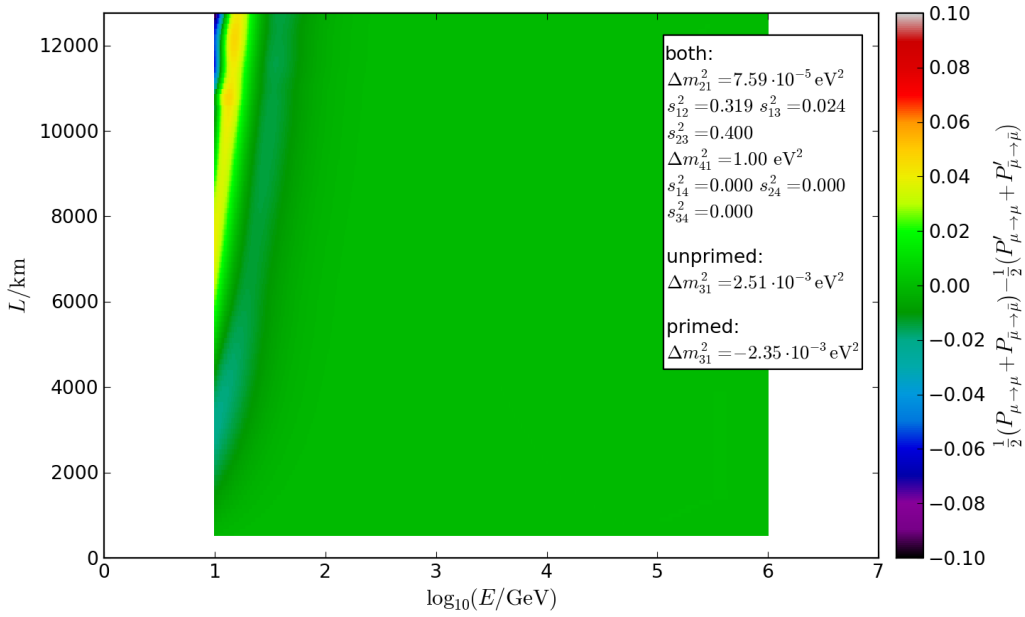


Figure 3.2: Difference $\frac{1}{2}(P_{\mu \rightarrow \mu} + P_{\bar{\mu} \rightarrow \bar{\mu}}) - \frac{1}{2}(P'_{\mu \rightarrow \mu} + P'_{\bar{\mu} \rightarrow \bar{\mu}})$ between the probabilities, averaged over muon neutrinos and antineutrinos, for a particle generated in the atmosphere to reach the detector in the same state in which it was generated, between $\Delta m_{32}^2 > 0$ (unprimed) and $\Delta m_{32}^2 < 0$ (primed). L is the path length through the Earth (s. fig. 2.2), E is the neutrino energy.

3.2 $\sin^2(\theta_{24}) \neq 0$, where $\sin^2(\theta_{34}) = \sin^2(\theta_{14}) = 0$

As an example, the probability $P_{\bar{\mu} \rightarrow \bar{\mu}}$ of a muon antineutrino produced in the atmosphere to be a muon antineutrino when reaching the detector for $\sin^2(\theta_{24}) = 0.03$ and $\Delta m_{32}^2 > 0$, $\Delta m_{41}^2 = 1 \text{ eV}^2$ is shown in fig. 3.3.

Two minima appear between $10 \text{ GeV} \lesssim E \lesssim 10^{1.7} \text{ GeV}$ and at about $E \approx 10^{3.5} \text{ GeV}$.

The minimum at $10^{3.5} \text{ GeV}$ is due to oscillation between muon antineutrinos and sterile antineutrinos. As visible in equation (1.13), in this energy range, oscillations between the know neutrinos flavors are strongly suppressed, and $P_{\bar{\mu} \rightarrow \bar{\mu}} \approx 1 - P_{\bar{\mu} \rightarrow s\bar{1}}$ (s. fig. 3.4, cf. fig. 3.3) holds. The process can be understood as a two-flavor oscillation.

It is evident from equation (1.20) that for $\Delta m_{41}^2 > 0$ resonances are only possible in the antiparticle channel.

At $E \approx 10^{3.2} \text{ GeV}$ and $L \approx 11000 \text{ km}$ there is full transition of muon antineutrinos into sterile antineutrinos. Just below that there is some kind of break in the structure. This is caused by the significant density change inside the Earth between core and mantle. The elemental composition of the matter (and hence also of the electron density) plus the density is notably changing at this radius (s. part 2.1). For that reason, the differential equation that describes the evolution of the states is notably changing, too (s. equation (1.15))

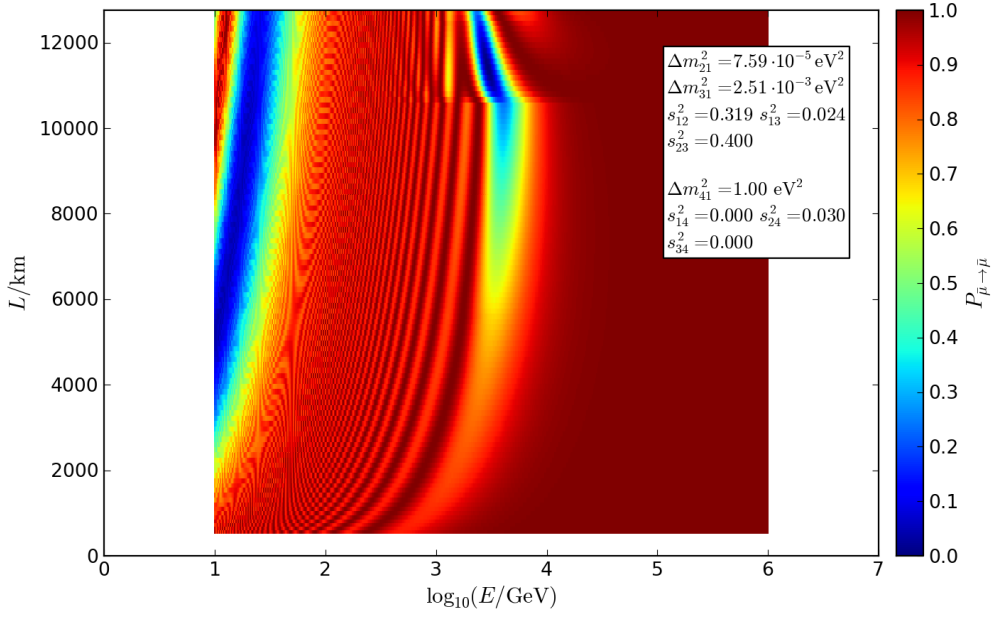


Figure 3.3: Probability $P_{\bar{\mu} \rightarrow \bar{\mu}}$ for a muon antineutrino generated in the atmosphere to reach the detector as a muon antineutrino. L is the path length through the Earth (s. fig. 2.2), E is the neutrino energy.

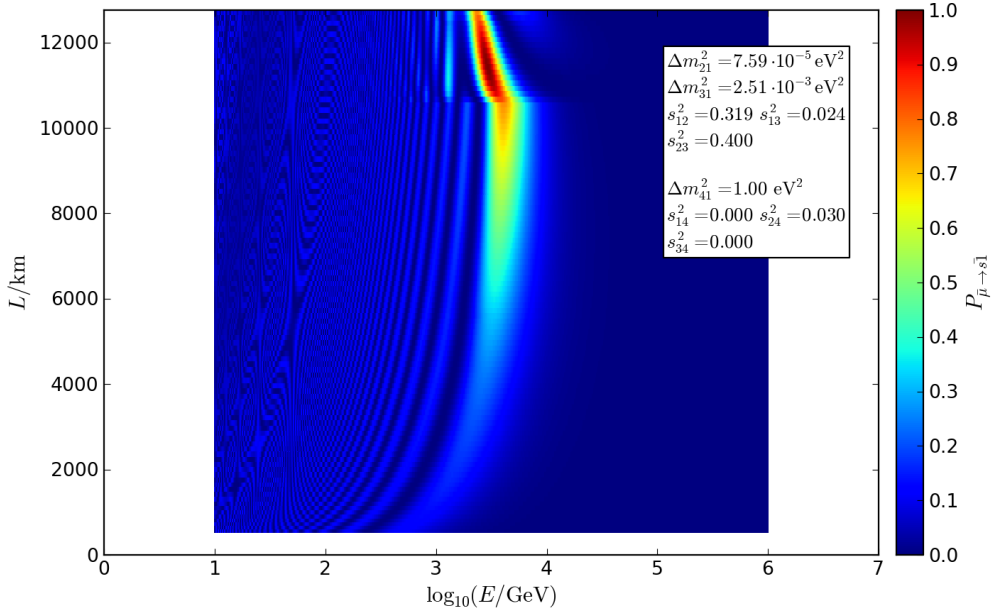


Figure 3.4: Probability $P_{\bar{\mu} \rightarrow s1}$ for a muon antineutrino generated in the atmosphere to reach the detector as a sterile antineutrino. L is the path length through the Earth (s. fig. 2.2), E is the neutrino energy.

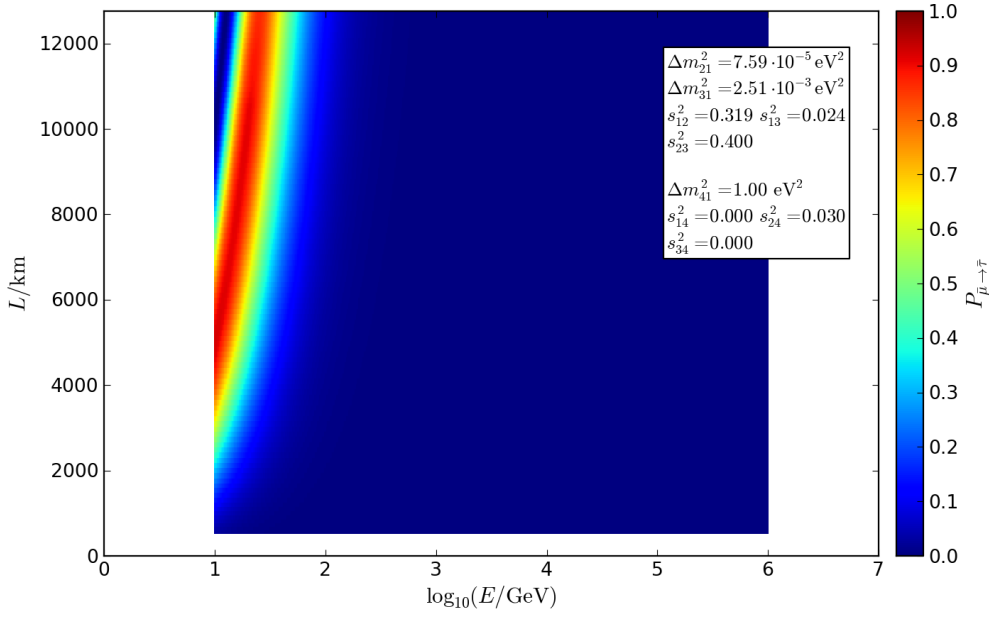


Figure 3.5: Probability $P_{\bar{\mu} \rightarrow \bar{\tau}}$ for a muon antineutrino generated in the atmosphere to reach the detector as a tau antineutrino. L is the path length through the Earth (s. fig. 2.2), E is the neutrino energy.

Especially in the area of the low-energy minimum, the moiré effect is noticeable, which was described in part 2.3. In this region, there are structures as fine as or finer than the calculation grid, thus they cannot be resolved anymore.

The low-energy minimum is due to oscillations between tau and muon antineutrinos (s. fig. 3.5), as already explained in part 3.1. The shape of these muon-tau oscillations is not affected by the additional resonance at $E \approx 10^{3.5}$ GeV. The probability $P_{\mu \rightarrow \tau}$ of a muon antineutrino to be a tau antineutrino at the time of detection is shown in fig. 3.6. The shape of the muon-tau oscillations still is almost symmetrical in particles and antiparticles for $\sin^2(\theta_{24}) \neq 0$ (cf. fig. 3.5, fig. 3.6). Mixing of muon and sterile neutrinos reduces the maximum of $P_{\bar{\mu} \rightarrow \bar{\tau}}$. Its position slightly shifts towards higher energies (s. fig. 3.7, cf. fig. A.1). The larger $\sin^2(\theta_{24})$ is, the more pronounced the changes are (s. fig. A.2). The sign of Δm_{32}^2 does not influence the oscillation between muon and sterile antineutrinos. The resonance stays in the antiparticle channel for $\Delta m_{32}^2 < 0$. For $\Delta m_{32}^2 < 0$ the maximum value of $P_{\mu \rightarrow \tau}$ is reduced and the position of the maximum is shifted as seen in the antiparticle channel before (s. fig. A.3, cf. fig. 3.7). So the asymmetry of the oscillations of both channels is not due to the resonance. Instead it is caused by changed effective mixing angles and masses in matter: The muon antineutrino gets a greater mass and for the effective mixing angle $\theta_{23, \text{Mat}}$ between muon and tau antineutrinos in matter $\theta_{23, \text{Mat}} < \theta_{23}$ holds.

The measurable probability $\frac{1}{2}(P_{\mu \rightarrow \mu} + P_{\bar{\mu} \rightarrow \bar{\mu}})$ of the presented example is shown in fig. 3.8. Regarding the averaged probability there are no differences between $\Delta m_{32}^2 > 0$ and $\Delta m_{32}^2 < 0$ that do not exist without sterile states. Caused by the already described asymmetry in particles and antiparticles the low-energy minimum is less deep than for $\sin^2(\theta_{14}) = \sin^2(\theta_{24}) = \sin^2(\theta_{34}) = 0$ (s. fig. 3.8, cf. fig. 3.3).

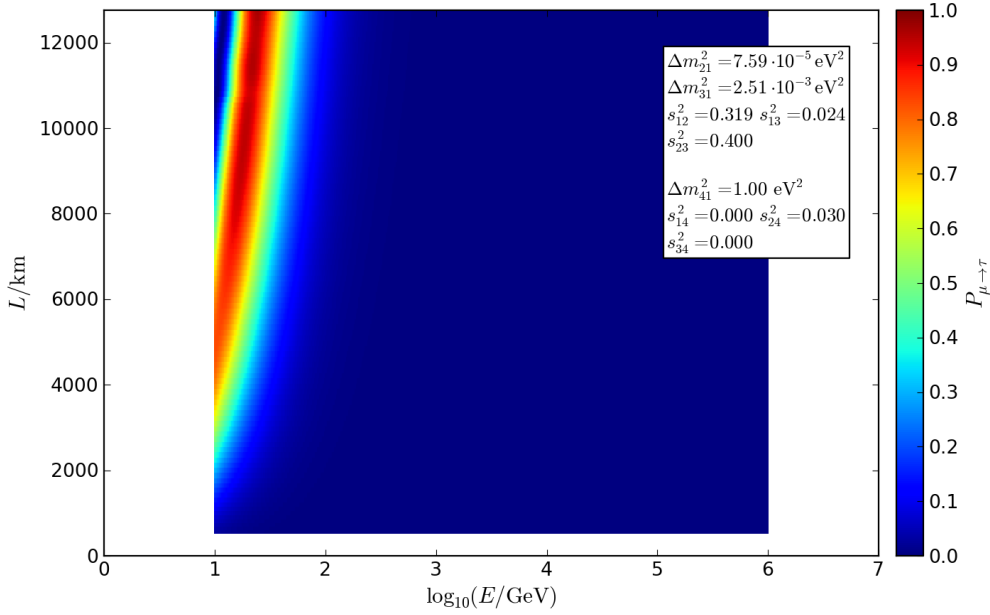
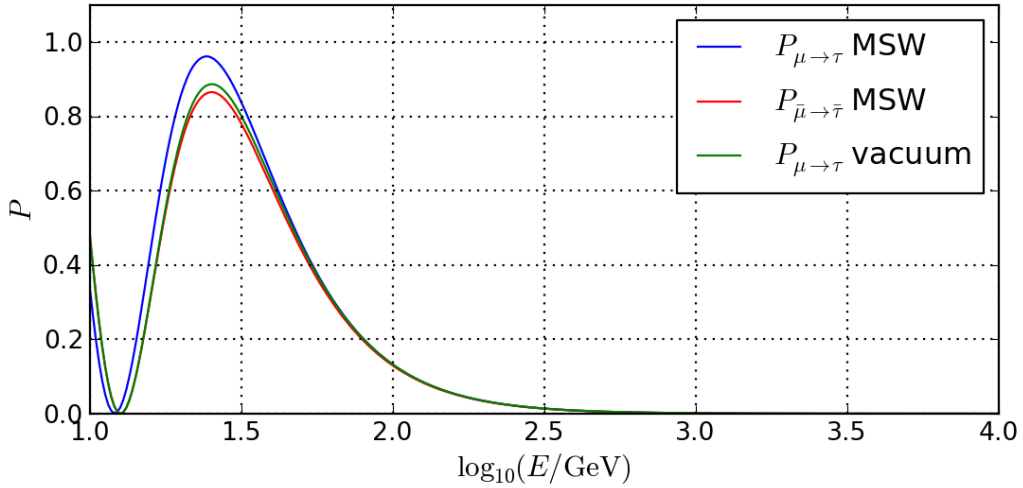


Figure 3.6: Probability $P_{\mu \rightarrow \tau}$ for a muon neutrino generated in the atmosphere to reach the detector as a tau neutrino. L is the path length through the Earth (s. fig. 2.2), E is the neutrino energy.



$$\begin{aligned} \Delta m_{41}^2 &= 1.00 \text{ eV}^2 & s_{14}^2 &= 0.000 & s_{24}^2 &= 0.030 & s_{34}^2 &= 0.000 \\ \Delta m_{21}^2 &= 7.59 \cdot 10^{-5} \text{ eV}^2 & \Delta m_{31}^2 &= 2.51 \cdot 10^{-3} \text{ eV}^2 & s_{12}^2 &= 0.319 & s_{13}^2 &= 0.024 & s_{23}^2 &= 0.400 \end{aligned}$$

Figure 3.7: Comparison of the probabilities $P_{\mu \rightarrow \tau}$, $P_{\bar{\mu} \rightarrow \bar{\tau}}$ of an vertically incoming antimuon/muon neutrino produced in the atmosphere to be an antitau/tau neutrino when reaching the detector. E denotes the neutrino energy.

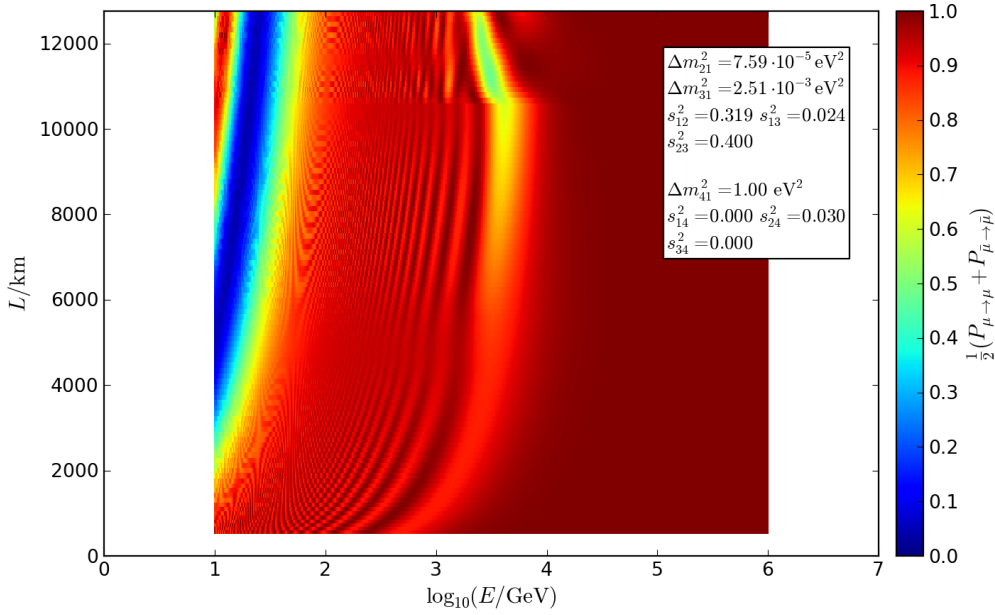


Figure 3.8: Probability $\frac{1}{2} (P_{\mu \rightarrow \mu} + P_{\bar{\mu} \rightarrow \bar{\mu}})$, averaged over muon neutrinos and antineutrinos, for a particle generated in the atmosphere to reach the detector in the same state in which it was generated. L is the path length through the Earth (s. fig. 2.2), E is the neutrino energy.

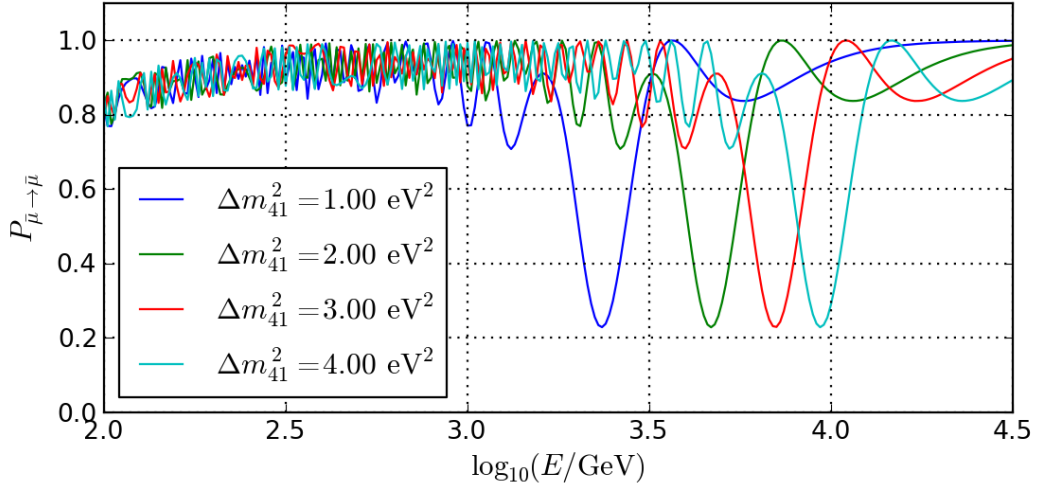
Because there is no noticeable transition $P_{\mu \rightarrow s1}$, in the TeV range transition probabilities $\frac{1}{2} (P_{\mu \rightarrow \mu} + P_{\bar{\mu} \rightarrow \bar{\mu}}) < \frac{1}{2}$ are not possible.

For other $\Delta m_{41}^2 > 0$ a stretching of the oscillation between muon and sterile antineutrinos on the energy axis occurs. In this process, the shape on the logarithmic axis stays the same (s. fig. 3.9). There is a linear dependence of the position of each point on Δm_{41}^2 , which directly follows from the combination of the equations (1.17), (1.18), and (1.11). So for further examination it is enough to analyze different mixing angles at a fixed value of Δm_{41}^2 .

If $\sin^2(\theta_{24})$ varies, the position on the energy axis roughly remains the same, but the shape of the signature changes. For smaller $\sin^2(\theta_{34})$ the minimum becomes thinner and moves towards larger path lengths L . For $\sin^2(\theta_{24}) \lesssim 0.01$ a full transition of muon antineutrinos into sterile antineutrinos is not achieved anymore (s. fig. 3.10, cf. fig. 3.3), because the maximum path length that is possible due to the Earth's geometry is not sufficient. The corresponding probability $\frac{1}{2} (P_{\mu \rightarrow \mu} + P_{\bar{\mu} \rightarrow \bar{\mu}})$ for $\sin^2(\theta_{24}) = 0.01$ can be found in the appendix (fig. A.4) together with another example (fig. A.5 and fig. A.6).

For greater $\sin^2(\theta_{24})$ the minimum moves towards smaller path lengths. For even larger values, vortices appear, the low-energy oscillations get overshadowed, and probabilities up to $\frac{1}{2} (P_{\mu \rightarrow \mu} + P_{\bar{\mu} \rightarrow \bar{\mu}}) \approx \frac{1}{2}$ occur in the whole energy range between 10 GeV and 10 TeV (s. fig. 3.11, fig. A.7). Effects like that would have been experimentally measured already, therefore, rigorous borders on θ_{24} can be given.

For $\Delta m_{41}^2 < 0$ the resonance in the oscillations between muon and sterile antineutrinos switches to the neutrino channel (s. Abb. A.8). The averaged probability over particles



$$s_{14}^2 = 0.000 \quad s_{24}^2 = 0.030 \quad s_{34}^2 = 0.040$$

$$\Delta m_{21}^2 = 7.59 \cdot 10^{-5} \text{ eV}^2 \quad \Delta m_{31}^2 = 2.51 \cdot 10^{-3} \text{ eV}^2 \quad s_{12}^2 = 0.319 \quad s_{13}^2 = 0.024 \quad s_{23}^2 = 0.400$$

Figure 3.9: Probability $P_{\bar{\mu} \rightarrow \bar{\mu}}$ of a vertically incoming antimuon neutrino produced in the atmosphere to be an antimuon neutrino when reaching the detector for various Δm_{41}^2 . E denotes the neutrino energy.

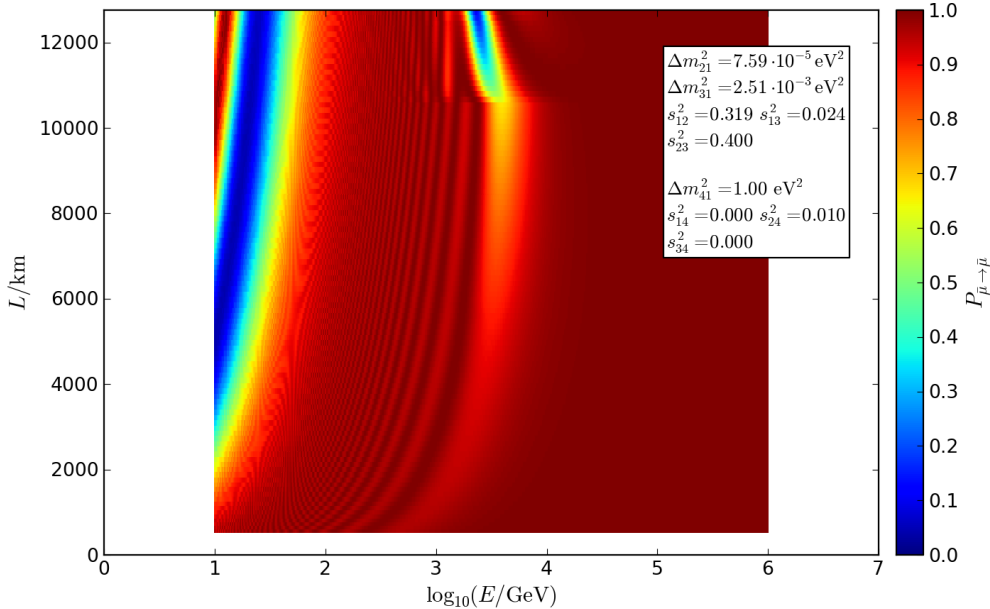


Figure 3.10: Probability $P_{\bar{\mu} \rightarrow \bar{\mu}}$ for a muon antineutrino generated in the atmosphere to reach the detector as a muon antineutrino. L is the path length through the Earth (s. fig. 2.2), E is the neutrino energy.

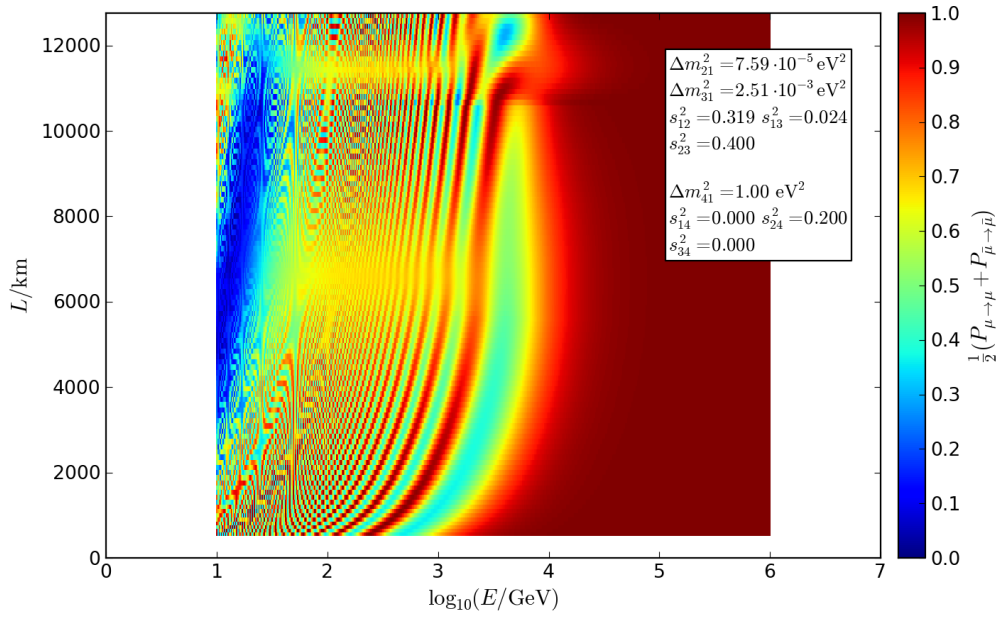
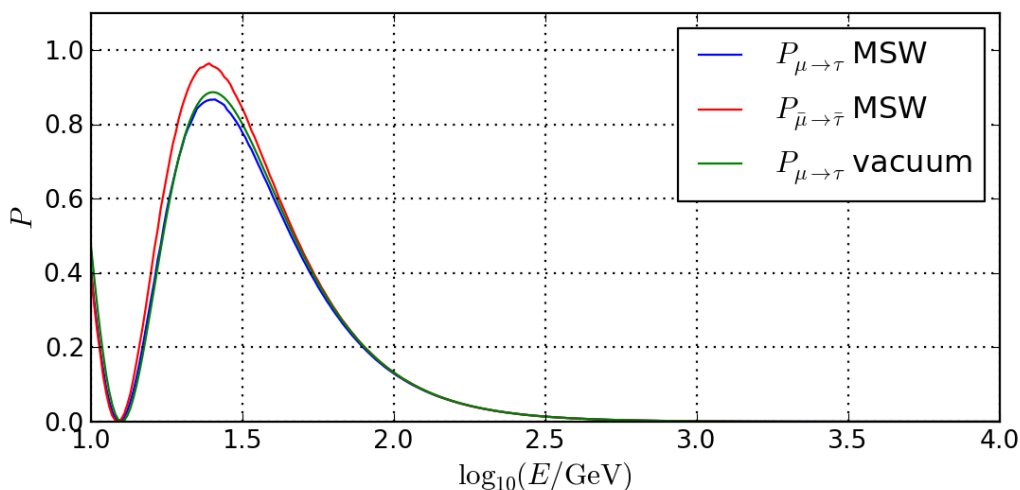


Figure 3.11: Probability $\frac{1}{2} (P_{\mu \rightarrow \mu} + P_{\bar{\mu} \rightarrow \bar{\mu}})$, averaged over muon neutrinos and antineutrinos, for a particle generated in the atmosphere to reach the detector in the same state in which it was generated. L is the path length through the Earth (s. fig. 2.2), E is the neutrino energy.

and antiparticles stays the same in very good approximation (s. fig. A.9, cf. fig. 3.8). Differences occur because of the mixing among the known states, and because $\Delta m_{41}^2 = \Delta m_{42}^2$ is only an approximation. Despite this, they are negligible even in comparison to every correction described below.

In the energy range of $10^1 \text{ GeV} - 10^6 \text{ GeV}$, the approximation $P_{\mu \rightarrow e} = P_{\bar{\mu} \rightarrow \bar{e}} = 0$ holds very well (s. fig. A.10, fig. A.11).



$$\begin{aligned} \Delta m_{41}^2 &= 1.00 \text{ eV}^2 & s_{14}^2 &= 0.000 & s_{24}^2 &= 0.000 & s_{34}^2 &= 0.030 \\ \Delta m_{21}^2 &= 7.59 \cdot 10^{-5} \text{ eV}^2 & \Delta m_{31}^2 &= 2.51 \cdot 10^{-3} \text{ eV}^2 & s_{12}^2 &= 0.319 & s_{13}^2 &= 0.024 & s_{23}^2 &= 0.400 \end{aligned}$$

Figure 3.12: Comparison of the probabilities $P_{\mu \rightarrow \tau}$ and $P_{\bar{\mu} \rightarrow \bar{\tau}}$ for a vertically incoming muon neutrino or antineutrino generated in the atmosphere to reach the detector as a tau neutrino or antineutrino. E is the neutrino energy.

3.3 $\sin^2(\theta_{34}) \neq 0$, **where** $\sin^2(\theta_{24}) = \sin(\theta_{14}) = 0$

Rigorous exclusion limits can be set on all sterile mixing angles by consideration of the results of all neutrino experiments. Oscillations between tau- and muon neutrinos are dominant in a much lower energy range than oscillations between muon and sterile neutrinos, because of $|\Delta m_{31}^2| \ll |\Delta m_{41}^2|$. Therefore, since pure-muon-neutrino initial states are investigated, resonances in the TeV range do not come along even for mixing angles above the exclusion limits (s. fig. A.12). However, changes of the effective masses and mixing angles appear in the low-energy region as already explained in part 3.2. Here, the particle and antiparticle channels are switched: For $\Delta m_{32}^2 > 0$ the maximum value of $P_{\mu \rightarrow \tau}$ decreases and the position of the oscillation maximum moves towards higher energies (s. fig. 3.12, cf. fig. 3.7). For $\Delta m_{32}^2 < 0$ equivalent changes appear in the antiparticle channel. Because particles with energies below 100 GeV are very rare in the data set that will be used in the follow-up analysis, this effect would not be recognizable. Very large mixing angles result in reduced low-energy oscillations for long path lengths. They can be excluded because oscillations are observed in this area.

3.4 $\sin^2(\theta_{24}), \sin^2(\theta_{34}) \neq 0$, **where** $\sin^2(\theta_{14}) = 0$

In order to study the effects that are caused by adding θ_{34} , $\sin^2(\theta_{34}) = 0.04$ was fixed while the other parameters are the same as in fig. 3.8. Fig. 3.13 shows the resulting probability $\frac{1}{2} (P_{\mu \rightarrow \mu} + P_{\bar{\mu} \rightarrow \bar{\mu}})$. In comparison to fig. 3.8, the first minimum moves upwards and to the left, hence towards lower energies and greater path lengths. For smaller path lengths the

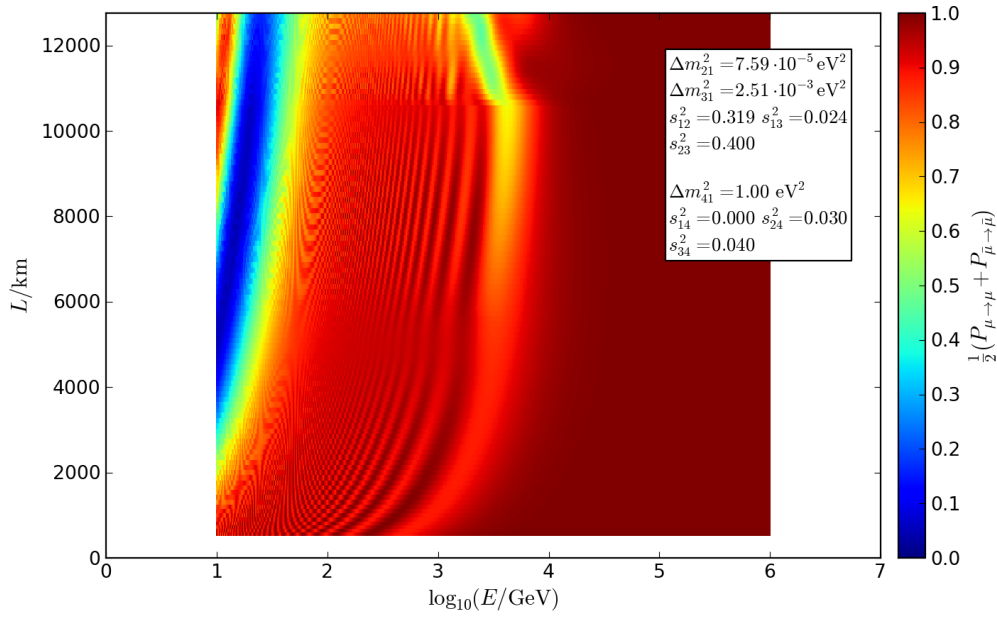


Figure 3.13: Probability $\frac{1}{2} (P_{\mu \rightarrow \mu} + P_{\bar{\mu} \rightarrow \bar{\mu}})$, averaged over muon neutrinos and antineutrinos, for a particle generated in the atmosphere to reach the detector in the same state in which it was generated. L is the path length through the Earth (s. fig. 2.2), E is the neutrino energy.

shape remains relatively unchanged. $\frac{1}{2} (P_{\mu \rightarrow \mu} + P_{\bar{\mu} \rightarrow \bar{\mu}})$ decreases in the medium-energy range by about 0.1 in comparison to fig. 3.8. The low-energy minimum is wider but less deep. In order to understand these effects, the muon-tau oscillation has to be considered carefully in both channels.

Firstly, the transition probability of muon antineutrinos into tau antineutrinos is shown in fig. 3.14. Compared to the corresponding plot for $\sin^2(\theta_{34}) = 0.00$ (fig. 3.5), first of all a maximum at about $E \approx 10^{3.1}$ GeV attracts attention. Even full transition is possible at the upper edge. The low-energy oscillation maximum is slightly curved to the left. The shape in the TeV range stretches linearly on the energy scale in dependence of Δm_{41}^2 (s. fig. 3.15). Furthermore, the resonance between sterile and muon antineutrinos is reduced (s. fig. 3.16, cf. fig. 3.4).

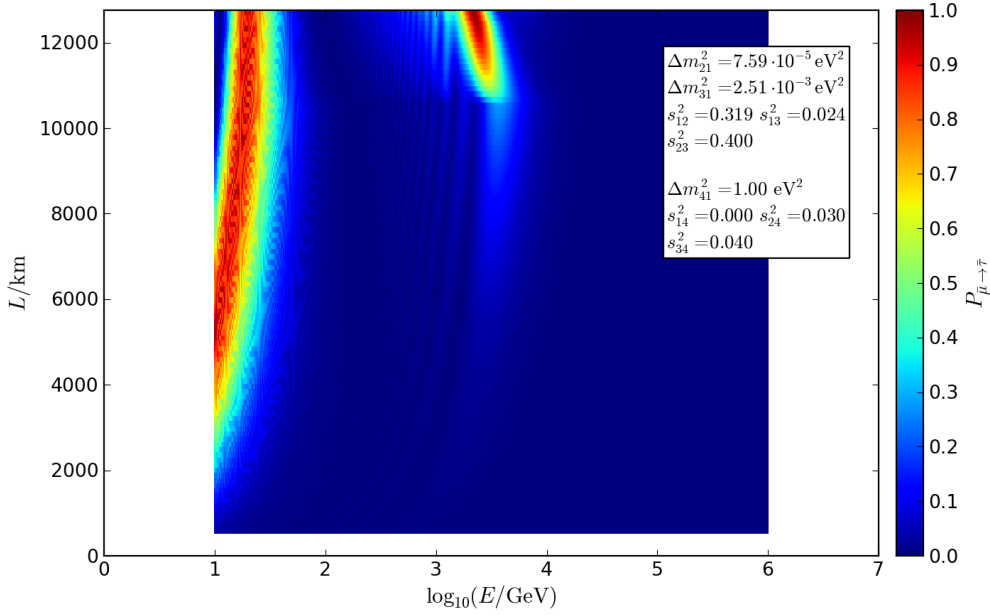
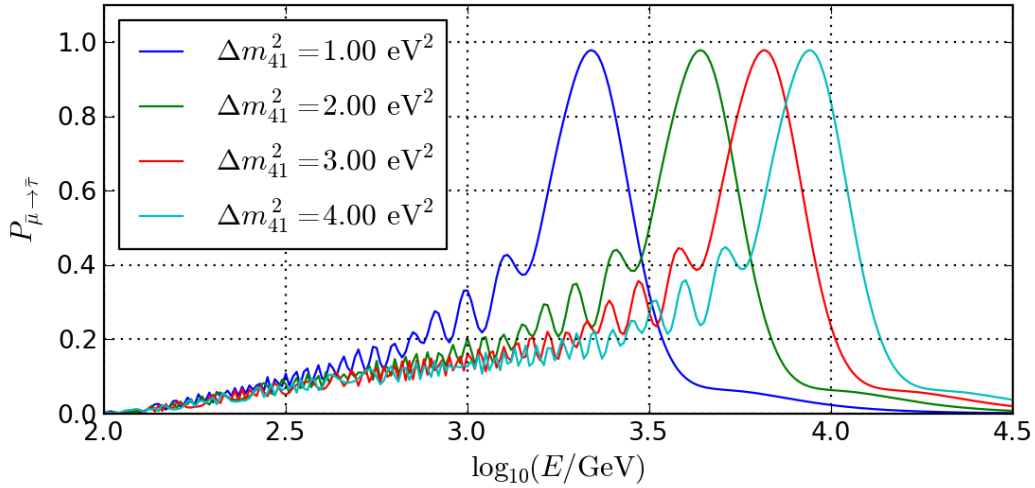


Figure 3.14: Probability $P_{\mu \rightarrow \tau}$ for a muon antineutrino generated in the atmosphere to reach the detector as a tau antineutrino. L is the path length through the Earth (s. fig. 2.2), E is the neutrino energy.



$$s_{14}^2 = 0.000 \quad s_{24}^2 = 0.030 \quad s_{34}^2 = 0.040$$

$$\Delta m_{21}^2 = 7.59 \cdot 10^{-5} \text{ eV}^2 \quad \Delta m_{31}^2 = 2.51 \cdot 10^{-3} \text{ eV}^2 \quad s_{12}^2 = 0.319 \quad s_{13}^2 = 0.024 \quad s_{23}^2 = 0.400$$

Figure 3.15: Probability $P_{\mu \rightarrow \tau}$ for a vertically incoming muon antineutrino generated in the atmosphere to reach the detector as a tau antineutrino, for various Δm_{41}^2 . E is the neutrino energy.

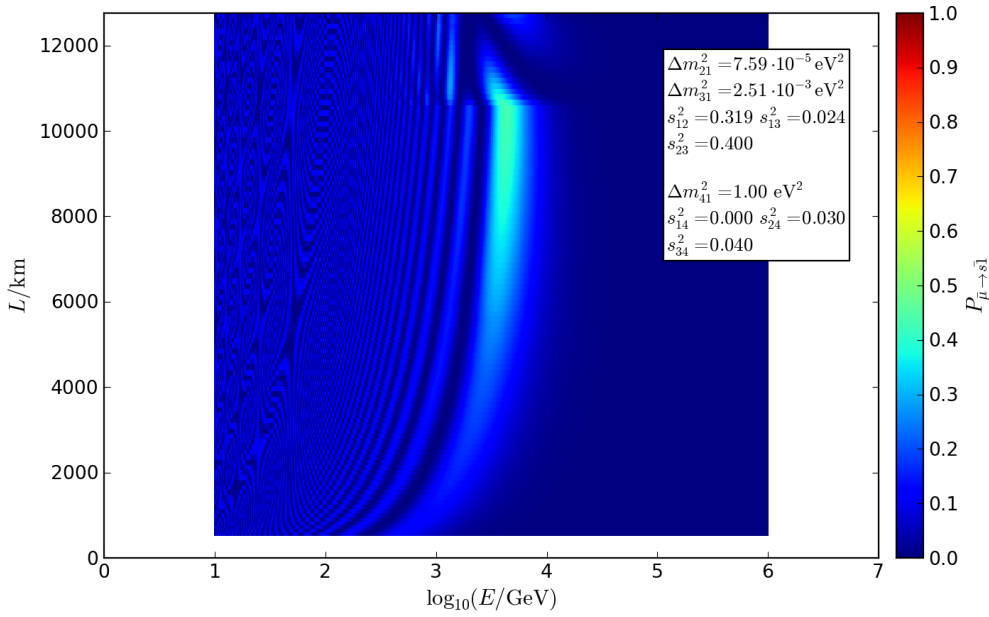


Figure 3.16: Probability $P_{\bar{\mu} \rightarrow \bar{s}1}$ for a muon antineutrino generated in the atmosphere to reach the detector as a sterile antineutrino. L is the path length through the Earth (s. fig. 2.2), E is the neutrino energy.

The oscillation between muon and tau antineutrinos still occurs if muon neutrinos do not mix with tau neutrinos (s. fig. 3.17, cf. fig. 3.14). Therefore, this process can be understood as a sequence of two two-flavor oscillations. The terms of $P_{\bar{\mu} \rightarrow \bar{\tau}}$ that cause the resonance in the TeV range do not depend on θ_{23} . At any given point inside the Earth, atmospheric muon antineutrinos with energies in the TeV range only have the possibility to be either an muon antineutrino or a sterile antineutrino if $\sin^2(\theta_{34}) = 0$ applies. If $\sin^2(\theta_{34})$ is non-zero, even though muon antineutrinos can not directly transform into tau antineutrinos at high energies, they are able to pass over into tau antineutrinos if they were sterile antineutrinos before.

From the mathematical point of view, terms are added that depend on $\sin^2(\theta_{34})$, $\sin^2(\theta_{24})$, and $\Delta m_{43}^2 \approx \Delta m_{42}^2 \approx \Delta m_{41}^2$. Switching the values of $\sin^2(\theta_{24})$ and $\sin^2(\theta_{34})$ approximately leads to the same transition probabilities (cf. fig. 3.16, fig. 3.18). Despite that it turns out that $\sin^2(\theta_{24}) \cdot \sin^2(\theta_{34})$ is not the critical value (s. fig. 3.19). Neither are $\sin^2(\theta_{24}) + \sin^2(\theta_{34})$ nor $\sin(\theta_{24}) + \sin(\theta_{34})$ the critical quantities (s. fig. A.13). This is already clear, because these can take non-zero values for $\sin^2(\theta_{34}) = 0 \vee \sin^2(\theta_{24}) = 0$ but there are no resonances of $P_{\bar{\mu} \rightarrow \bar{\tau}}$ in this case. The smaller the value of $\sin^2(\theta_{34})$ is while $\sin^2(\theta_{24})$ is fixed, and the greater $\sin^2(\theta_{24})$ is while $\sin^2(\theta_{34})$ is fixed, the more considerable the resonance between muon and sterile antineutrinos becomes (cf. fig. 3.16, fig. 3.20). The reason is that for large $\sin^2(\theta_{24})$ many sterile antineutrinos arise and that for small $\sin^2(\theta_{34})$ only a few of them pass over into tau antineutrinos. Still, the quotient $\sin^2(\theta_{24}) \div \sin^2(\theta_{34})$ is not a good parameter because $\sin^2(\theta_{24})$ is a characteristic variable for the shape of the signature. Furthermore, for $\sin^2(\theta_{34}) \rightarrow 0$ divergent behavior is not observable.

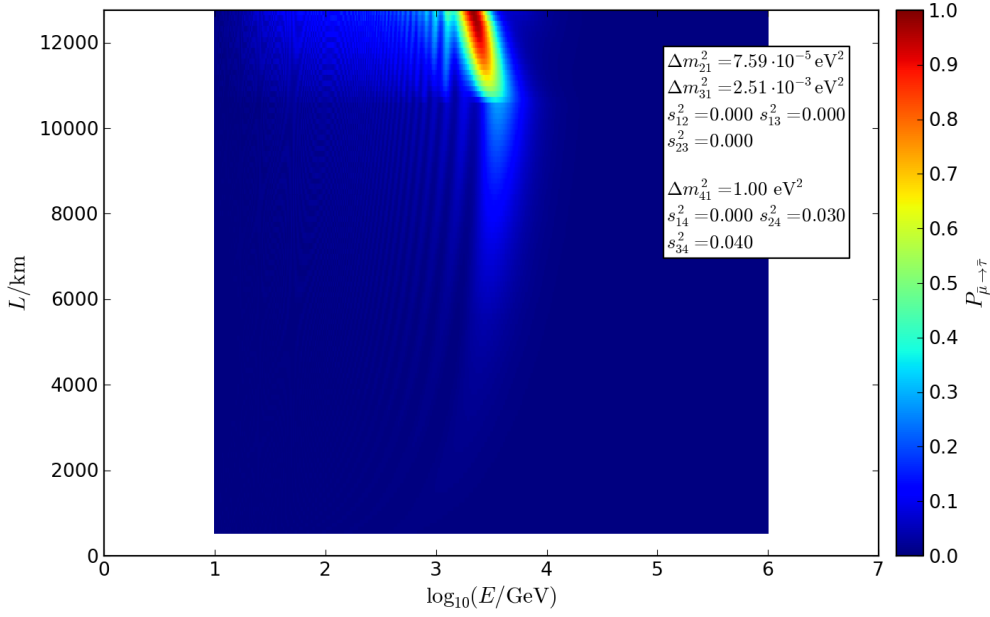


Figure 3.17: Probability $P_{\bar{\mu} \rightarrow \bar{\tau}}$ for a muon antineutrino generated in the atmosphere to reach the detector as a tau antineutrino. L is the path length through the Earth (s. fig. 2.2), E is the neutrino energy.

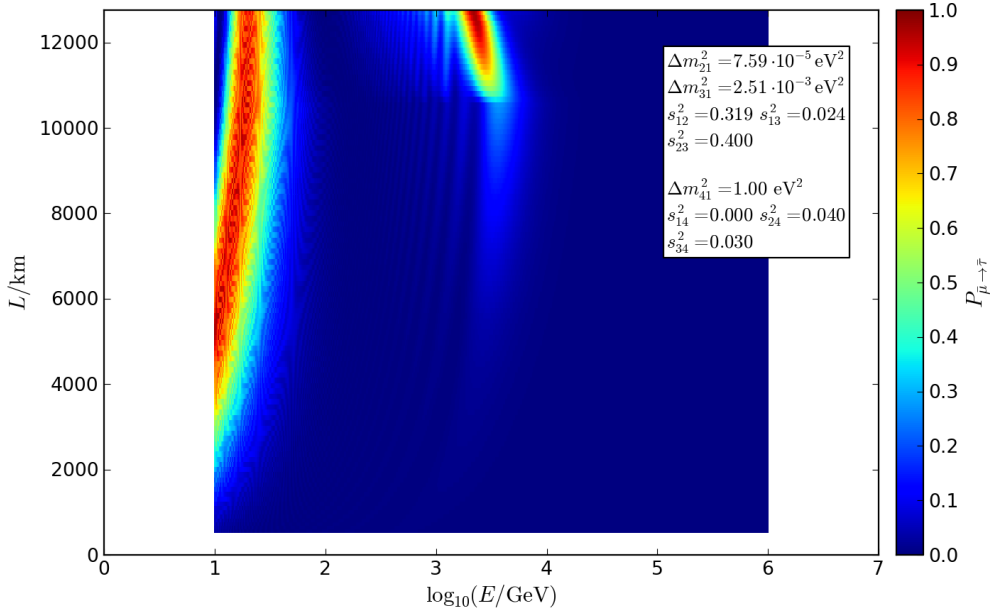
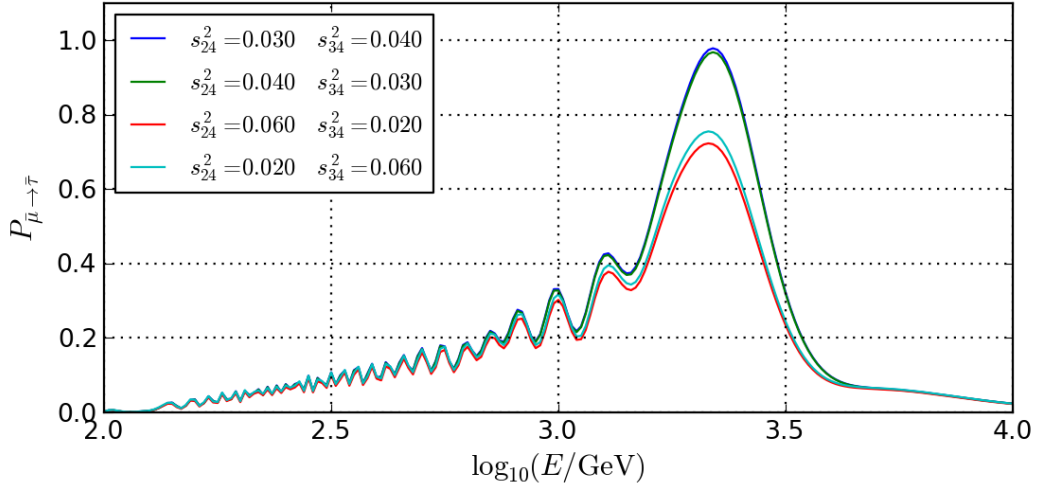


Figure 3.18: Probability $P_{\bar{\mu} \rightarrow \bar{\tau}}$ for a muon antineutrino generated in the atmosphere to reach the detector as a tau antineutrino. L is the path length through the Earth (s. fig. 2.2), E is the neutrino energy.



$$\Delta m_{41}^2 = 1.00 \text{ eV}^2 \quad s_{14}^2 = 0.000$$

$$\Delta m_{21}^2 = 7.59 \cdot 10^{-5} \text{ eV}^2 \quad \Delta m_{31}^2 = 2.51 \cdot 10^{-3} \text{ eV}^2 \quad s_{12}^2 = 0.319 \quad s_{13}^2 = 0.024 \quad s_{23}^2 = 0.400$$

Figure 3.19: Probability $P_{\bar{\mu} \rightarrow \bar{\tau}}$ for a vertically incoming muon antineutrino generated in the atmosphere to reach the detector as a tau antineutrino, for various $\sin^2(\theta_{24})$, $\sin^2(\theta_{34})$ with $\sin^2(\theta_{24}) \cdot \sin^2(\theta_{34}) = 0.0012$. E is the neutrino energy.

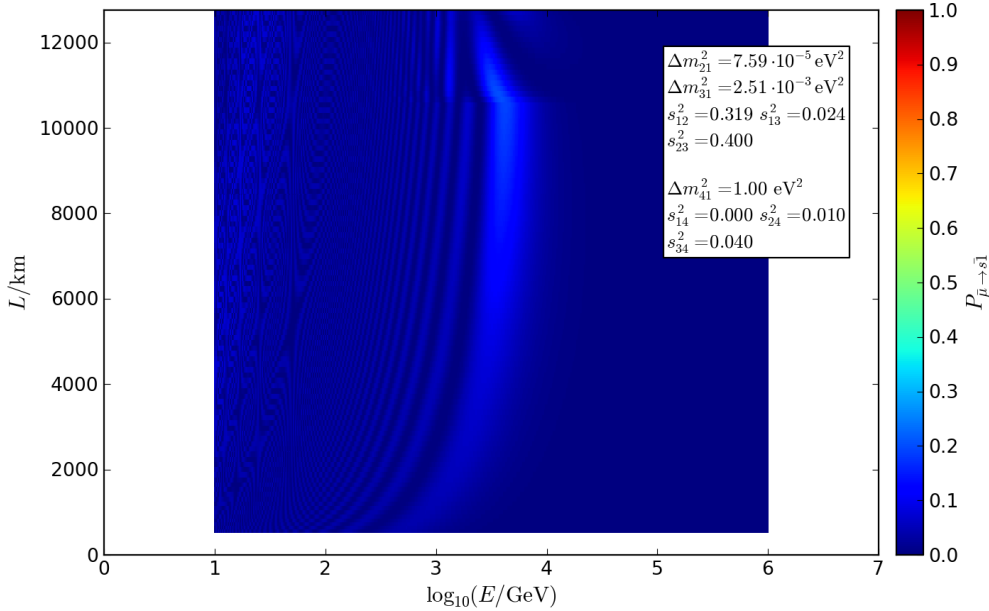


Figure 3.20: Probability $P_{\bar{\mu} \rightarrow \bar{s}1}$ for a muon antineutrino generated in the atmosphere to reach the detector as a sterile antineutrino. L is the path length through the Earth (s. fig. 2.2), E is the neutrino energy.

It is necessary to focus on the particle channel to understand the decrease of the probability $\frac{1}{2}(P_{\mu \rightarrow \mu} + P_{\mu \rightarrow \bar{\mu}})$. The probability of the transition of muon into tau neutrinos is shown in fig. 3.21. There is a widening of the low-energy oscillation signatures in contrast to the corresponding probability $P_{\mu \rightarrow \tau}$ for $\sin^2(\theta_{34}) = 0.00$ (fig. 3.6). The same effect appears if electron neutrinos are not mixing with any neutrino type (s. fig. A.15, cf. fig. 3.21). So this is not a result of a four-flavor oscillation. The widening does not occur in vacuum (s. fig. A.16, cf. fig. 3.21). When having a careful look at fig. 3.21, one can see a break at about the same height as in fig. 3.3, so matter parameters have to be considered.

Next, the dependencies of the widening of the low-energy oscillation on $\sin^2(\theta_{34})$ and $\sin^2(\theta_{24})$ is studied. With fixed $\sin^2(\theta_{24})$, the widening is more noticeable the greater $\sin^2(\theta_{34})$ is, and vice versa. In approximation, the product $\sin^2(\theta_{24}) \cdot \sin^2(\theta_{34})$ is the significant parameter (cf. fig. 3.21, fig. 3.22, for the difference s. fig. A.17). $P_{\mu \rightarrow \tau}$ also contains terms that lead to corrections at around the area of the low-energy oscillations in case of $\sin^2(\theta_{24}) = 0$. $\sin^2(\theta_{24}) \cdot \sin^2(\theta_{34})$ is not the relevant parameter for this terms. Therefore, $\sin^2(\theta_{24}) \cdot \sin^2(\theta_{34})$ is the most important parameter for the widening, but not the only one.

For further illustration, fig. 3.23 shows $P_{\mu \rightarrow \tau}$ for a vertically incoming neutrino ($L \approx 2 \cdot \text{Earthradius}$) for various $\sin^2(\theta_{34})$ with $\sin^2(\theta_{24}) = 0.03$ fixed. $P_{\mu \rightarrow \tau}$ for a vertically incoming particle and various $\sin^2(\theta_{24})$ with $\sin^2(\theta_{34}) = 0.03$ fixed is shown in fig. 3.24.

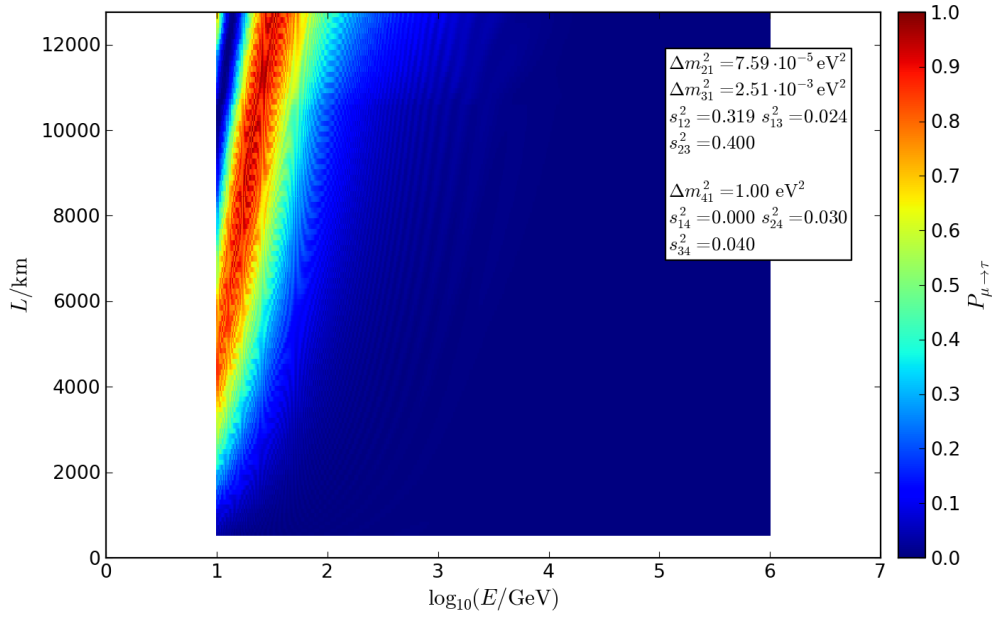


Figure 3.21: Probability $P_{\mu \rightarrow \tau}$ for a muon neutrino generated in the atmosphere to reach the detector as a tau neutrino. L is the path length through the Earth (s. fig. 2.2), E is the neutrino energy.

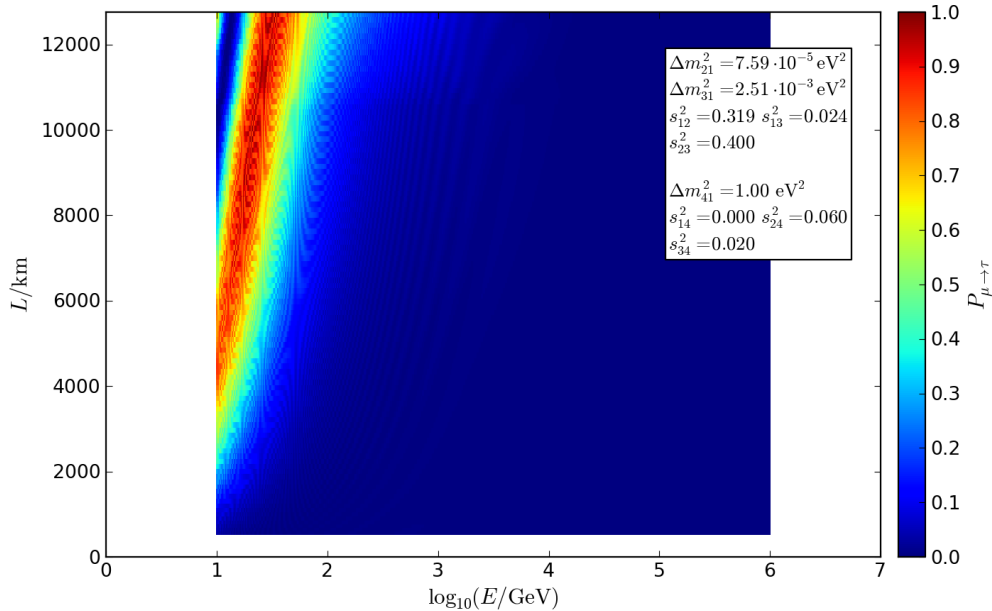
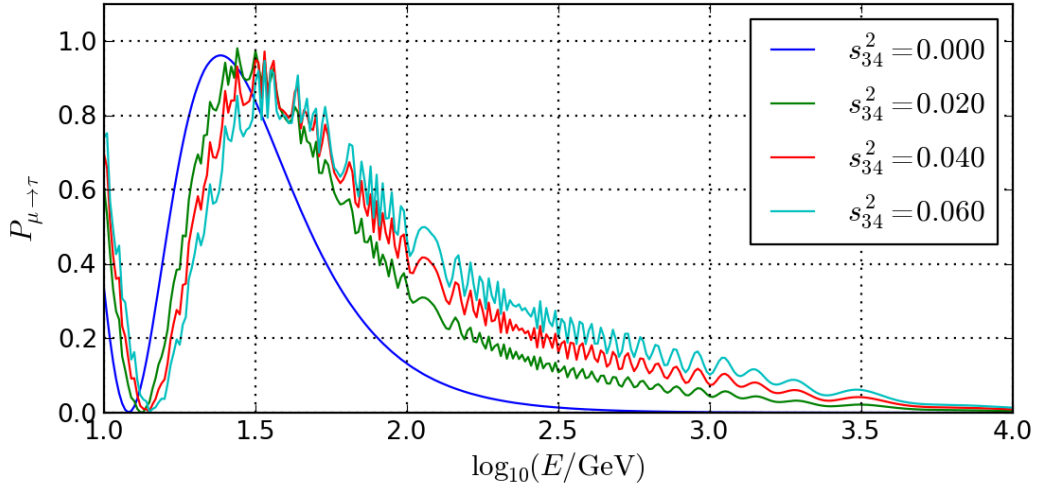


Figure 3.22: Probability $P_{\mu \rightarrow \tau}$ for a muon neutrino generated in the atmosphere to reach the detector as a tau neutrino. L is the path length through the Earth (s. fig. 2.2), E is the neutrino energy.



$$\begin{aligned} \Delta m_{41}^2 &= 1.00 \text{ eV}^2 & s_{14}^2 &= 0.000 & s_{24}^2 &= 0.030 \\ \Delta m_{21}^2 &= 7.59 \cdot 10^{-5} \text{ eV}^2 & \Delta m_{31}^2 &= 2.51 \cdot 10^{-3} \text{ eV}^2 & s_{12}^2 &= 0.319 & s_{13}^2 &= 0.024 & s_{23}^2 &= 0.400 \end{aligned}$$

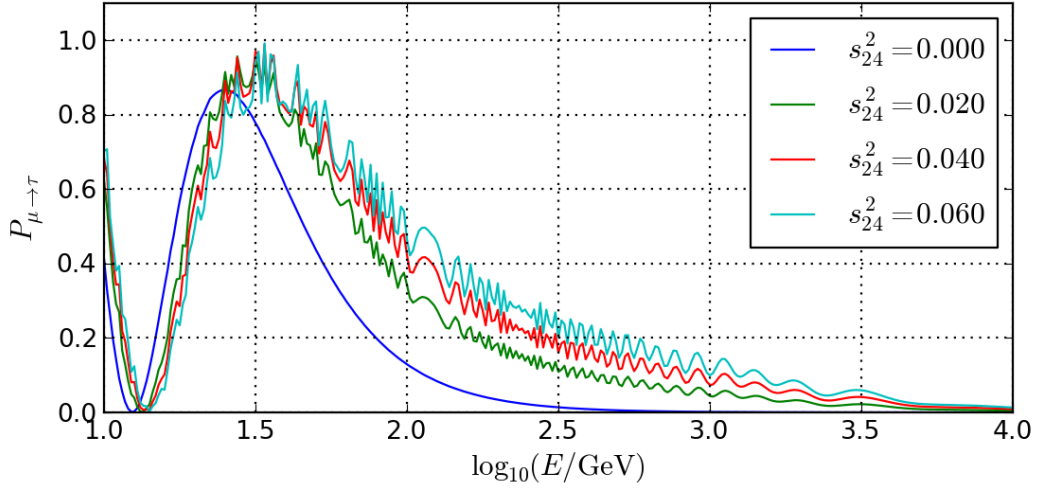
Figure 3.23: Probability $P_{\mu \rightarrow \tau}$ for a vertically incoming muon neutrino generated in the atmosphere to reach the detector as a tau neutrino, for various $\sin^2(\theta_{34})$ with $\sin^2(\theta_{24}) = 0.03$ constant. E is the neutrino energy.

For $\theta_{23} = 0$ there are no low-energy oscillations that could change (s. fig. A.18). Consequently, the oscillation probabilities contain terms that depend on θ_{23} , θ_{24} , and θ_{34} . There is a dependence on Δm_{41}^2 , but it is less important than the dependence on the mixing angles (s. fig. 3.25, cf. fig. 3.23, fig. 3.24).

For $\Delta m_{41}^2 < 0$ the resonance of $P_{\bar{\mu} \rightarrow \bar{\tau}}$ in fig. 3.14 is switched into the particle channel (s. fig. 3.26). The widening of the low-energy oscillations in the particle channel still stays there for $\Delta m_{41}^2 < 0$ so that both effects are in the same channel.

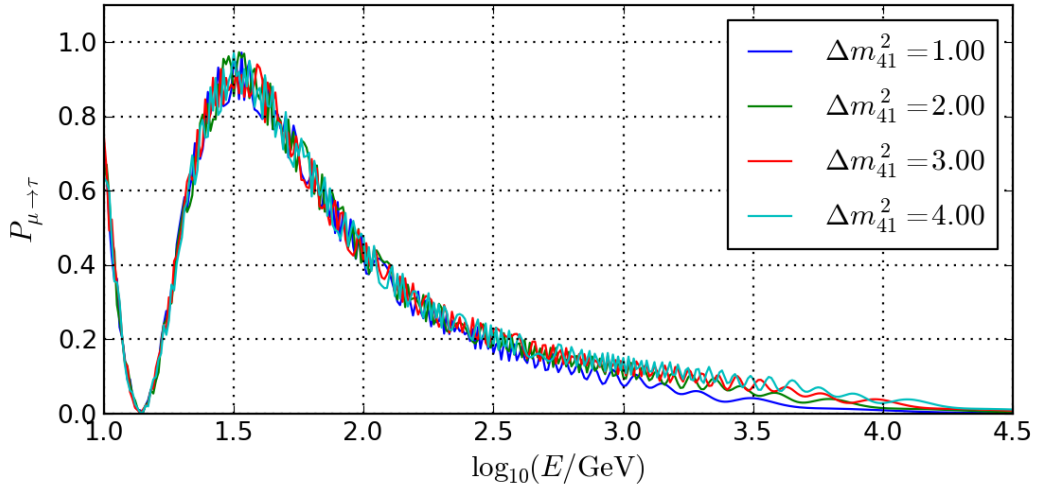
For $\Delta m_{32}^2 < 0$ the widening of the low-energy oscillations is switched into the antiparticle channel (s. fig. 3.27, cf. fig. 3.21). The higher-energy maximum can be found either in the particle channel ($\Delta m_{41}^2 < 0$) or in the antiparticle channel ($\Delta m_{41}^2 > 0$).

Considering all described aspects results in the conclusion that terms must be important that depend on $\Delta m_{32, \text{Mat}}^2$ and on mixing angles $\theta_{23, \text{Mat}}$. The oscillation probabilities contain matter parameters of higher order, meaning that they depend on $\sin^2(\theta_{23})$, $\sin^2(\theta_{34})$, $\sin^2(\theta_{24})$, Δm_{32}^2 , $|\Delta m_{41}^2|$, ρ , and E .



$$\begin{aligned} \Delta m_{41}^2 &= 1.00 \text{ eV}^2 & s_{14}^2 &= 0.000 & s_{34}^2 &= 0.030 \\ \Delta m_{21}^2 &= 7.59 \cdot 10^{-5} \text{ eV}^2 & \Delta m_{31}^2 &= 2.51 \cdot 10^{-3} \text{ eV}^2 & s_{12}^2 &= 0.319 & s_{13}^2 &= 0.024 & s_{23}^2 &= 0.400 \end{aligned}$$

Figure 3.24: Probability $P_{\mu \rightarrow \tau}$ for a vertically incoming muon neutrino generated in the atmosphere to reach the detector as a tau neutrino, for various $\sin^2(\theta_{24})$ with $\sin^2(\theta_{34}) = 0.03$ constant. E is the neutrino energy.



$$\begin{aligned} s_{14}^2 &= 0.000 & s_{24}^2 &= 0.030 & s_{34}^2 &= 0.040 \\ \Delta m_{21}^2 &= 7.59 \cdot 10^{-5} \text{ eV}^2 & \Delta m_{31}^2 &= 2.51 \cdot 10^{-3} \text{ eV}^2 & s_{12}^2 &= 0.319 & s_{13}^2 &= 0.024 & s_{23}^2 &= 0.400 \end{aligned}$$

Figure 3.25: Probability $P_{\mu \rightarrow \tau}$ for a vertically incoming muon neutrino generated in the atmosphere to reach the detector as a tau neutrino, for various Δm_{41}^2 . E is the neutrino energy.

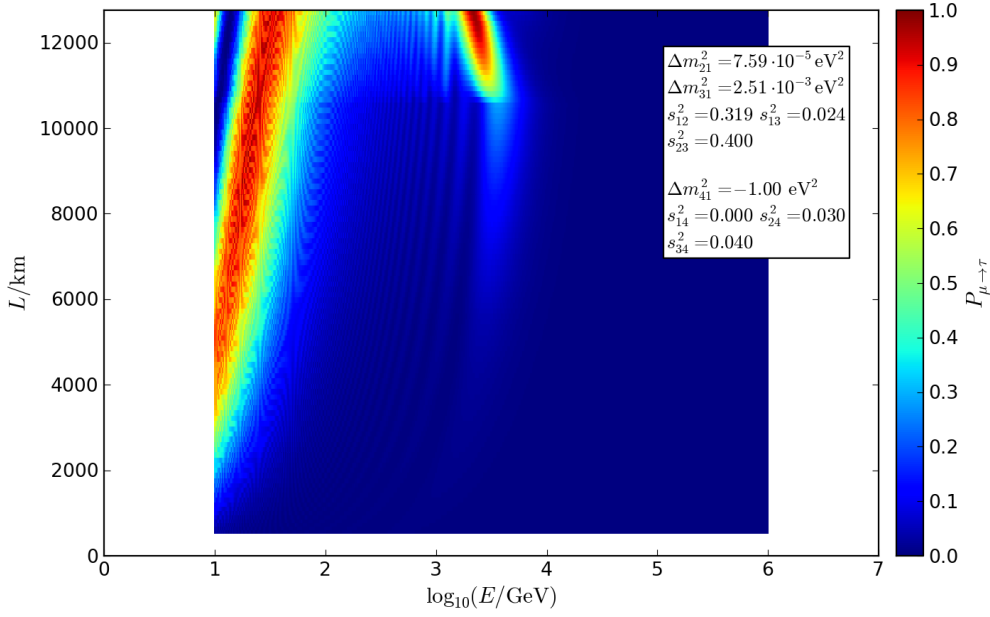


Figure 3.26: Probability $P_{\mu \rightarrow \tau}$ for a muon neutrino generated in the atmosphere to reach the detector as a tau neutrino. L is the path length through the Earth (s. fig. 2.2), E is the neutrino energy.

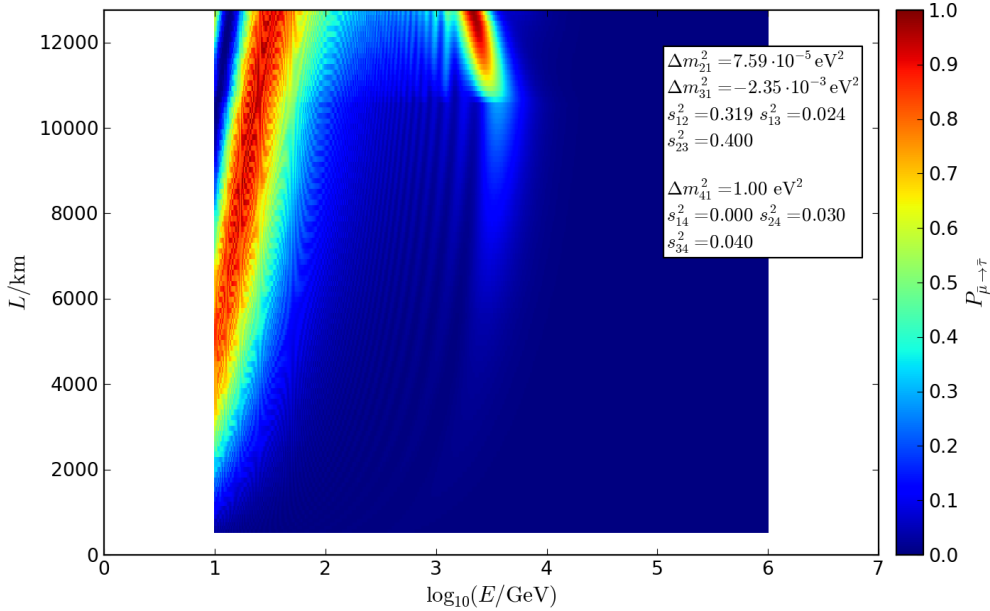


Figure 3.27: Probability $P_{\bar{\mu} \rightarrow \bar{\tau}}$ for a muon antineutrino generated in the atmosphere to reach the detector as a tau antineutrino. L is the path length through the Earth (s. fig. 2.2), E is the neutrino energy.

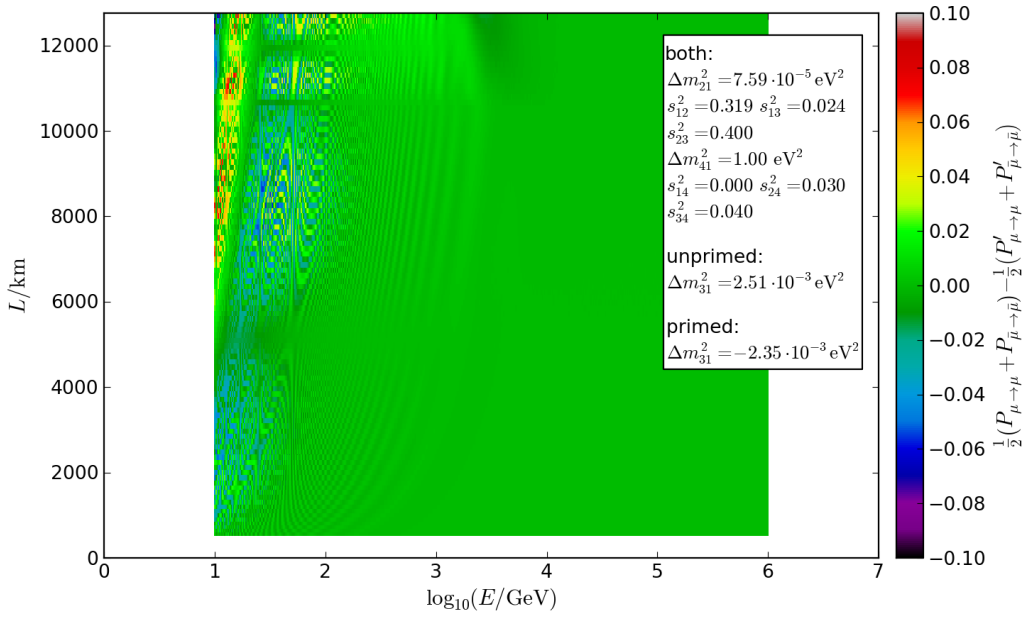


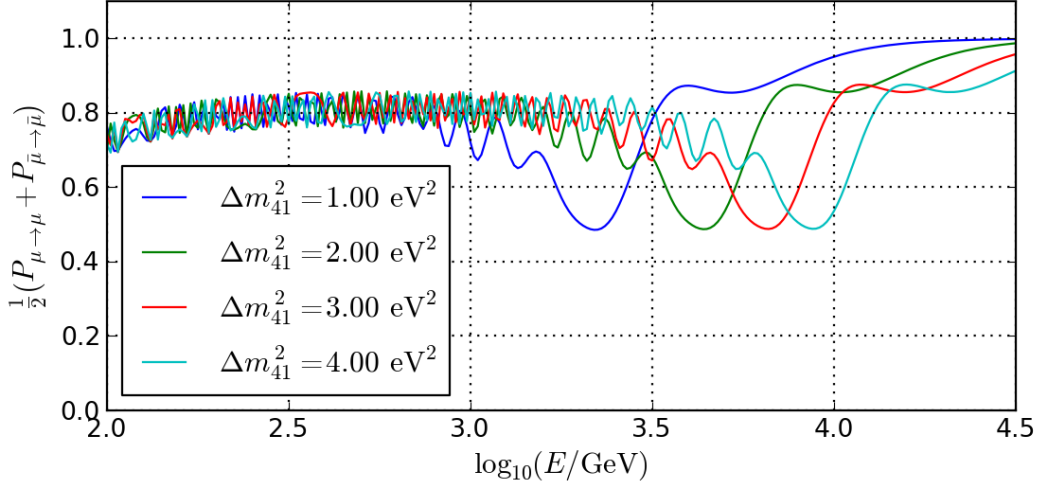
Figure 3.28: Difference $\frac{1}{2}(P_{\mu \rightarrow \mu} + P_{\bar{\mu} \rightarrow \bar{\mu}}) - \frac{1}{2}(P'_{\mu \rightarrow \mu} + P'_{\bar{\mu} \rightarrow \bar{\mu}})$ between the probabilities, averaged over muon neutrinos and antineutrinos, for a particle generated in the atmosphere to reach the detector in the same state in which it was generated, between $\Delta m_{32}^2 > 0$ (unprimed) and $\Delta m_{32}^2 < 0$ (primed). L is the path length through the Earth (s. fig. 2.2), E is the neutrino energy.

Fig. 3.28 shows the non-zero difference of $\frac{1}{2}(P_{\mu \rightarrow \mu} + P_{\bar{\mu} \rightarrow \bar{\mu}})$ between $\Delta m_{32}^2 > 0$ (unprimed) and $\Delta m_{32}^2 < 0$ (primed) for $\Delta m_{41}^2 = 1 \text{ eV}^2 > 0$.

Matter and antimatter can annihilate, but they can not transform into each other. Therefore the calculation is done separately for both of them. Hence, any two effects are able to influence each other only if they occur in the same channel. That is the reason for the difference of the actually measurable probabilities between $\Delta m_{32}^2 < 0$ and $\Delta m_{32}^2 > 0$. This difference is also described in [24]. In this paper, $\Delta m_{41}^2 > 0$ is assumed. The measurable transition probabilities of $\Delta m_{32}^2 > 0 \wedge \Delta m_{41}^2 < 0$ and $\Delta m_{32}^2 < 0 \wedge \Delta m_{41}^2 > 0$ only differ from each other as they do for $\Delta m_{32}^2 \geq 0$ without sterile states (s. fig. A.19, cf. fig. 3.2). It is possible to identify the sign of Δm_{32}^2 only if the sign of Δm_{41}^2 is known.

After all effects that are responsible for the global shape have been described, now their dependencies on $|\Delta m_{41}^2|$ will be analyzed. The signatures in the TeV range that are due to resonant oscillations between muon and tau neutrinos as well as between muon and sterile neutrinos stretch on the logarithmic energy axis with linear dependence on $|\Delta m_{41}^2|$.

The changes of the low-energy oscillations caused by matter parameters occur at lower energies. They mainly depend on the effective mixing angles and not as much on $|\Delta m_{41}^2|$. Thus $\frac{1}{2}(P_{\mu \rightarrow \mu} + P_{\bar{\mu} \rightarrow \bar{\mu}})$ stretches as well as the probabilities $P_{\bar{\mu} \rightarrow \bar{\tau}}$ (or $P_{\mu \rightarrow \tau}$ for $\Delta m_{41}^2 < 0$) and $P_{\mu \rightarrow s1}$ (or $P_{\bar{\mu} \rightarrow s\bar{1}}$, respectively) on the energy axis. With respect to the logarithmic axis the shape stays the same with a linear dependence on $|\Delta m_{41}^2|$ (s. fig. 3.29). The widening of the low-energy oscillations can be described by $\sin^2(\theta_{24}) \cdot \sin^2(\theta_{34})$, but this does not apply for the shape in the TeV range. So the dependence on the mixing angles can not be reduced to less parameters.



$$s_{14}^2 = 0.000 \quad s_{24}^2 = 0.030 \quad s_{34}^2 = 0.040$$

$$\Delta m_{21}^2 = 7.59 \cdot 10^{-5} \text{ eV}^2 \quad \Delta m_{31}^2 = 2.51 \cdot 10^{-3} \text{ eV}^2 \quad s_{12}^2 = 0.319 \quad s_{13}^2 = 0.024 \quad s_{23}^2 = 0.400$$

Figure 3.29: Probability $\frac{1}{2} (P_{\mu \rightarrow \mu} + P_{\bar{\mu} \rightarrow \bar{\mu}})$, averaged over muon neutrinos and antineutrinos, for a vertically incoming particle generated in the atmosphere to reach the detector in the same state in which it was generated, for various Δm_{41}^2 . E is the neutrino energy.

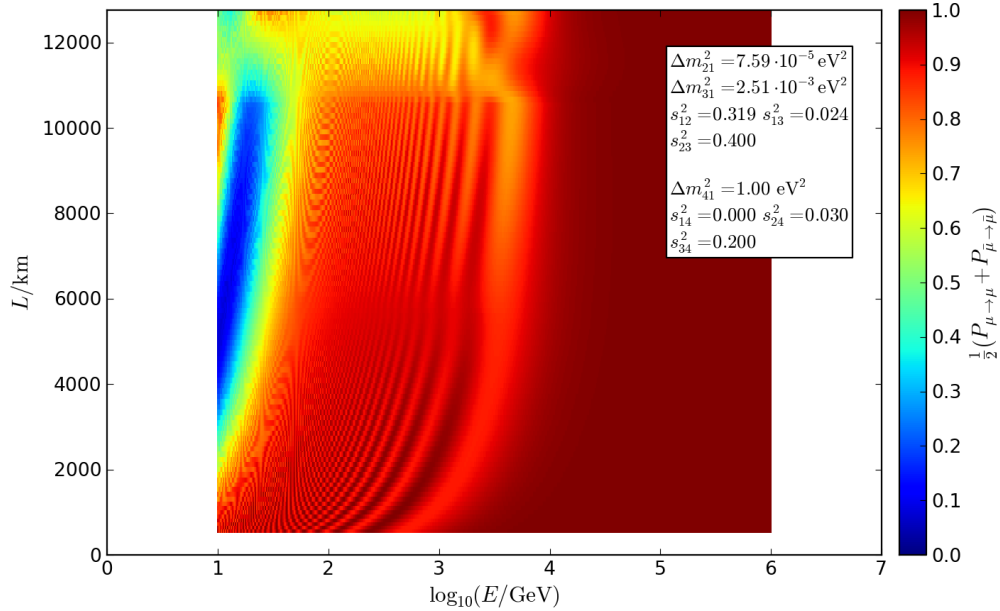


Figure 3.30: Probability $\frac{1}{2} (P_{\mu \rightarrow \mu} + P_{\bar{\mu} \rightarrow \bar{\mu}})$, averaged over muon neutrinos and antineutrinos, for a particle generated in the atmosphere to reach the detector in the same state in which it was generated. L is the path length through the Earth (s. fig. 2.2), E is the neutrino energy.

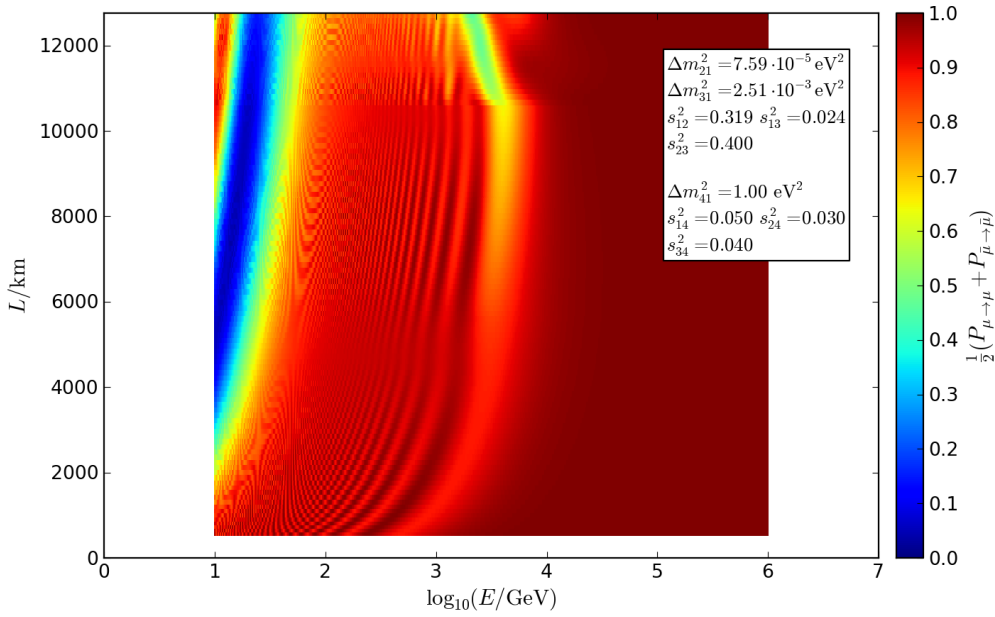


Figure 3.31: Probability $\frac{1}{2} (P_{\mu \rightarrow \mu} + P_{\bar{\mu} \rightarrow \bar{\mu}})$, averaged over muon neutrinos and antineutrinos, for a particle generated in the atmosphere to reach the detector in the same state in which it was generated. L is the path length through the Earth (s. fig. 2.2), E is the neutrino energy.

For very large $\sin^2(\theta_{34})$ the low-energy oscillations vanish for long path lengths. Furthermore, $\frac{1}{2} (P_{\mu \rightarrow \mu} + P_{\bar{\mu} \rightarrow \bar{\mu}}) \approx \frac{1}{2}$ holds between 10 and 1000 GeV for long path lengths (s. fig. 3.30). Therefore, limits of $\sin^2(\theta_{34})$ can be found. There is another example with $\Delta m^2_{41} = 1 \text{ eV}^2$, $\Delta m^2_{32} > 0$, $\sin^2(\theta_{24}) = 0.03$, $\sin^2(\theta_{34}) = 0.02$ in the appendix (fig. A.14, fig. A.20, fig. A.21, fig. A.22).

3.5 $\sin^2(\theta_{24}), \sin^2(\theta_{34}), \sin^2(\theta_{14}) \neq 0$

So far, electron neutrinos only caused small corrections due to $\Delta m^2_{21} \ll |\Delta m^2_{32}| \ll |\Delta m^2_{41}|$. The effects caused by electron neutrinos are still small if they mix with sterile states. For $\sin^2(\theta_{24}) = 0.03$, $\sin^2(\theta_{34}) = 0.04$, and $\sin^2(\theta_{14}) = 0.05$, $\frac{1}{2} (P_{\mu \rightarrow \mu} + P_{\bar{\mu} \rightarrow \bar{\mu}})$ is shown in fig. 3.31. Compared to the corresponding plot for $\sin^2(\theta_{24}) = 0.03$, $\sin^2(\theta_{34}) = 0.04$, $\sin^2(\theta_{14}) = 0.00$ (fig. 3.13), a little shift of both minima towards lower energies can be observed. Especially in the particle channel, changes of the oscillation between muon and electron neutrinos occur due to $\sin^2(\theta_{14}) \neq 0$ (s. fig. A.24, cf. fig. A.11). The modifications are just briefly mentioned because the effects are small and the correlations are complex.

There is no full transition even for very large mixing angles θ_{14} (s. fig. A.25, fig. A.26).

Effects due to changed matter parameters appear in the low-energy area of the particle channel and affect the oscillation between electron and muon neutrinos. There are also signatures in the TeV range (s. fig. A.27).

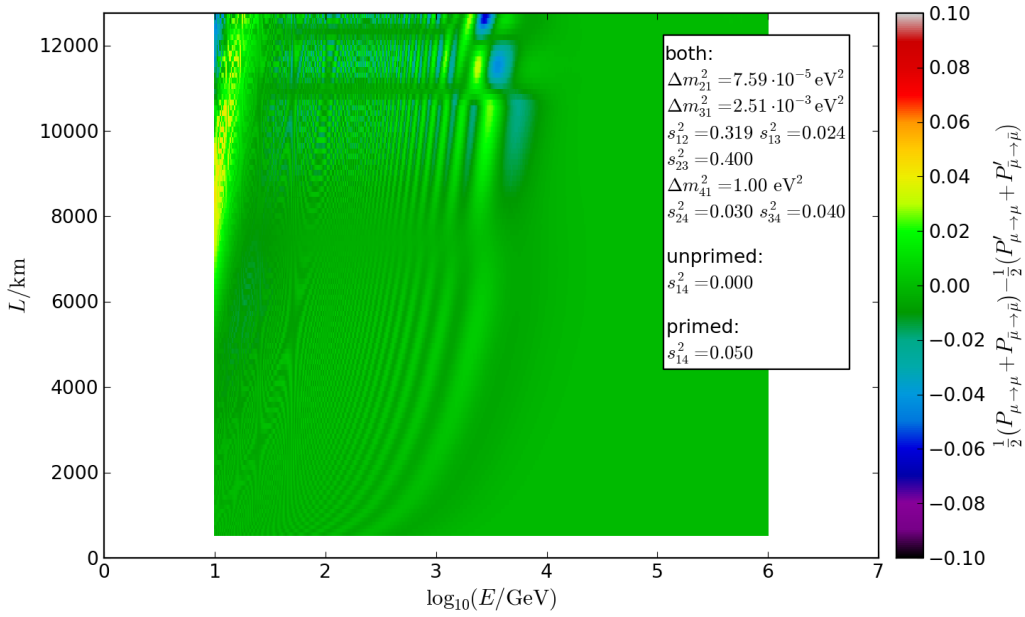


Figure 3.32: Difference $\frac{1}{2}(P_{\mu \rightarrow \mu} + P_{\bar{\mu} \rightarrow \bar{\mu}}) - \frac{1}{2}(P'_{\mu \rightarrow \mu} + P'_{\bar{\mu} \rightarrow \bar{\mu}})$ between the probabilities, averaged over muon neutrinos and antineutrinos, for a particle generated in the atmosphere to reach the detector in the same state in which it was generated, between $\sin^2(\theta_{14}) = 0.00$ (unprimed) and $\sin^2(\theta_{14}) = 0.05$ (primed). L is the path length through the Earth (s. fig. 2.2), E is the neutrino energy.

Differences compared with $\sin^2(\theta_{14}) = 0$ also exist in the antiparticle channel, but with on the scale of these plots its not easy to see them (s. fig. A.28, cf. fig. A.10). A plot of $P_{\bar{\mu} \rightarrow \bar{e}}$ in another scale is given by fig. A.29.

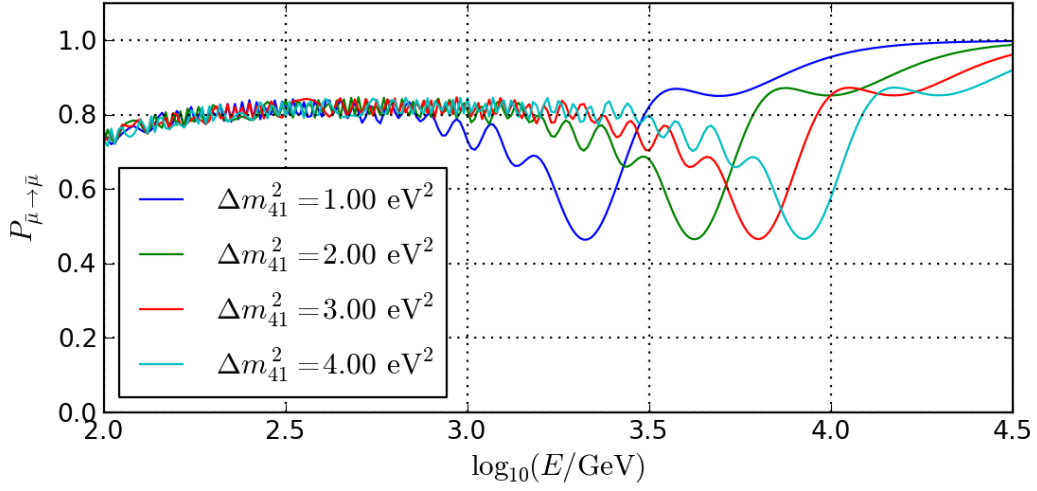
Because of the small transition probabilities, possible dependencies and signatures will not be discussed here in detail.

As a result of the changes of the oscillations between muon and electron neutrinos in both channels, the oscillations between muon neutrinos and the other states are rarely modified, too. Compared to those caused by the other mixing angles, theses changes are very small ($\lesssim 0.04$, s. fig. 3.32). This holds for all mass hierarchies, and the effects are even smaller for smaller $\sin^2(\theta_{14})$.

It is found that the TeV range signatures due to θ_{14} retain their shape on the logarithmic energy axis for other $|\Delta m^2_{41}|$. Hence, this applies for the whole shape in the TeV range, resulting from all mixing angles (cf. fig. 3.31, fig. A.23). In this whole range, the relation between the positions of points with the same probabilities and $|\Delta m^2_{41}|$ is linear (s. fig. 3.33).

3.6 CP-violating phases

In case of four neutrino types, the parametrization can be reduced to three CP-violating phases (1.23). δ_{24} , δ_{34} , and δ_{13} have been chosen.



$$\begin{aligned}
 s_{14}^2 &= 0.050 & s_{24}^2 &= 0.030 & s_{34}^2 &= 0.040 \\
 \Delta m_{21}^2 &= 7.59 \cdot 10^{-5} \text{ eV}^2 & \Delta m_{31}^2 &= 2.51 \cdot 10^{-3} \text{ eV}^2 & s_{12}^2 &= 0.319 & s_{13}^2 &= 0.024 & s_{23}^2 &= 0.400
 \end{aligned}$$

Figure 3.33: Probability $\frac{1}{2}(P_{\mu \rightarrow \mu} + P_{\bar{\mu} \rightarrow \bar{\mu}})$, averaged over muon neutrinos and antineutrinos, for a vertically incoming particle generated in the atmosphere to reach the detector in the same state in which it was generated, for various Δm_{41}^2 . E is the neutrino energy.

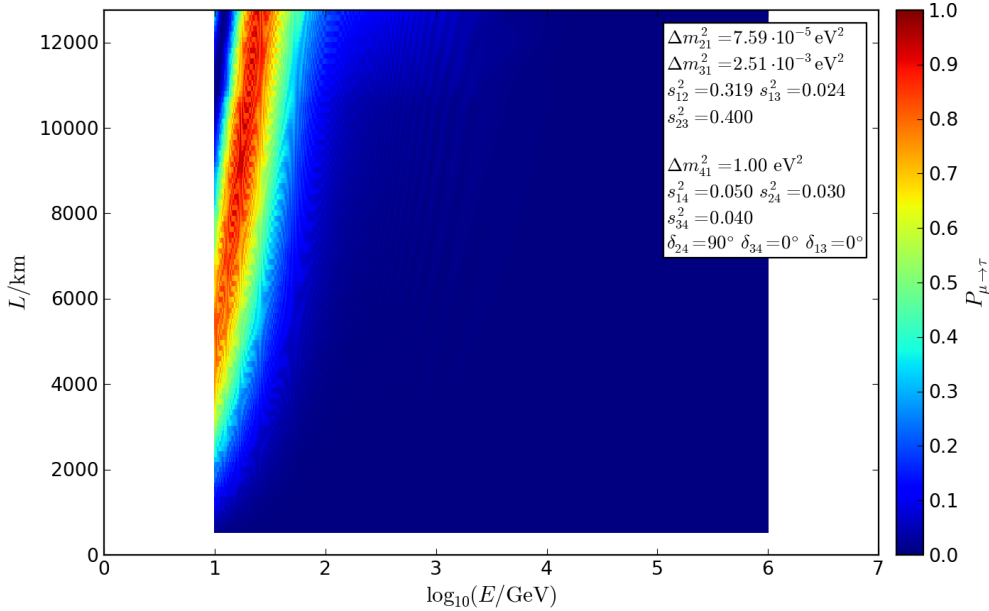


Figure 3.34: Probability $P_{\mu \rightarrow \tau}$ for a muon neutrino generated in the atmosphere to reach the detector as a tau neutrino. L is the path length through the Earth (s. fig. 2.2), E is the neutrino energy.

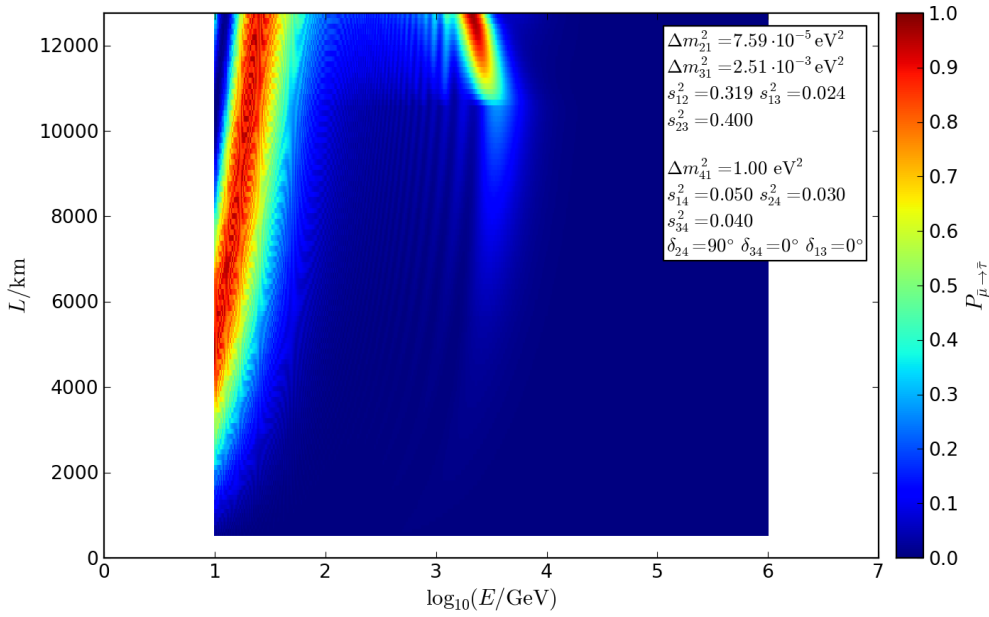


Figure 3.35: Probability $P_{\bar{\mu} \rightarrow \bar{\tau}}$ for a muon antineutrino generated in the atmosphere to reach the detector as a tau antineutrino. L is the path length through the Earth (s. fig. 2.2), E is the neutrino energy.

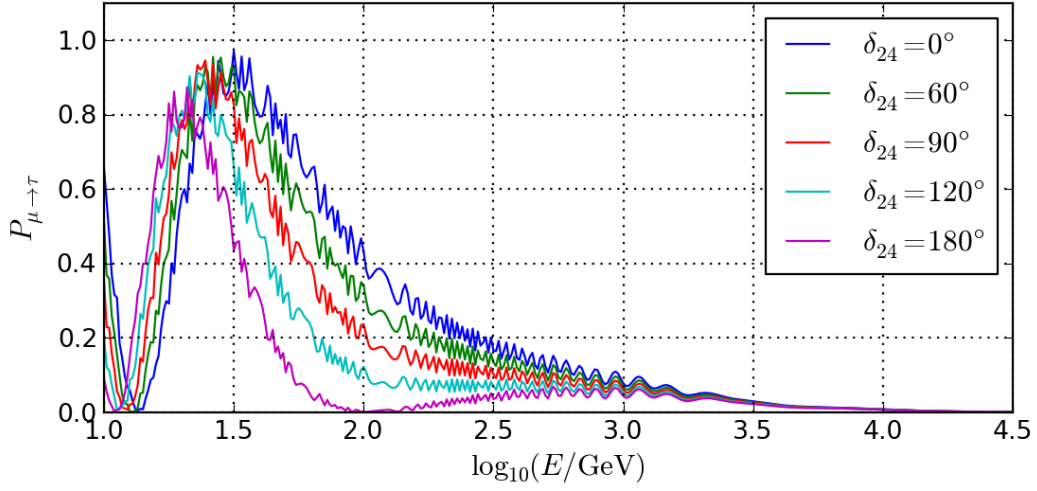
For $\sin^2(\theta_{34}) = \sin^2(\theta_{14}) = 0.00$, the effects due to sterile states can be described by a two-flavor oscillation (s. part 3.2). Thus, CP-violating phases do not lead to changes in this case (s. part 1.1.3). For δ_{34} , this is already implied by construction because the matrix entry that is multiplied with the phases is zero. For non-zero $\sin^2(\theta_{34})$ and $\Delta m_{41}^2 > 0$ (< 0), resonances in the muon-tau oscillations occur in the particle (antiparticle) channel. These are understandable as a sequence of two two-flavor oscillations (s. part 3.4). Caused by this fact, these signatures do not change if CP-violation is added. On the other hand, the observed widening of the low-energy oscillations depends on θ_{23} , θ_{24} , and θ_{34} . Hence in this case CP-violation is relevant.

In order to give an example, $P_{\mu \rightarrow \tau}$ is shown in fig. 3.34 for $\delta_{24} \neq 0^\circ$, $\delta_{34} = \delta_{13} = 0^\circ$, the corresponding probability $P_{\bar{\mu} \rightarrow \bar{\tau}}$ in fig. 3.35. Compared to the corresponding plot for $\delta_{ij} = 0^\circ$ (fig. 3.21), one can see that now the widening occurs not only in the particle but also in the antiparticle channel. The signature in this energy range is symmetric. For $\delta_{ij} = 0^\circ$, it spreads out up to higher energies (cf. fig. 3.21, fig. 3.34, fig. 3.35). For further examination, various $\delta_{24} \neq 0^\circ$ are going to be compared: $P_{\mu \rightarrow \tau}$ is shown in fig. 3.36 for various $\delta_{24} \neq 0^\circ$ and vertically incoming particles. The corresponding $P_{\bar{\mu} \rightarrow \bar{\tau}}$ is shown in fig. 3.37. The phase causes a rotation of the matter-dependent changes of the medium- and low-energy oscillations from the particle into the antiparticle channel (s. part 3.4).

Provided that there is only a single non-vanishing CP-violating phase, the chosen phases δ_{24} and δ_{34} result in similar transition probabilities (s. fig. A.30, fig. A.31, cf. fig. 3.36, fig. 3.37). In the corresponding plot for δ_{13} (fig. 3.38), all lines lie on top of each other. δ_{13} does not produce such changes. Although the 3+1 model contains four neutrino flavors, at the energies relevant here their oscillations arise just among three flavors due to $\Delta m_{21}^2 \ll |\Delta m_{32}^2| \ll |\Delta m_{41}^2|$. In case of three oscillating sorts, the parametrization can be reduced to one single phase (1.23). It has to be inserted in one of the components that

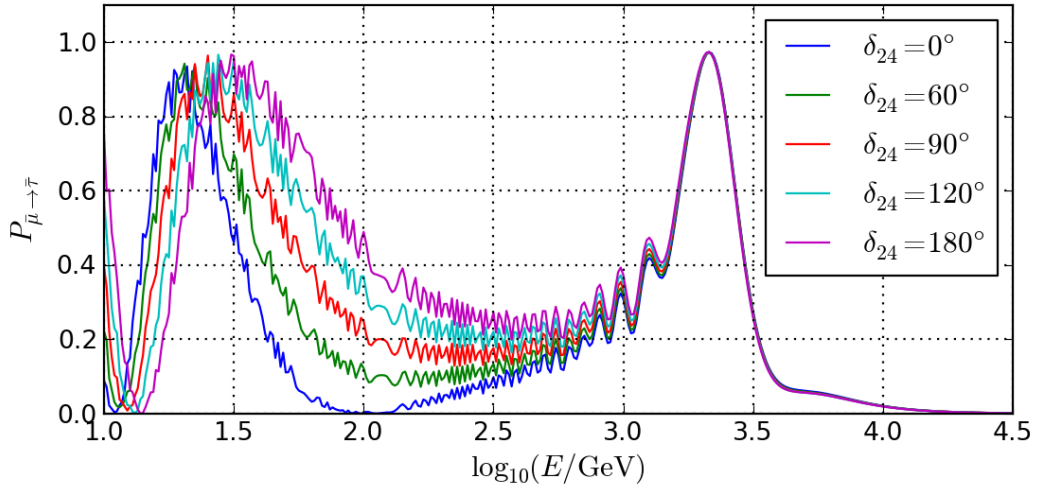
take part in the oscillation process. For the purpose of verification, changes caused by an alternative parametrization containing δ_{23} , δ_{14} and δ_{24} were also studied.

δ_{23} leads to similar changes like δ_{24} and δ_{34} if all other phases are vanishing (s. fig. A.32, cf. fig. 3.36, fig. A.30). Thus in this case the choices δ_{23} , δ_{34} , or δ_{24} are equivalent if three neutrino sorts are involved. If they are mixing with sterile states, electron neutrinos cause that the phases δ_{34} and δ_{24} do not have completely the same impact, especially in the energy range of $E \approx 10$ GeV (s. fig. 3.39, A.33), just as δ_{13} causes changes in there especially for $\sin^2(\theta_{14}) \neq 0$ (s. fig. A.34, fig. A.35). For $\Delta m_{41}^2 < 0$, δ_{24} and δ_{34} result in changes analog to those described above (s. fig. A.36, cf. fig. 3.36). The same applies for $\Delta m_{32}^2 < 0$ (s. fig. A.37, cf. fig. 3.36). The oscillation effects do not depend on the signs of δ_{ij} with $0^\circ \leq |\delta_{ij}| \leq 180^\circ$ (s. fig. A.38). They are 360° -periodic via construction. The oscillation probabilities of $\Delta m_{32}^2 \leq 0 \wedge (\delta_{i4} = \pm 180^\circ \wedge \delta_{j4} = 0^\circ, i, j = 2, 3, i \neq j)$ and $\Delta m_{32}^2 \geq 0$ differ from each other due to the different sign of Δm_{31}^2 . So the difference equals fig. 3.2.



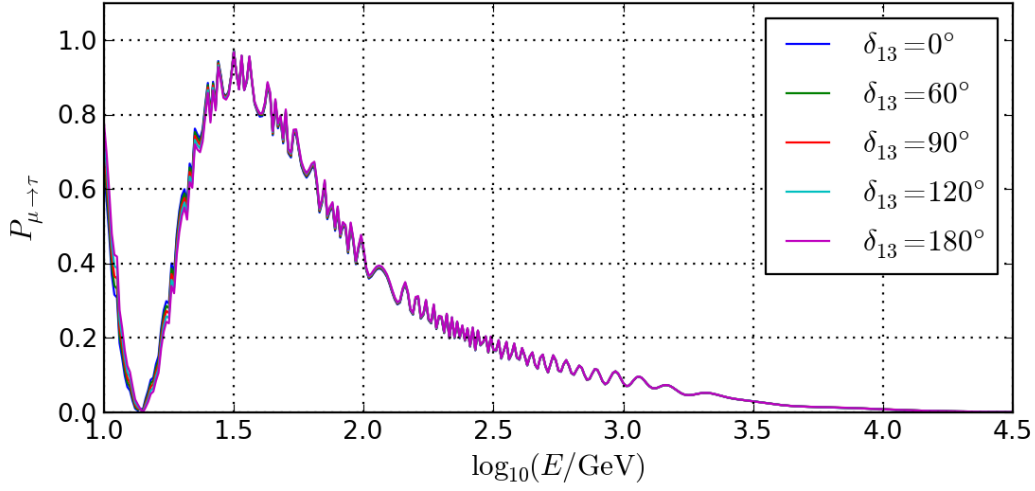
$$\begin{aligned} \Delta m_{41}^2 &= 1.00 \text{ eV}^2 & s_{14}^2 &= 0.050 & s_{24}^2 &= 0.030 & s_{34}^2 &= 0.040 & \delta_{13} &= 0^\circ & \delta_{34} &= 0^\circ \\ \Delta m_{21}^2 &= 7.59 \cdot 10^{-5} \text{ eV}^2 & \Delta m_{31}^2 &= 2.51 \cdot 10^{-3} \text{ eV}^2 & s_{12}^2 &= 0.319 & s_{13}^2 &= 0.024 & s_{23}^2 &= 0.400 \end{aligned}$$

Figure 3.36: Probability $P_{\mu \rightarrow \tau}$ for a vertically incoming muon neutrino generated in the atmosphere to reach the detector as a tau neutrino, for various $\delta_{24} \neq 0^\circ$ with $\delta_{34} = \delta_{13} = 0^\circ$. E is the neutrino energy.



$$\begin{aligned} \Delta m_{41}^2 &= 1.00 \text{ eV}^2 & s_{14}^2 &= 0.050 & s_{24}^2 &= 0.030 & s_{34}^2 &= 0.040 & \delta_{13} &= 0^\circ & \delta_{34} &= 0^\circ \\ \Delta m_{21}^2 &= 7.59 \cdot 10^{-5} \text{ eV}^2 & \Delta m_{31}^2 &= 2.51 \cdot 10^{-3} \text{ eV}^2 & s_{12}^2 &= 0.319 & s_{13}^2 &= 0.024 & s_{23}^2 &= 0.400 \end{aligned}$$

Figure 3.37: Probability $P_{\bar{\mu} \rightarrow \bar{\tau}}$ for a vertically incoming muon antineutrino generated in the atmosphere to reach the detector as a tau antineutrino, for various $\delta_{24} \neq 0^\circ$ with $\delta_{34} = \delta_{13} = 0^\circ$. E is the neutrino energy.



$$\begin{aligned} \Delta m_{41}^2 &= 1.00 \text{ eV}^2 & s_{14}^2 &= 0.050 & s_{24}^2 &= 0.030 & s_{34}^2 &= 0.040 & \delta_{24} &= 0^\circ & \delta_{34} &= 0^\circ \\ \Delta m_{21}^2 &= 7.59 \cdot 10^{-5} \text{ eV}^2 & \Delta m_{31}^2 &= 2.51 \cdot 10^{-3} \text{ eV}^2 & s_{12}^2 &= 0.319 & s_{13}^2 &= 0.024 & s_{23}^2 &= 0.400 \end{aligned}$$

Figure 3.38: Probability $P_{\mu \rightarrow \tau}$ for a vertically incoming muon neutrino generated in the atmosphere to reach the detector as a tau neutrino, for various $\delta_{13} \neq 0^\circ$ with $\delta_{24} = \delta_{34} = 0^\circ$. E is the neutrino energy.

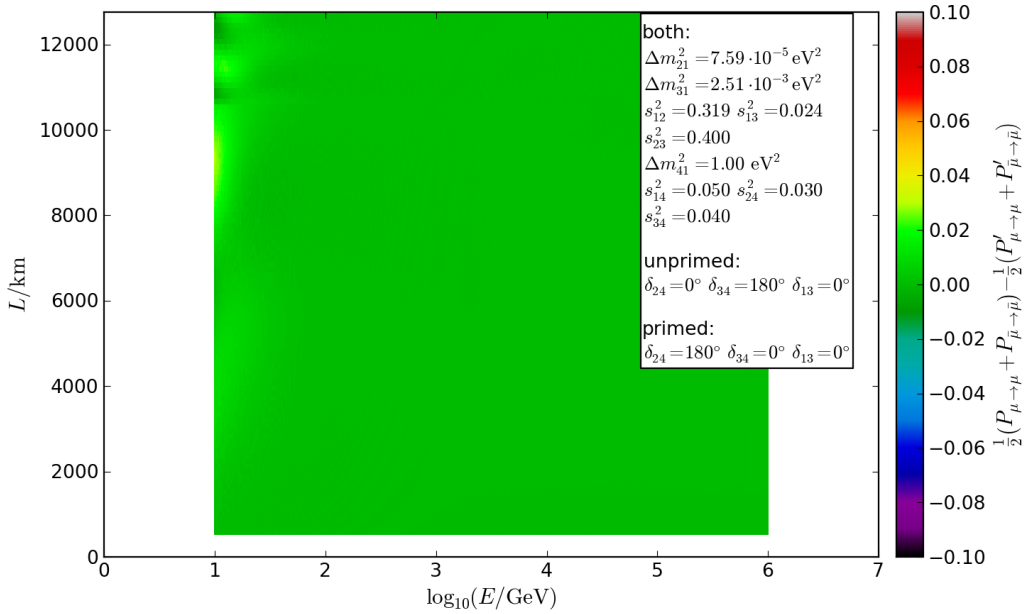


Figure 3.39: Difference $\frac{1}{2} (P_{\mu \rightarrow \mu} + P_{\bar{\mu} \rightarrow \bar{\mu}}) - \frac{1}{2} (P'_{\mu \rightarrow \mu} + P'_{\bar{\mu} \rightarrow \bar{\mu}})$ between the probabilities, averaged over muon neutrinos and antineutrinos, for a particle generated in the atmosphere to reach the detector in the same state in which it was generated, between $\delta_{34} = 180^\circ$, $\delta_{24} = \delta_{13} = 0^\circ$ (unprimed) and $\delta_{24} = 180^\circ$, $\delta_{34} = \delta_{13} = 0^\circ$ (primed). L is the path length through the Earth (s. fig. 2.2), E is the neutrino energy.

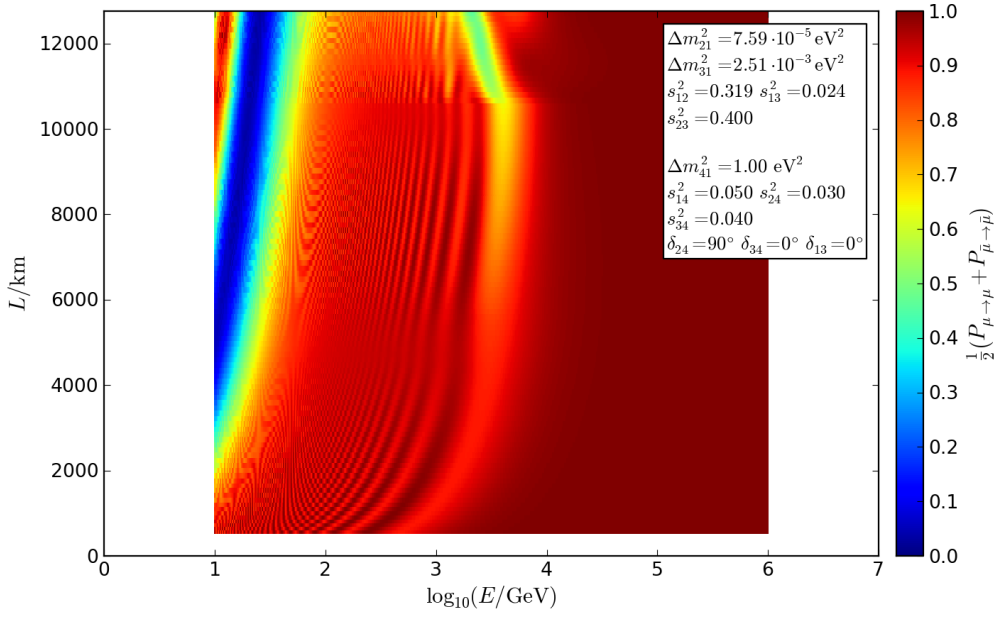


Figure 3.40: Probability $\frac{1}{2} (P_{\mu \rightarrow \mu} + P_{\bar{\mu} \rightarrow \bar{\mu}})$, averaged over muon neutrinos and antineutrinos, for a particle generated in the atmosphere to reach the detector in the same state in which it was generated. L is the path length through the Earth (s. fig. 2.2), E is the neutrino energy.

In order to give an indication of measurable values, fig. 3.40 shows $\frac{1}{2} (P_{\mu \rightarrow \mu} + P_{\bar{\mu} \rightarrow \bar{\mu}})$ for the example presented in fig. 3.34 and fig. 3.35. Compared to fig. 3.31, in which all phases are vanishing, differences exist in the area of the low-energy oscillations for long path lengths. The minimum is deeper and shift towards higher energies for larger δ_{24} . A comparison of $\frac{1}{2} (P_{\mu \rightarrow \mu} + P_{\bar{\mu} \rightarrow \bar{\mu}})$ for various δ_{24} at maximum path length can be found in fig. A.39.

3.7 Errors on the known parameters

Oscillations among the known neutrino states are strongly suppressed in the TeV range. For that reason, the errors of the chosen conventional parameters do not affect the shape in the TeV range. It was tested that variations of the value of Δm_{32}^2 in the 2σ -range and variations of θ_{23} around $\pm 15\%$ only lead to changes for energies $E < 100$ GeV. So that is not a restriction on the later analyses, because this energy range is barely included in the data set (s. fig. 2.3).

Chapter 4

3+2 model

The subject of this chapter is the 3+2 model. It allows the theoretical description of the LSND as well as the MiniBooNe data [6][1]. After all the changes that are caused by the additional parameters of one single sterile state have been covered in part 3, now the interaction of the parameters of two sterile states is studied. The goal is to identify relevant parameters by looking at the interaction of the effects, provided that there are two sterile states.

4.1 Impact of θ_{45}

Because sterile neutrinos do not take part in the weak interaction, it is actually not possible to associate a flavor state with them as already mentioned in part 1.1.1. Therefore, existing interactions among sterile states can not be recognized experimentally. Thus, w.l.o.g., $\sin^2(\theta_{45})$ can be set to any value $0 \leq \sin^2(\theta_{45}) \leq 1$. Most practical is $\sin^2(\theta_{45}) = 0$. Other choices do not change measurable oscillation probabilities, but instead just change the transition probabilities of both sterile states into each other. $P_{\mu \rightarrow s1} + P_{\mu \rightarrow s2}$ and $P_{\bar{\mu} \rightarrow s1} + P_{\bar{\mu} \rightarrow s2}$ are constant for all choices of θ_{45} . The probabilities $P_{\mu \rightarrow e}$, $P_{\mu \rightarrow \tau}$, $P_{\mu \rightarrow \mu}$, $P_{\bar{\mu} \rightarrow e}$, $P_{\bar{\mu} \rightarrow \tau}$, and $P_{\bar{\mu} \rightarrow \bar{\mu}}$ are identical, too.

4.2 Impact of the relative sign of Δm_{41}^2 and Δm_{51}^2

4.2.1 $\sin^2(\theta_{24}) = \sin^2(\theta_{25}) \neq 0$, $\sin^2(\theta_{ij}) = 0$ with $i = 1, 3$, $j = 4, 5$

By examination of the most simple case $\sin^2(\theta_{24}) = \sin^2(\theta_{25}) \neq 0$, $\sin^2(\theta_{ij}) = 0$ with $i = 1, 3$; $j = 4, 5$, in this section the impact of the relative of Δm_{41}^2 and Δm_{51}^2 is going to be analyzed.

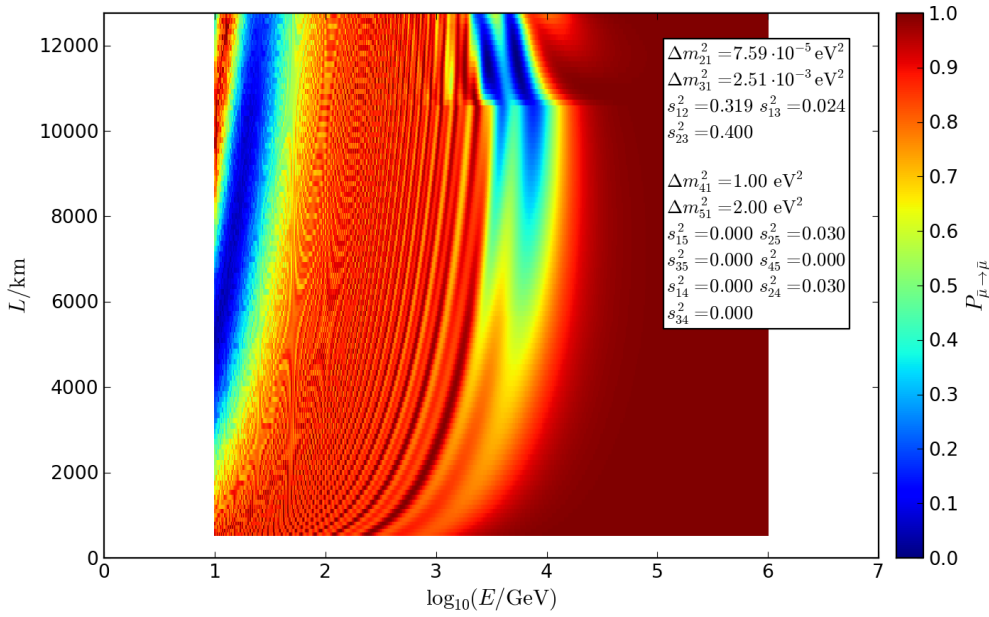


Figure 4.1: Probability $P_{\bar{\mu} \rightarrow \bar{\mu}}$ for a muon antineutrino generated in the atmosphere to reach the detector as a muon antineutrino. L is the path length through the Earth (s. fig. 2.2), E is the neutrino energy.

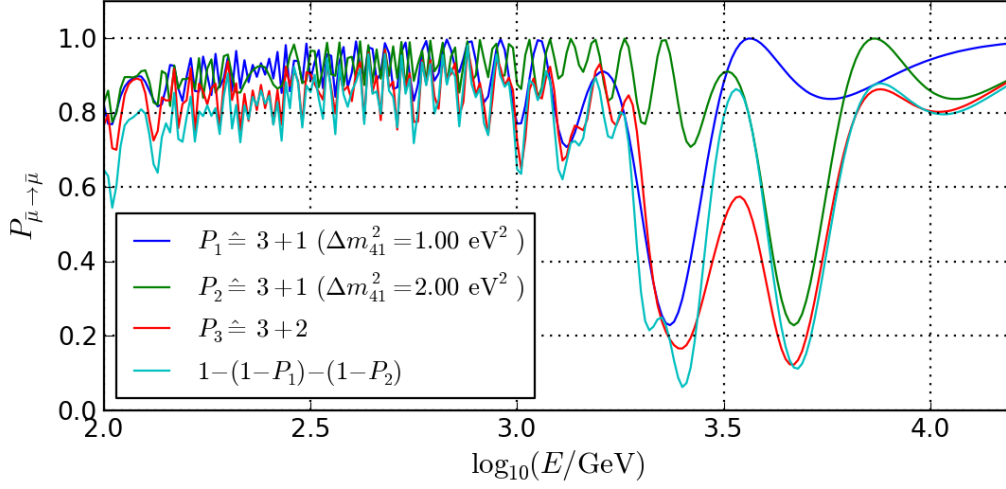
$$\Delta m_{41}^2, \Delta m_{51}^2 > 0 \text{ or } \Delta m_{41}^2, \Delta m_{51}^2 < 0$$

In chapter 3 it has been explained that for $\Delta m_{41}^2 > 0$ and $\sin^2(\theta_{24}) \neq 0$ resonances between muon and sterile neutrinos occur in the antiparticle channel.

Analog, there are two resonate oscillations in the antiparticle channel for $\Delta m_{41}^2, \Delta m_{51}^2 > 0$. An example for a situation in which only muon neutrinos mix with sterile and in which the parameters have been chosen symmetrically is given in fig. 4.1. The resonances affect each other. If this was not the case, they would have been shifted on the x-axis but would have had the same shape. Fig. (Abb. 4.2) serves further illustration: $P_{\bar{\mu} \rightarrow \bar{\mu}}$ for the 3+2 model (red line) is shown together with the probabilities that come around in the 3+1 model for $\Delta m_{41}^2 = 1 \text{ eV}^2$ ($=: P_1$, dark blue line) and $\Delta m_{41}^2 = 2 \text{ eV}^2$ ($=: P_2$, green line). It can be seen that the probability in the 3+2 model does not match $1 - (1 - P_1) - (1 - P_2)$ (cyan line), $\min(P_1, P_2)$, or $\frac{1}{2}(P_{\mu \rightarrow \mu} + P_{\bar{\mu} \rightarrow \bar{\mu}})$ (s. fig. B.1).

One reason for this is that the number of muon antineutrinos inside the Earth depends on how many of them already oscillated into one of the two sterile states. Therefore, both probabilities strongly influence each other. Mathematically, there is no reason to assume that the differential equation that describes the evolution of the states (1.13) separates fully.

By comparison of fig. 4.1 and fig. 3.3, differences of the oscillation probabilities in the region between the low-energy oscillation and the first minimum can be identified. Furthermore, by looking at figures with different values for $\Delta m_{41}^2, \Delta m_{51}^2$ but the same mixing angles (fig. 4.3, fig. B.2), different periodicities of this differences are visible. Hence a beat due to Δm_{54}^2 can be observed.



$$\begin{aligned} \Delta m_{41}^2 &= 1.00 \text{ eV}^2 & \Delta m_{51}^2 &= 2.00 \text{ eV}^2 & s_{24}^2 &= s_{25}^2 = 0.030 & s_{i4}^2 &= s_{i5}^2 = 0 \quad (i=1,3) \\ \Delta m_{21}^2 &= 7.59 \cdot 10^{-5} \text{ eV}^2 & \Delta m_{31}^2 &= 2.51 \cdot 10^{-3} \text{ eV}^2 & s_{12}^2 &= 0.319 & s_{13}^2 &= 0.024 & s_{23}^2 &= 0.400 \end{aligned}$$

Figure 4.2: Probability $P_{\bar{\mu} \rightarrow \bar{\mu}}$ for a vertically incoming muon antineutrino generated in the atmosphere to reach the detector as a muon antineutrino. E is the neutrino energy.

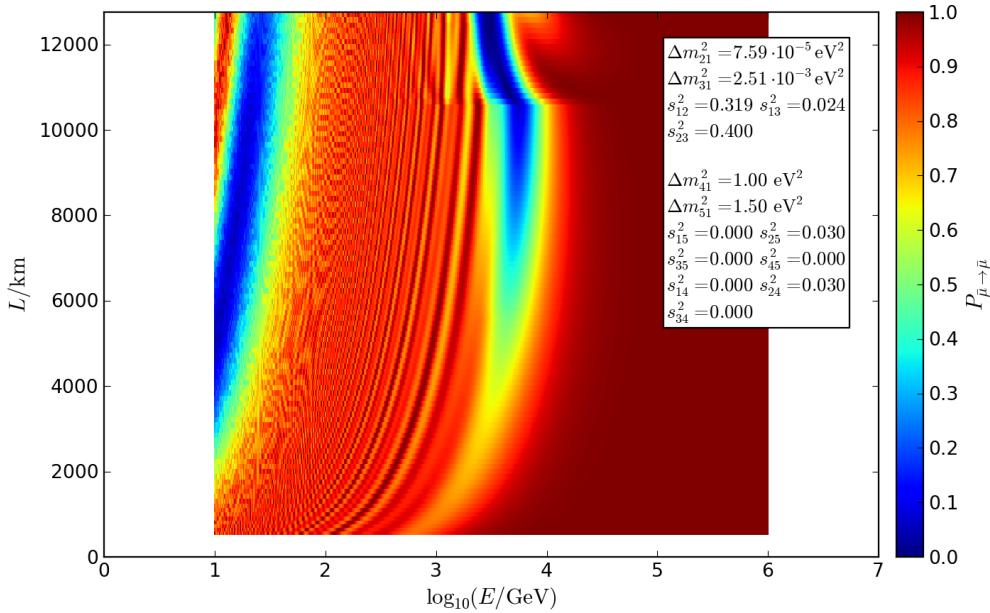
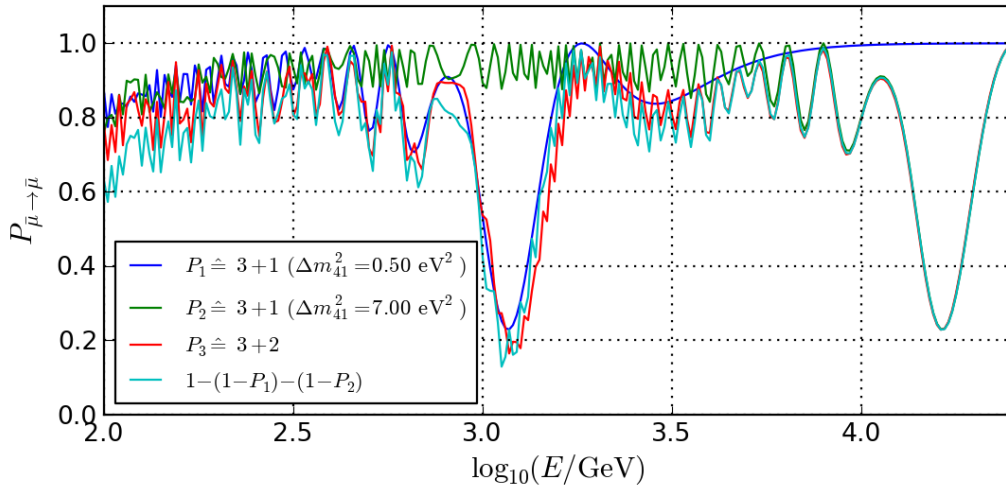


Figure 4.3: Probability $P_{\bar{\mu} \rightarrow \bar{\mu}}$ for a muon antineutrino generated in the atmosphere to reach the detector as a muon antineutrino. L is the path length through the Earth (s. fig. 2.2), E is the neutrino energy.



$$\begin{aligned} \Delta m_{41}^2 &= 1.00 \text{ eV}^2 & \Delta m_{51}^2 &= 7.00 \text{ eV}^2 & s_{24}^2 &= s_{25}^2 = 0.030 & s_{i4}^2 &= s_{i5}^2 = 0 \quad (i=1,3) \\ \Delta m_{21}^2 &= 7.59 \cdot 10^{-5} \text{ eV}^2 & \Delta m_{31}^2 &= 2.51 \cdot 10^{-3} \text{ eV}^2 & s_{12}^2 &= 0.319 & s_{13}^2 &= 0.024 & s_{23}^2 &= 0.400 \end{aligned}$$

Figure 4.4: Probability $P_{\bar{\mu} \rightarrow \bar{\mu}}$ for a vertically incoming muon antineutrino generated in the atmosphere to reach the detector as a muon antineutrino. E is the neutrino energy.

The smaller values $\Delta m_{51}^2 - \Delta m_{41}^2 = \Delta m_{54}^2$ takes, the more the oscillations influence each other (cf. fig. 4.2, fig. 4.4). For symmetrical choice of $\sin^2(\theta_{24})$ and $\sin^2(\theta_{25})$, the minima can not be separated anymore for $\Delta m_{51}^2 \div \Delta m_{41}^2 \lesssim \frac{3}{2}$ (s. fig. 4.3).

Instead of two separated minima there is now a clear single minimum. The corresponding probability $\frac{1}{2}(P_{\mu \rightarrow \mu} + P_{\bar{\mu} \rightarrow \bar{\mu}})$ (s. fig. 4.5) clearly differs from the corresponding probability in the 3+1 model with $\Delta m_{41}^2 = 1\text{eV}^2$, $\sin^2(\theta_{24}) = 0.03$, $\sin^2(\theta_{34}) = \sin^2(\theta_{14}) = 0.00$ (s. fig. 4.5, cf. fig. 3.8).

The minimum is much more pronounced and reaches longer path lengths.

In part 3.2 it has already been shown that the resonance is shifted to the particle channel in case of one single sterile state with $\Delta m_{41}^2 < 0$. The measurable probability $\frac{1}{2}(P_{\mu \rightarrow \mu} + P_{\bar{\mu} \rightarrow \bar{\mu}})$ stays the same in good approximation. Likewise, here, both resonances are shifted to the particle channel for $\Delta m_{41}^2 < 0$ and $\Delta m_{51}^2 < 0$ (s. fig. B.3). $\frac{1}{2}(P_{\mu \rightarrow \mu} + P_{\bar{\mu} \rightarrow \bar{\mu}})$ does almost not change. In part 1.2, w.l.o.g., $|\Delta m_{41}^2| < |\Delta m_{51}^2|$ has been defined. Another definition that depends on which sterile state is heavier and which is lighter is not advisable, because these cases can not be differentiated. The difference between $\Delta m_{32}^2 > 0$ and $\Delta m_{32}^2 < 0$ is the same as it is without sterile states (s. fig. 3.2).

$$(\Delta m_{41}^2 < 0 \wedge \Delta m_{51}^2 > 0) \text{ or } (\Delta m_{41}^2 > 0 \wedge \Delta m_{51}^2 < 0)$$

An example for a situation with $(\Delta m_{41}^2 > 0 \wedge \Delta m_{51}^2 < 0)$ is given by fig. 4.6. The plot shows $\frac{1}{2}(P_{\mu \rightarrow \mu} + P_{\bar{\mu} \rightarrow \bar{\mu}})$ for $\Delta m_{51}^2 = -1.50\text{eV}^2$, with all other parameters as in fig. 4.5. If the signs of Δm_{41}^2 and Δm_{51}^2 are different, the resonance between muon neutrinos and

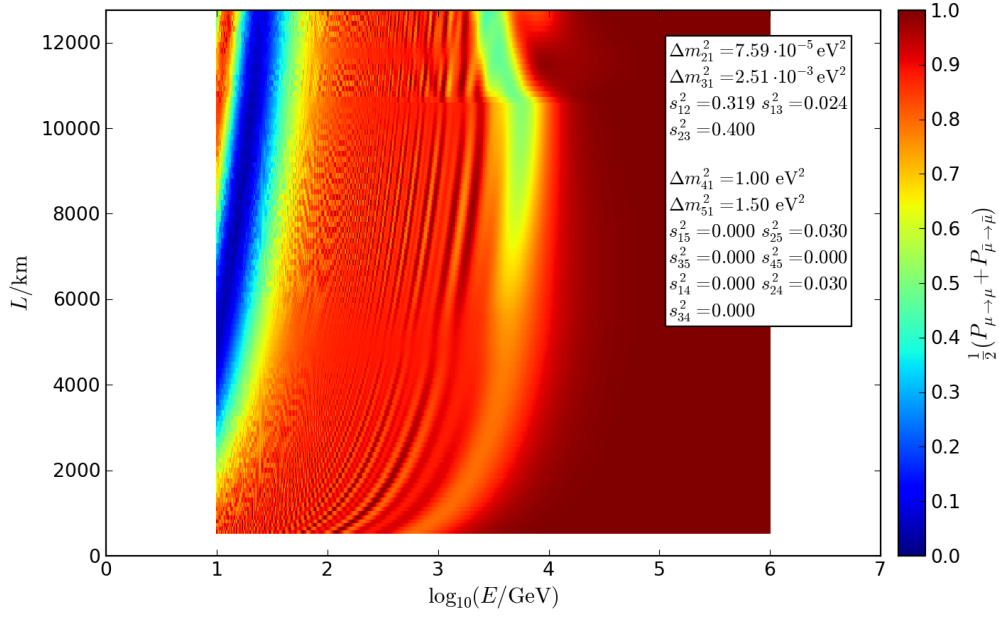


Figure 4.5: Probability $\frac{1}{2}(P_{\mu \rightarrow \mu} + P_{\bar{\mu} \rightarrow \bar{\mu}})$, averaged over muon neutrinos and antineutrinos, for a particle generated in the atmosphere to reach the detector in the same state in which it was generated. L is the path length through the Earth (s. fig. 2.2), E is the neutrino energy.

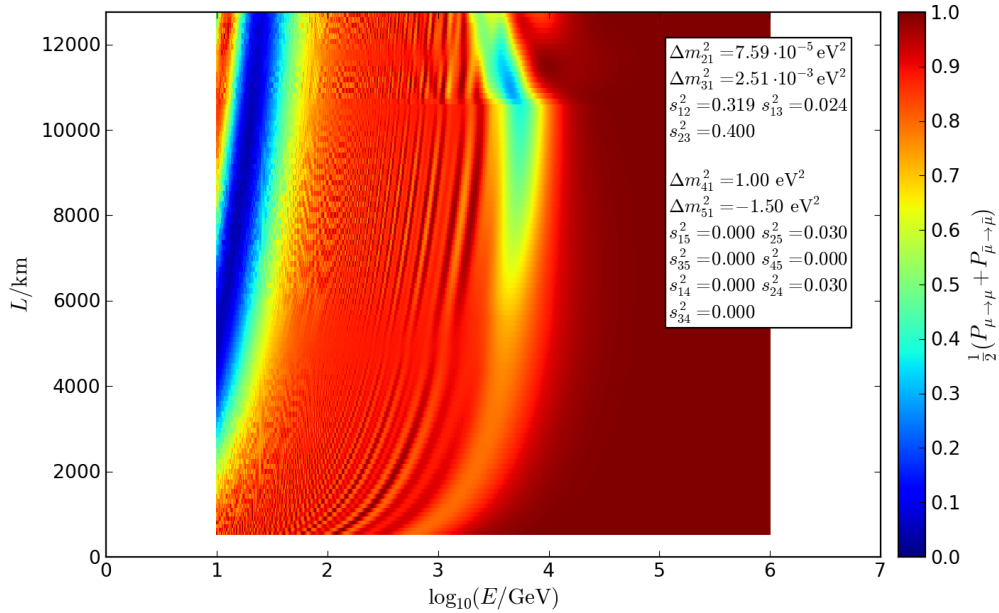
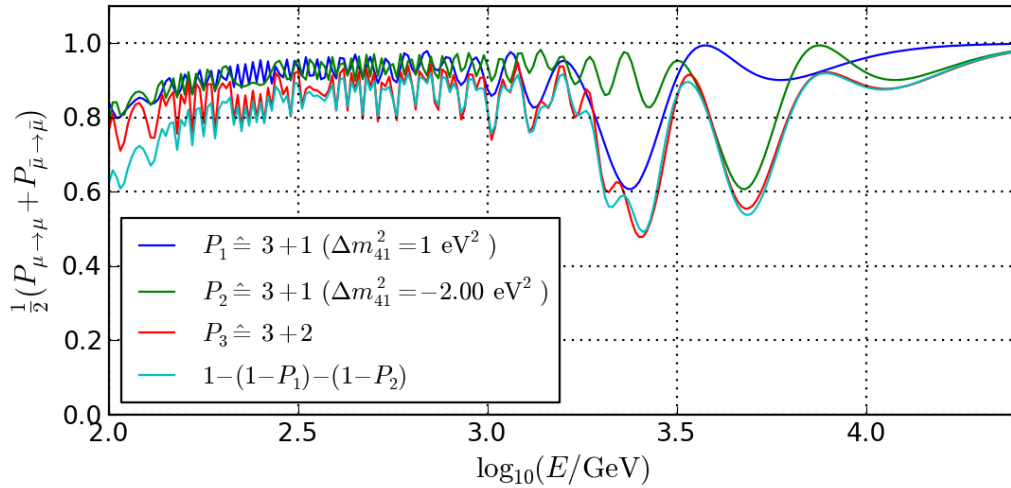


Figure 4.6: Probability $\frac{1}{2}(P_{\mu \rightarrow \mu} + P_{\bar{\mu} \rightarrow \bar{\mu}})$, averaged over muon neutrinos and antineutrinos, for a particle generated in the atmosphere to reach the detector in the same state in which it was generated. L is the path length through the Earth (s. fig. 2.2), E is the neutrino energy.



$$\begin{aligned} \Delta m_{41}^2 &= 1.00 \text{ eV}^2 & \Delta m_{51}^2 &= -2.00 \text{ eV}^2 & s_{24}^2 = s_{25}^2 &= 0.030 & s_{i4}^2 = s_{i5}^2 &= 0 \quad (i=1,3) \\ \Delta m_{21}^2 &= 7.59 \cdot 10^{-5} \text{ eV}^2 & \Delta m_{31}^2 &= 2.51 \cdot 10^{-3} \text{ eV}^2 & s_{12}^2 &= 0.319 & s_{13}^2 &= 0.024 & s_{23}^2 &= 0.400 \end{aligned}$$

Figure 4.7: Probability $\frac{1}{2}(P_{\mu \rightarrow \mu} + P_{\bar{\mu} \rightarrow \bar{\mu}})$, averaged over muon neutrinos and antineutrinos, for a vertically incoming particle generated in the atmosphere to reach the detector in the same state in which it was generated. E is the neutrino energy.

the sterile state for which $\Delta m_{i1}^2 < 0$ applies is shifted to the particle channel (s. fig. B.4, fig. B.5).

Now both oscillations occur in separated channels. Hence they influence each other much less (cf. fig. 4.5, fig. 4.6; s. fig. 4.7, cf. fig. B.1). In fig. 4.6 two minima can be separated at high path lengths, in fig. 4.5 they can not. Furthermore we can take from the plots that the integrated probability $\frac{1}{2}(P_{\mu \rightarrow \mu} + P_{\bar{\mu} \rightarrow \bar{\mu}})$ in fig. 4.5 is larger, as the minimum is both thinner and less deep. Only if the signs of Δm_{41}^2 and Δm_{51}^2 are different, values of $\frac{1}{2}(P_{\mu \rightarrow \mu} + P_{\bar{\mu} \rightarrow \bar{\mu}}) < \frac{1}{2}$ can occur. In case of $\Delta m_{41}^2, \Delta m_{51}^2 \gtrless 0$, $\frac{1}{2}(P_{\mu \rightarrow \mu} + P_{\bar{\mu} \rightarrow \bar{\mu}}) \gtrsim \frac{1}{2}$.

For lower energies, more distinct differences exist (s. fig. 4.7). Changes of the conventional oscillations arise comparable to those in the 3+1 model for $\sin^2(\theta_{24}) \neq 0$ (s. part 3.2). There, the minimum of $\frac{1}{2}(P_{\mu \rightarrow \mu} + P_{\bar{\mu} \rightarrow \bar{\mu}})$ levels off slightly and shifts to higher energies (s. fig. 3.7). Similar effects can be observed in the 3+2 model and cause changes in the area of the conventional oscillations.

The probabilities $\frac{1}{2}(P_{\mu \rightarrow \mu} + P_{\bar{\mu} \rightarrow \bar{\mu}})$ are almost equal for $(\Delta m_{41}^2 < 0 \wedge \Delta m_{51}^2 > 0)$ and $(\Delta m_{41}^2 > 0 \wedge \Delta m_{51}^2 < 0)$ (s. fig. B.6).

There are not differences between $\Delta m_{32}^2 > 0$ and $\Delta m_{32}^2 < 0$ that do not occur without sterile states.

4.2.2 General unsymmetrical case

The signs of the mass-squared differences determine the channels in which resonances are possible. $\Delta m_{i1}^2 > 0$ and $\sin^2(\theta_{2i}) \neq 0$ with $i = 4, 5$ enable resonant oscillations in the

TeV range between muon neutrinos and the corresponding sterile state in the antiparticle channel. If also $\sin^2(\theta_{3i}) \neq 0$ applies, additional resonances of the oscillation between muon and tau antineutrinos arise (s. fig. 4.8). $\Delta m_{i1}^2 < 0$ results in nearly identical resonances in the particle channel, provided that the sign of the other sterile mass-squared difference changes, too (s. fig. 4.9, cf. fig. 4.8). Attention should be paid to the fact that the examination is much more complex for $\theta_{45} \neq 0$. In this case, a sterile "flavor state" contains different amounts of the mass states, so that in case of unequal signs resonances can arise in both channels for each "flavor state" (s. fig. B.7, fig. B.8). Still the sums $P_{\bar{\mu} \rightarrow \bar{s}1} + P_{\bar{\mu} \rightarrow \bar{s}2}$ and $P_{\mu \rightarrow s1} + P_{\mu \rightarrow s2}$ are equal (cf. fig. B.9, fig. B.10; cf. fig. B.11, fig. B.12). Because there are no differences regarding the transition probabilities into the known states (cf. fig. 4.6, fig. B.13), the choice $\theta_{45} = 0$ is w.l.o.g. possible and quite useful. Independent of that, the relative signs of the Δm_{i1}^2 is a relevant parameter, because two resonances in the same channel influence each other more than in separated channels. This result does not depend on the definition of θ_{45} .

For $\sin^2(\theta_{34}) \neq 0 \vee \sin^2(\theta_{35}) \neq 0$ the conventional oscillations change similarly to the way they do in the 3+1 model for $\sin^2(\theta_{34}), \sin^2(\theta_{24}) \neq 0$ (s. fig. 4.9). $\sin^2(\theta_{24}) \cdot \sin^2(\theta_{34})$ is the most important parameter for the changes in the 3+1 model, where a dependency on $|\Delta m_{41}^2|$ exists as well. In the 3+2 model the most important parameters are $|\Delta m_{41}^2|$, $\sin^2(\theta_{24}) \cdot \sin^2(\theta_{34})$, $|\Delta m_{51}^2|$, and $\sin^2(\theta_{25}) \cdot \sin^2(\theta_{35})$ (cf. fig. 4.9, fig. 4.10) and not, e.g., $\sin^2(\theta_{24}) \cdot \sin^2(\theta_{34}) + \sin^2(\theta_{25}) \cdot \sin^2(\theta_{35})$ (cf. fig. 4.9, fig. B.14).

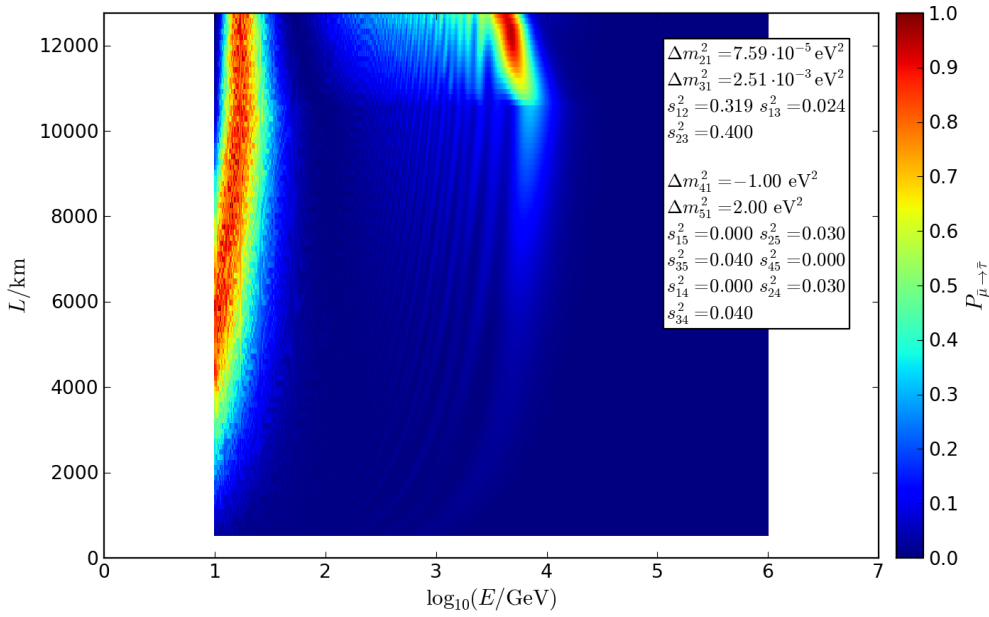


Figure 4.8: Probability $P_{\bar{\mu} \rightarrow \bar{\tau}}$ for a muon antineutrino generated in the atmosphere to reach the detector as a tau antineutrino. L is the path length through the Earth (s. fig. 2.2), E is the neutrino energy.

In part 3.4 the differences in the 3+1 model with $\sin^2(\theta_{34}) \neq 0$ that result from various mass hierarchies were discussed in detail. The effects that were described there can be transferred to the mixing angles in the 3+2 model. $\Delta m_{32}^2 > 0$ and $\Delta m_{32}^2 < 0$ in general do not result in identical physical probabilities, especially not for $\sin^2(\theta_{34}) \neq 0 \vee \sin^2(\theta_{35}) \neq 0$.

So usually the physical effects of two different mass hierarchies are different; especially for $\sin^2(\theta_{34}) \neq 0 \vee \sin^2(\theta_{35}) \neq 0$. The cases $\Delta m_{41}^2 > 0 \wedge \Delta m_{51}^2 > 0$, $\Delta m_{41}^2 < 0 \wedge \Delta m_{51}^2 < 0$, and $\Delta m_{41}^2 < 0 \wedge \Delta m_{51}^2 > 0$, $\Delta m_{41}^2 > 0 \wedge \Delta m_{51}^2 < 0$ can differ from each other by corrections, but they are quite similar.

By a look at $\frac{1}{2}(P_{\mu \rightarrow \mu} + P_{\bar{\mu} \rightarrow \bar{\mu}})$ for the example in fig. 4.9 it becomes apparent that the chosen values in the 3+2 model definitely break exclusion limits, because transition probabilities $\approx \frac{1}{2}$ arise in the whole area between around 10 GeV and 10 TeV for long path lengths (s. fig. 4.11). This conclusion holds for equal signs, too (s. fig. B.15). With respect to single mixing angles, the parameter space in the 3+2 model might be the subject of stricter restrictions than in the 3+1 model. In fig. 4.11, only the values of $\sin^2(\theta_{24})$ and $\sin^2(\theta_{34})$ are larger than in fig. 4.12. The integral of the probability $\frac{1}{2}(P_{\mu \rightarrow \mu} + P_{\bar{\mu} \rightarrow \bar{\mu}})$ is clearly smaller than in fig. 4.12. So boundary values can not refer to single mixing angles, but only to matrix entries of (1.8).

Even in the 3+2 model, effects due to the mixing angles θ_{14} , θ_{15} are small compared to those caused by the other mixing angles (cf. fig. 4.5, fig. B.16, cf. fig. 4.13, fig. 4.15).

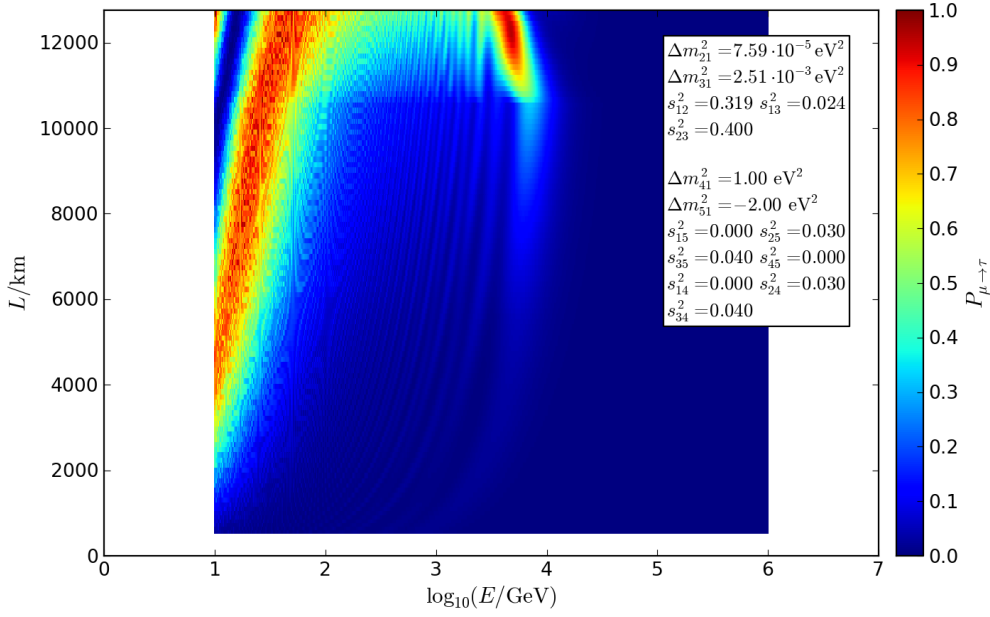


Figure 4.9: Probability $P_{\mu \rightarrow \tau}$ for a muon neutrino generated in the atmosphere to reach the detector as a tau neutrino. L is the path length through the Earth (s. fig. 2.2), E is the neutrino energy.

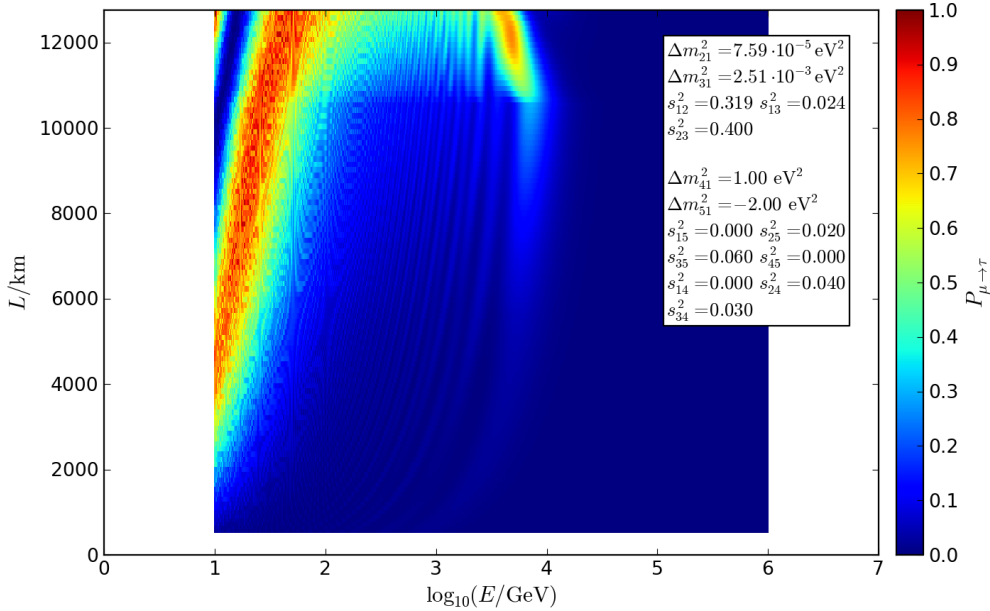


Figure 4.10: Probability $P_{\mu \rightarrow \tau}$ for a muon neutrino generated in the atmosphere to reach the detector as a tau neutrino. L is the path length through the Earth (s. fig. 2.2), E is the neutrino energy.

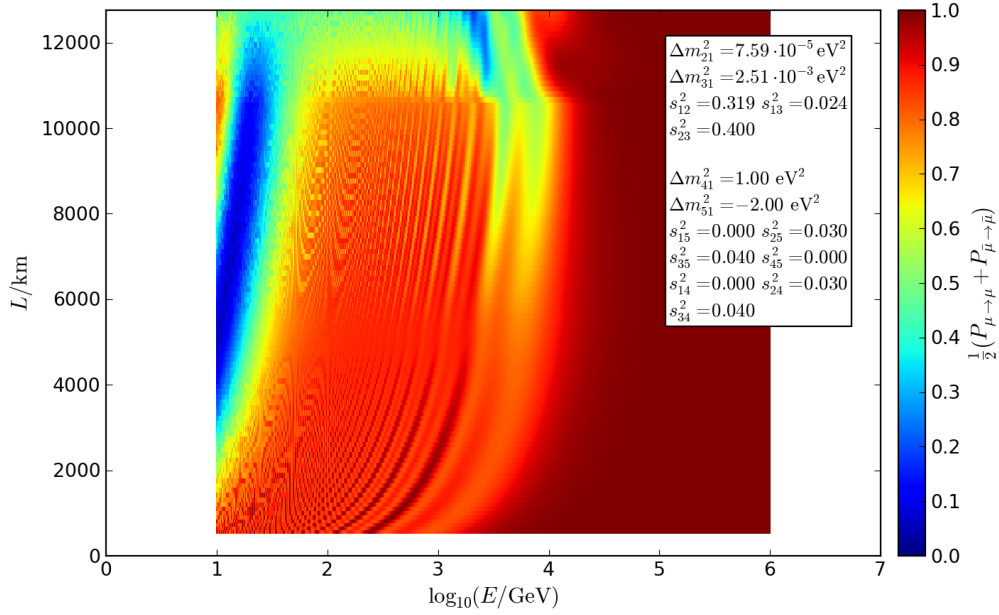


Figure 4.11: Probability $\frac{1}{2} (P_{\mu \rightarrow \mu} + P_{\bar{\mu} \rightarrow \bar{\mu}})$, averaged over muon neutrinos and antineutrinos, for a particle generated in the atmosphere to reach the detector in the same state in which it was generated. L is the path length through the Earth (s. fig. 2.2), E is the neutrino energy.

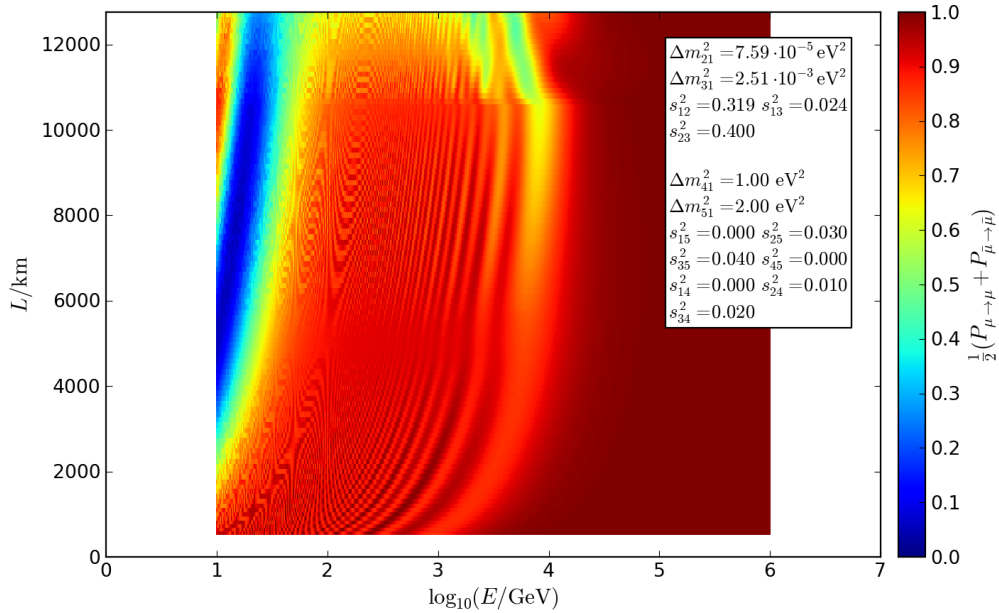


Figure 4.12: Probability $\frac{1}{2} (P_{\mu \rightarrow \mu} + P_{\bar{\mu} \rightarrow \bar{\mu}})$, averaged over muon neutrinos and antineutrinos, for a particle generated in the atmosphere to reach the detector in the same state in which it was generated. L is the path length through the Earth (s. fig. 2.2), E is the neutrino energy.

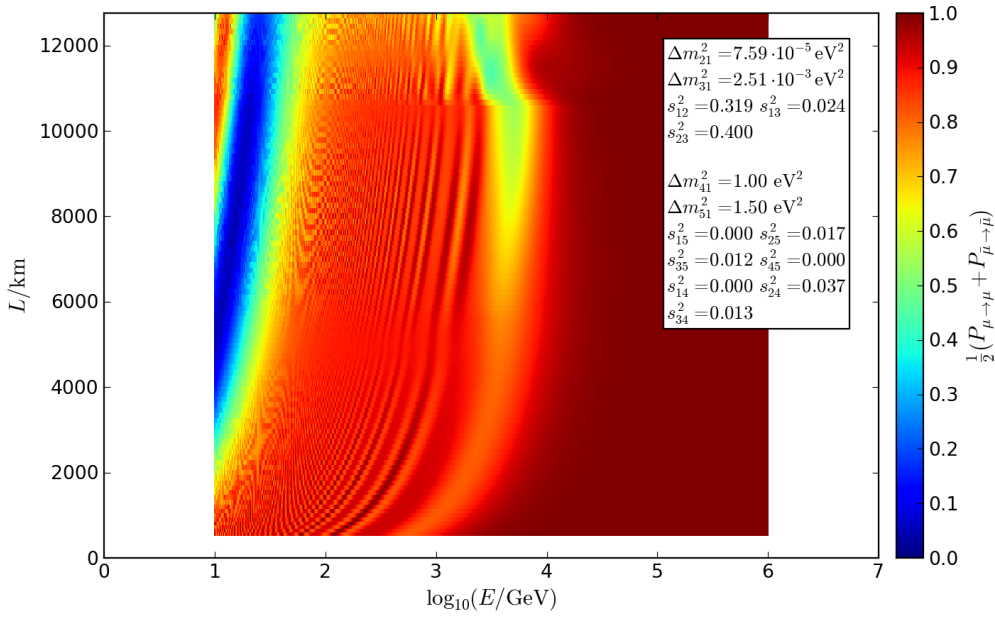


Figure 4.13: Probability $\frac{1}{2} (P_{\mu \rightarrow \mu} + P_{\bar{\mu} \rightarrow \bar{\mu}})$, averaged over muon neutrinos and antineutrinos, for a particle generated in the atmosphere to reach the detector in the same state in which it was generated. L is the path length through the Earth (s. fig. 2.2), E is the neutrino energy.

4.3 Impact of the ratio $\Delta m_{41}^2 \div \Delta m_{51}^2$

The discovery from 4.2.1 that besides $|\Delta m_{41}^2|$ and $|\Delta m_{51}^2|$ the difference $|\Delta m_{41}^2| - |\Delta m_{51}^2|$ is of importance, too, suggests the presumption that the ratio of the mass-squared differences could be essential.

4.3.1 $\Delta m_{41}^2, \Delta m_{51}^2 > 0$ or $\Delta m_{41}^2, \Delta m_{51}^2 < 0$

$$\Delta m_{41}^2 \div \Delta m_{51}^2 \approx 1$$

In part 4.2.1 it was already noticed that minima close to each other can not be separated. Now the focus is on $\Delta m_{41}^2, \Delta m_{51}^2$ very close to each other. An example is shown in fig. 4.14. There is no difference to fig. 3.31. It arises that the sums $c_1 = \sin^2(\theta_{24}) + \sin^2(\theta_{25})$, $c_2 = \sin^2(\theta_{14}) + \sin^2(\theta_{25})$, $c_3 = \sin^2(\theta_{14}) + \sin^2(\theta_{15})$ for symmetric parameter choices result in the same measurable probabilities as in the $3+1$ model with the choice $\sin^2(\theta_{24}) = c_1$, $\sin^2(\theta_{34}) = c_2$, $\sin^2(\theta_{14}) = c_3$. Sterile states with precise identical mass are not distinguishable for us. But for lack of weak interaction a differentiation of such sterile neutrinos in different types is only meaningful if they interact different under some other, unknown interaction. This case will not be discussed. Nevertheless, mass-squared differences at about the size of Δm_{21}^2 are possible. Even smaller differences can not be excluded, especially since sterile neutrinos could even be lighter than the known sorts. Hence on the basis of observations of one single resonance with $\frac{1}{2} (P_{\mu \rightarrow \mu} + P_{\bar{\mu} \rightarrow \bar{\mu}}) \geq 0.5$ it

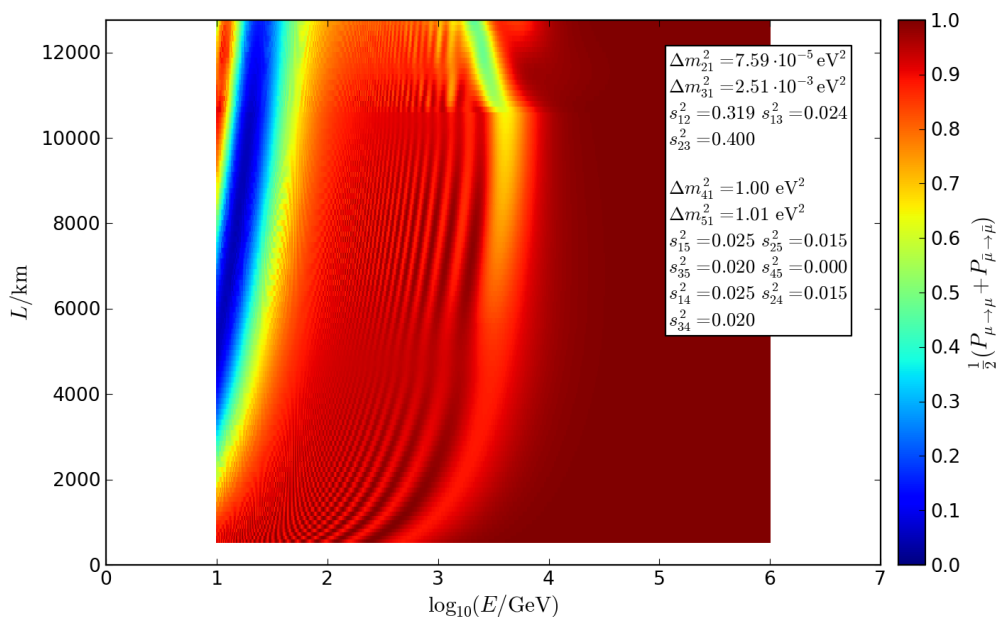


Figure 4.14: Probability $\frac{1}{2} (P_{\mu \rightarrow \mu} + P_{\bar{\mu} \rightarrow \bar{\mu}})$, averaged over muon neutrinos and antineutrinos, for a particle generated in the atmosphere to reach the detector in the same state in which it was generated. L is the path length through the Earth (s. fig. 2.2), E is the neutrino energy.

can not be concluded that there is only one single sterile state. For the number of sterile states, only a lower limit can be set.

Universal case

The relative mass-squared difference is a relevant parameter of the shape of the oscillation effects in the TeV range. For equal ratio and equal mixing angles, the shape stretches on the energy scale like in the 3+1 model (cf. fig. 4.15, fig. 4.16; s. fig. 4.17, cf. fig. 3.29).

There is a linear dependence between the energy at which $\frac{1}{2} (P_{\mu \rightarrow \mu} + P_{\bar{\mu} \rightarrow \bar{\mu}})$ is minimal and Δm_{41}^2 , provided that the ratio to Δm_{51}^2 is constant

This is not surprising, because a linear dependence of the whole shape in the TeV range on Δm_{41}^2 was already observed in the 3+1 model, and the relative mass-squared difference specifies the interaction of the effects. For smaller energies corrections are needed, because the effective muon-tau oscillation relies on the masses of sterile neutrinos for $\sin^2(\theta_{34}) \neq 0$. If the ratio $\Delta m_{54}^2 \div \Delta m_{41}^2$ is not constant, quite different signatures are possible even for equal mixing angles (cf. fig. 4.15, fig. B.17, fig. 4.18). While in fig. 4.15 a single minimum occurs, which separates a little for long path lengths, in fig. B.17 two minima occur, which barely meet. Finally, for even greater gaps two separated minima occur (s. fig. 4.18).

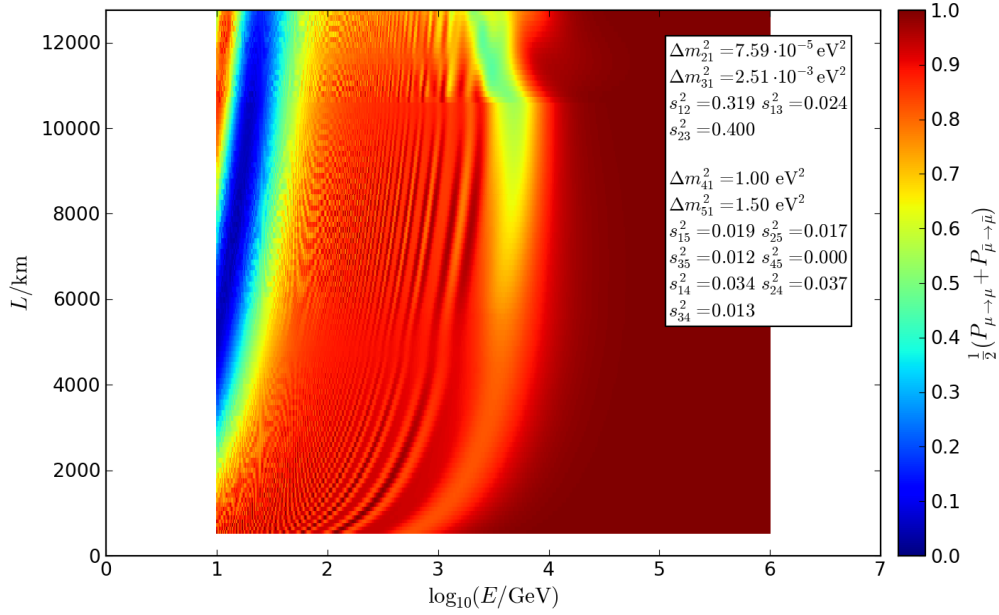


Figure 4.15: Probability $\frac{1}{2} (P_{\mu \rightarrow \mu} + P_{\bar{\mu} \rightarrow \bar{\mu}})$, averaged over muon neutrinos and antineutrinos, for a particle generated in the atmosphere to reach the detector in the same state in which it was generated. L is the path length through the Earth (s. fig. 2.2), E is the neutrino energy.

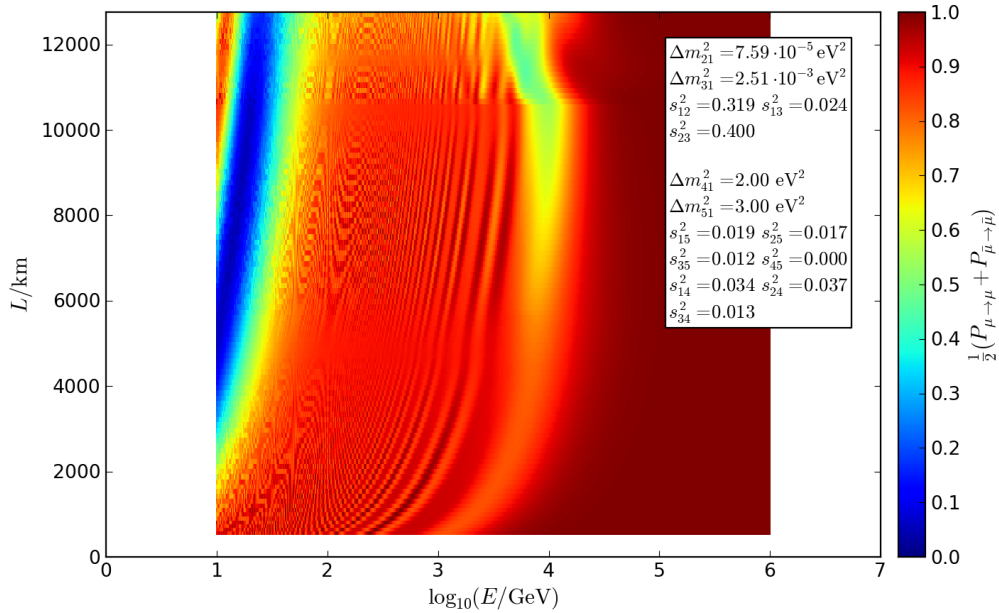


Figure 4.16: Probability $\frac{1}{2} (P_{\mu \rightarrow \mu} + P_{\bar{\mu} \rightarrow \bar{\mu}})$, averaged over muon neutrinos and antineutrinos, for a particle generated in the atmosphere to reach the detector in the same state in which it was generated. L is the path length through the Earth (s. fig. 2.2), E is the neutrino energy.

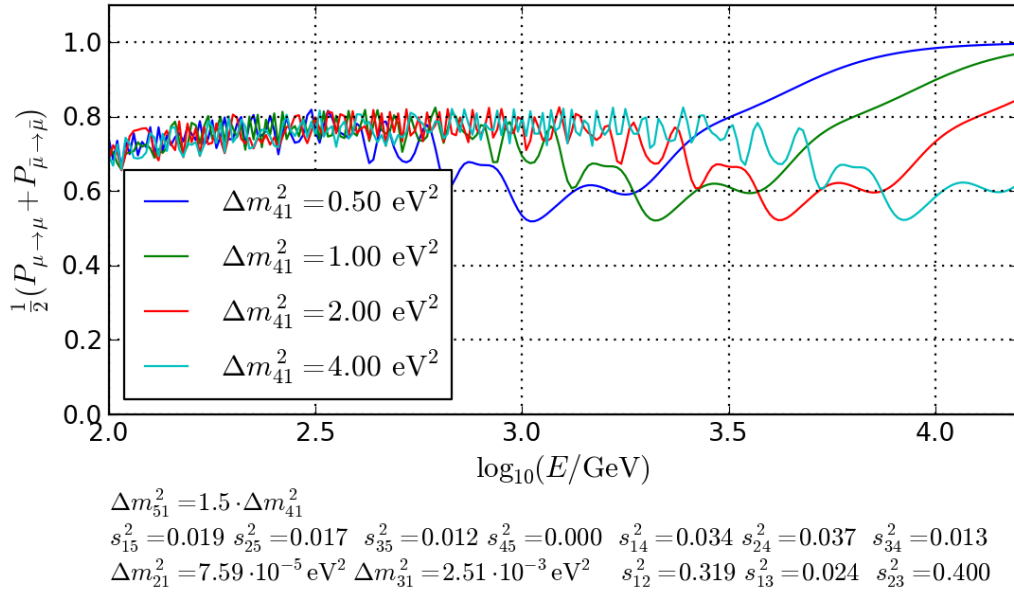


Figure 4.17: Probability $\frac{1}{2} (P_{\mu \rightarrow \mu} + P_{\bar{\mu} \rightarrow \bar{\mu}})$, averaged over muon neutrinos and antineutrinos, for a vertically incoming particle generated in the atmosphere to reach the detector in the same state in which it was generated, for various Δm_{41}^2 with $\Delta m_{41}^2 \div \Delta m_{51}^2 = c = 1.5$. E is the neutrino energy.

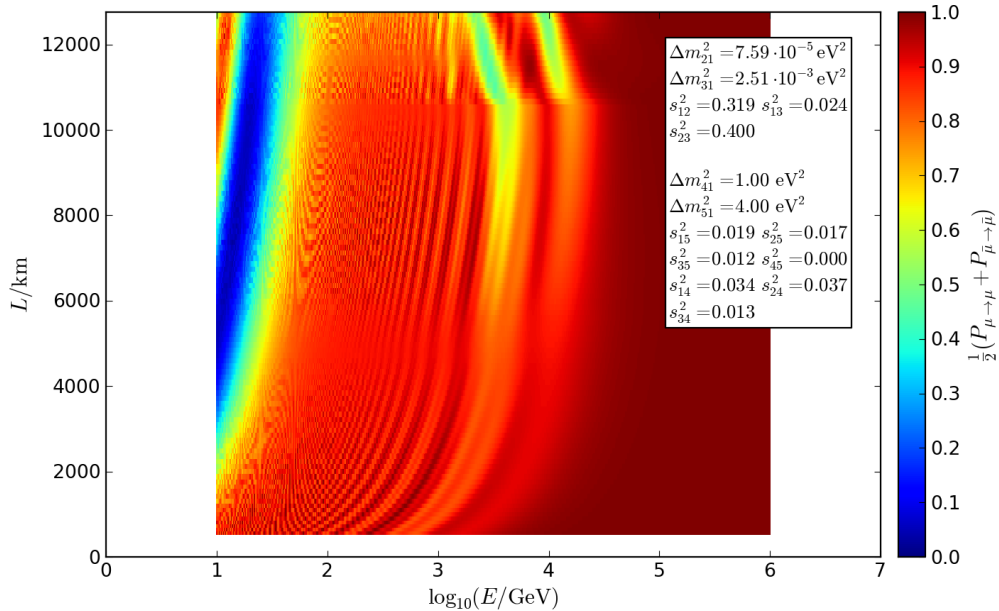


Figure 4.18: Probability $\frac{1}{2} (P_{\mu \rightarrow \mu} + P_{\bar{\mu} \rightarrow \bar{\mu}})$, averaged over muon neutrinos and antineutrinos, for a particle generated in the atmosphere to reach the detector in the same state in which it was generated. L is the path length through the Earth (s. fig. 2.2), E is the neutrino energy.

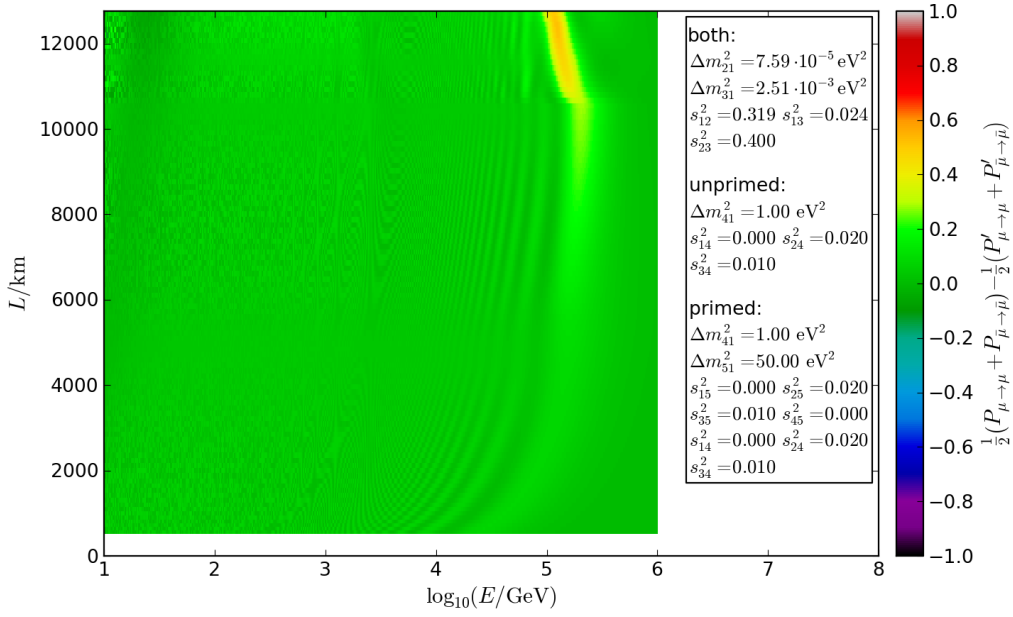


Figure 4.19: Difference $\frac{1}{2} (P_{\mu \rightarrow \mu} + P_{\bar{\mu} \rightarrow \bar{\mu}}) - \frac{1}{2} (P'_{\mu \rightarrow \mu} + P'_{\bar{\mu} \rightarrow \bar{\mu}})$ between the probabilities, averaged over muon neutrinos and antineutrinos, for a particle generated in the atmosphere to reach the detector in the same state in which it was generated, between the 3+1 model and the 3+2 model with $|\Delta m_{51}^2| \gg 1 \text{ eV}^2$. L is the path length through the Earth (s. fig. 2.2), E is the neutrino energy.

$$|\Delta m_{51}^2| \gg |\Delta m_{41}^2|$$

The larger the ratio $\Delta m_{51}^2 \div \Delta m_{41}^2$ becomes, the less the resonances due to the sterile states influence each other. It can be seen in fig. 4.19 that already for $\Delta m_{51}^2 = 50 \text{ eV}^2$ no changes of the shape in the TeV range due to $s1$ can be recognized. Still, due to the non-resonant oscillations, $\frac{1}{2} (P_{\mu \rightarrow \mu} + P_{\bar{\mu} \rightarrow \bar{\mu}})$ is slightly smaller at energies below the first minimum than if only $s1$ exists.

4.3.2 $(\Delta m_{41}^2 < 0 \wedge \Delta m_{51}^2 > 0)$ or $(\Delta m_{41}^2 > 0 \wedge \Delta m_{51}^2 < 0)$

If their signs are unequal, the ratio of the mass-squared differences is a relevant parameter, too. It can be seen again that the shape stretches linearly on the logarithmic axis if $\Delta m_{51}^2 \div \Delta m_{41}^2 = c$ is constant (s. fig. 4.20, cf. fig. 4.17). Signatures in the TeV range due to a state $s1$ with $|\Delta m_{41}^2| \approx 1 \text{ eV}^2$ are not affected by a state $s2$ with $|\Delta m_{51}^2| \gg 1 \text{ eV}^2$. This can be seen by the fact that this conclusion was found for equal signs of Δm_{51}^2 , Δm_{41}^2 , and the resonances are always less dependent in case of unequal signs.

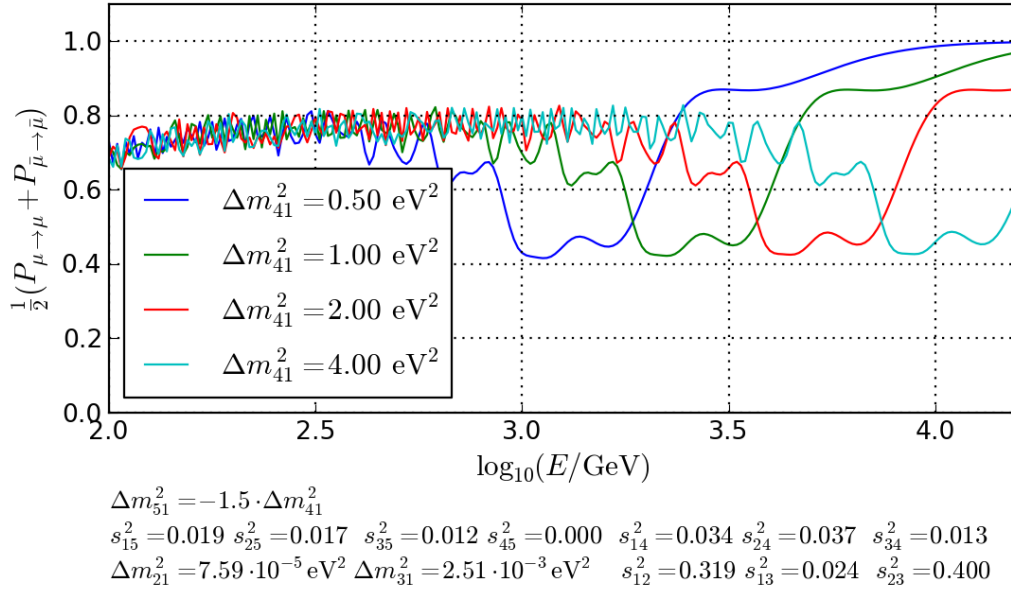


Figure 4.20: Probability $\frac{1}{2}(P_{\mu \rightarrow \mu} + P_{\bar{\mu} \rightarrow \bar{\mu}})$, averaged over muon neutrinos and antineutrinos, for a vertically incoming particle generated in the atmosphere to reach the detector in the same state in which it was generated, for various Δm_{41}^2 with $\Delta m_{41}^2 \div \Delta m_{51}^2 = c = -1.5$. E is the neutrino energy.

4.4 Impact of the angle distribution

In this section it will be examined in which way the oscillation effects due to the mixing angles of a sterile state depend on whether the sterile state associated with them is the one with the greater absolute value of its mass-squared difference.

The angles of the two sterile neutrinos are by construction not of equivalent meaning, because the pseudo rotation matrices in the parametrization of the PMNS mixing matrix ((2.6)) in general do not commute. Association of the observed effect with mixing angles must be done with this in mind.

4.4.1 $\Delta m_{41}^2, \Delta m_{51}^2 > 0$ or $\Delta m_{41}^2, \Delta m_{51}^2 < 0$

For examination it is advisable to chose the mixing angles θ_{35}, θ_{34} symmetrically. Fig. 4.21 shows an example, where two minima of the probability $P_{\bar{\mu} \rightarrow \bar{\tau}}$ occur. The one at lower energies is clearly more distinct. It comprises a larger area and contains greater transition probabilities. Furthermore this minimum looks more like the one that arises in the 3+1 model for the same mixing angle (s. fig. 3.14, cf. fig. 4.21).

Suchlike observation can be done for the oscillation between muon and sterile antineutrinos, too. For reasons of demonstration, the example with $\sin^2(\theta_{25}) = \sin^2(\theta_{24}) = 0.03$ is taken up again. The plots 4.22 and 4.23 show the corresponding probabilities $P_{\bar{\mu} \rightarrow \bar{s}1}$ and $P_{\bar{\mu} \rightarrow \bar{s}2}$, respectively. In fig. 4.22, greater values are reached.

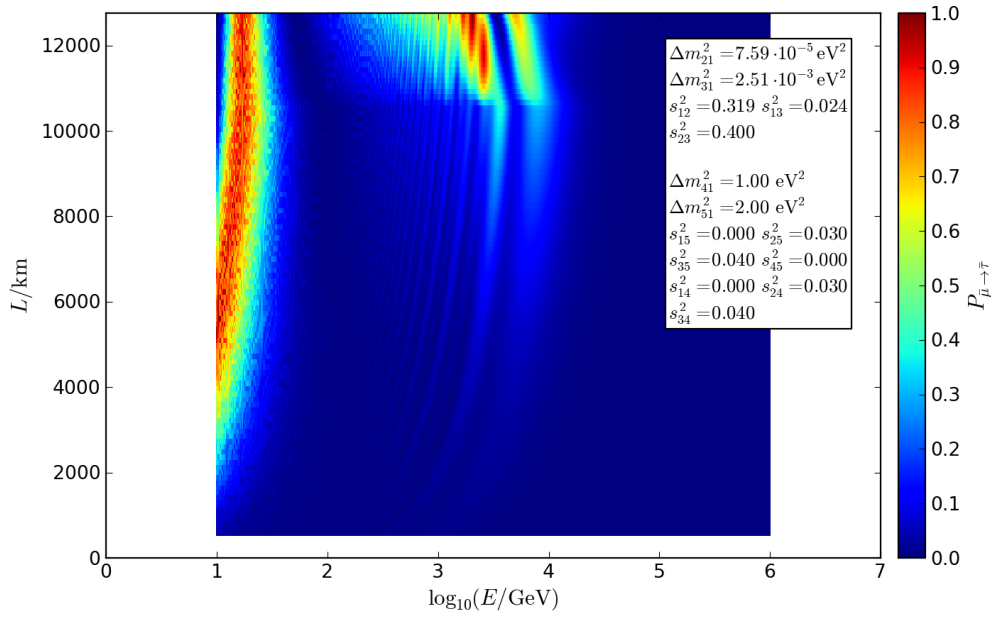


Figure 4.21: Probability $P_{\mu \rightarrow \tau}$ for a muon antineutrino generated in the atmosphere to reach the detector as a tau antineutrino. L is the path length through the Earth (s. fig. 2.2), E is the neutrino energy.

The differences are less distinct in the discussed example, because the oscillation between muon and tau antineutrinos is dominant (s. fig. B.18, fig. B.19, cf. fig. 3.16).

So the parameters of the neutrino with smaller absolute value of its mass-squared difference $\overline{s1}$ are of bigger impact. This holds for the alternative parametrization with $|\Delta m_{41}^2| > |\Delta m_{51}^2|$ and identical mixing angles (s. fig. B.20, cf. fig. 4.21). The corresponding resonance emerges for lower energies and hence – figuratively spoken – it deprives the neutrinos from the resonance at higher energies. The smaller the mass-squared difference among the sterile states, the more distinct this effect is (cf. fig. 4.21, fig. B.21). Therefore, general statements, which refer only to the mixing angles, are not possible. Instead it must be taken into account which values of Δm_{41}^2 and Δm_{51}^2 are associated with the corresponding states $\overline{s1}$, $\overline{s2}$.

The signature due to a mixing angle depends also on the values of the other mixing angles, as we can take from the different signatures of $s2$ in fig. 4.21 and fig. 4.24. There are differences to the 3+1 model even for $\sin^2(\theta_{34}) = 0 \vee \sin^2(\theta_{35}) = 0$. Indeed the shape of the signature is similar, but the maximum value is smaller (s. fig. 4.25, cf. fig. 3.14; s. fig. 4.26). The muon antineutrinos in the example from fig. 4.25 are not only able to transform into the state $\overline{s2}$, but they can also transform into $\overline{s1}$. Because transition into tau antineutrinos is only possible from the state $\overline{s2}$, $P_{\mu \rightarrow \tau}$ becomes smaller.

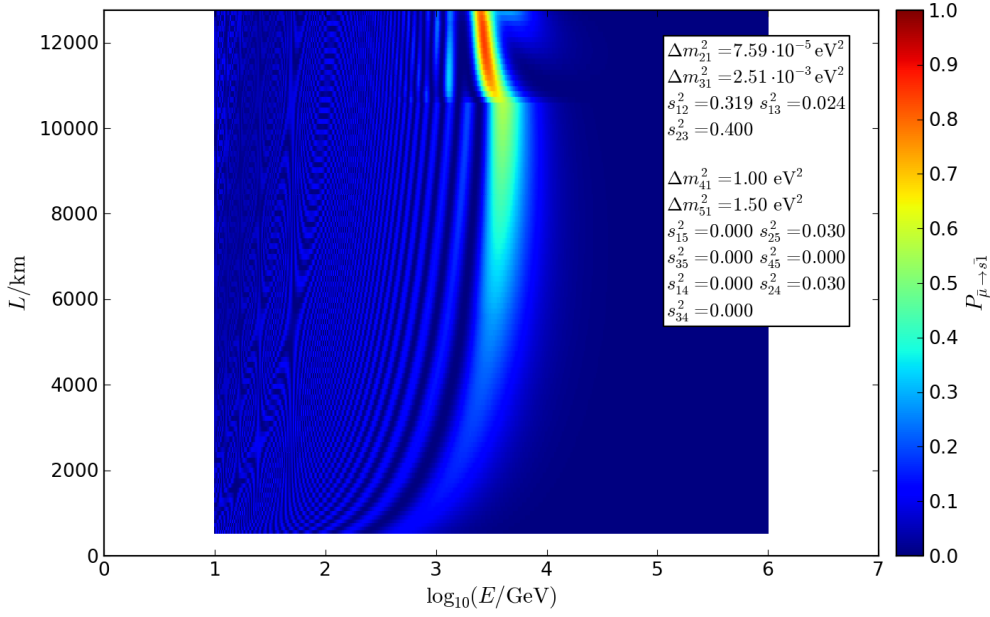


Figure 4.22: Probability $P_{\bar{\mu} \rightarrow s1}$ for a muon antineutrino generated in the atmosphere to reach the detector in state $s1$. L is the path length through the Earth (s. fig. 2.2), E is the neutrino energy.

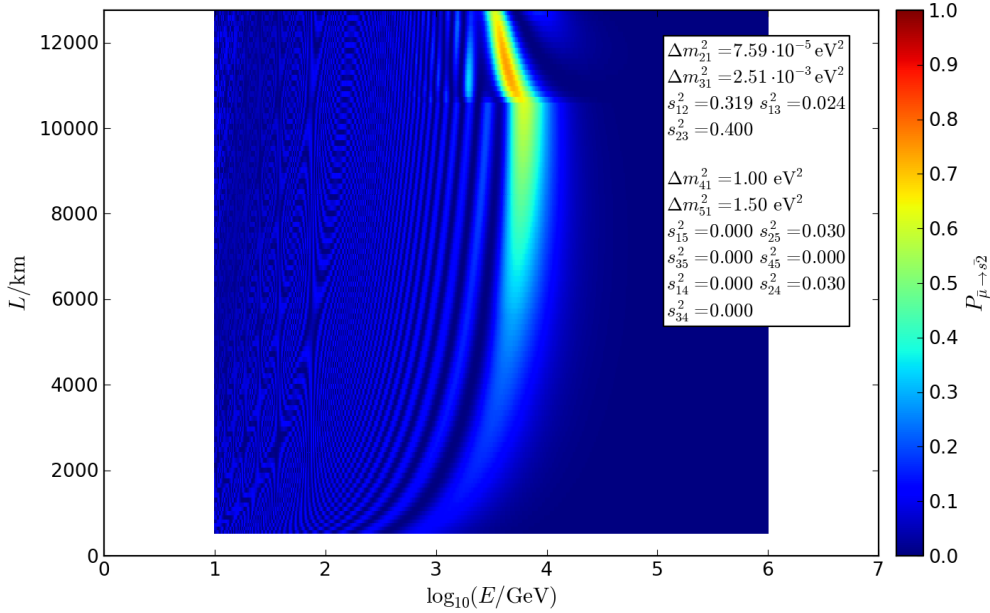


Figure 4.23: Probability $P_{\bar{\mu} \rightarrow s2}$ for a muon antineutrino generated in the atmosphere to reach the detector in state $s2$. L is the path length through the Earth (s. fig. 2.2), E is the neutrino energy.

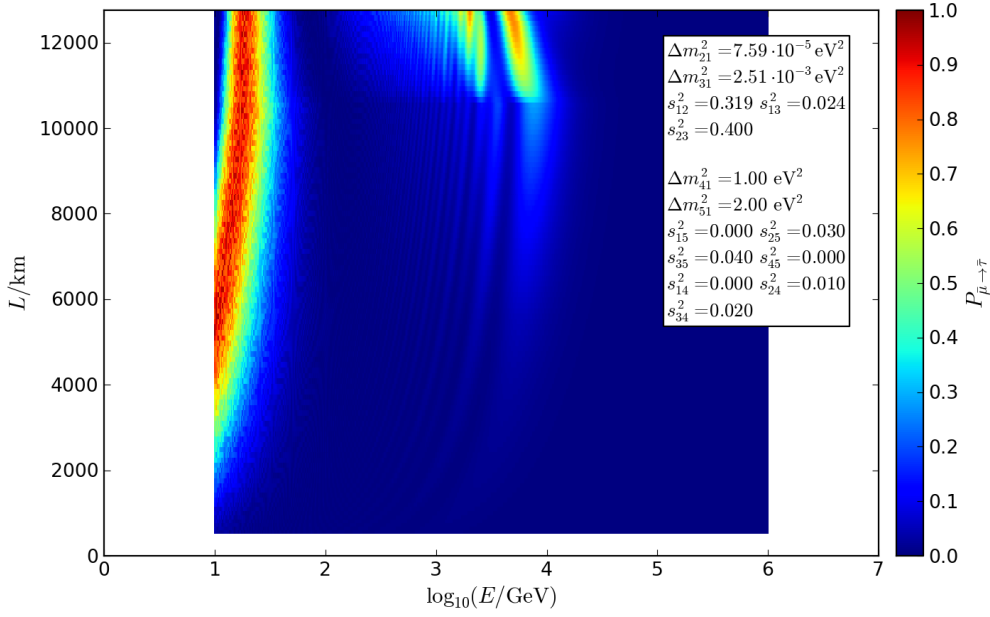


Figure 4.24: Probability $P_{\bar{\mu} \rightarrow \bar{\tau}}$ for a muon antineutrino generated in the atmosphere to reach the detector as a tau antineutrino. L is the path length through the Earth (s. fig. 2.2), E is the neutrino energy.

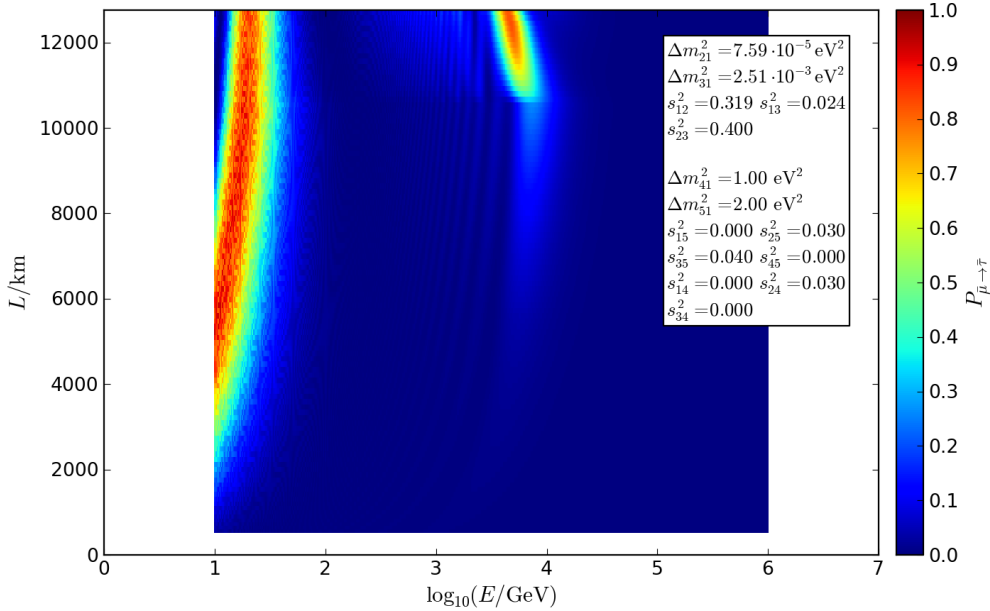
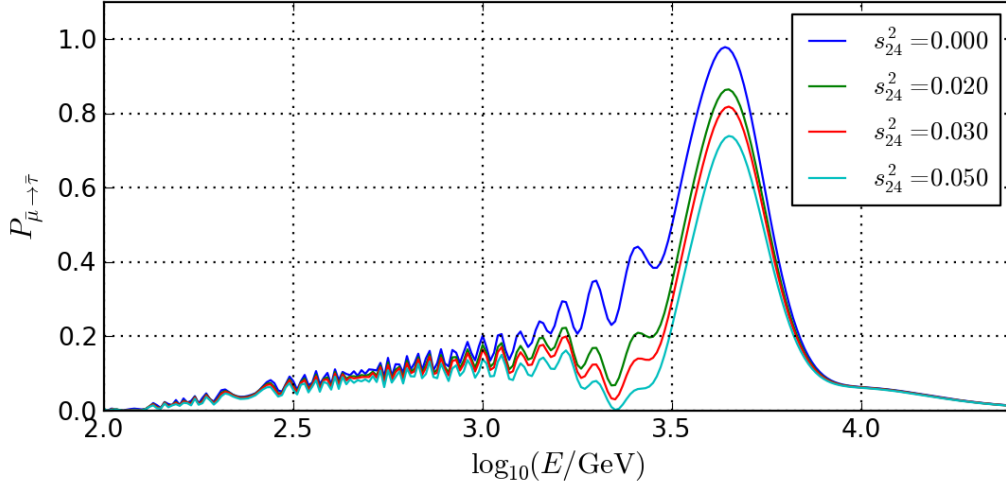


Figure 4.25: Probability $P_{\bar{\mu} \rightarrow \bar{\tau}}$ for a muon antineutrino generated in the atmosphere to reach the detector as a tau antineutrino. L is the path length through the Earth (s. fig. 2.2), E is the neutrino energy.



$$\begin{aligned} \Delta m_{41}^2 &= 1.00 \text{ eV}^2 & \Delta m_{51}^2 &= 2.00 \text{ eV}^2 & s_{25}^2 &= 0.030 & s_{35}^2 &= 0.040 & s_{14}^2 &= s_{15}^2 &= s_{34}^2 &= 0 \\ \Delta m_{21}^2 &= 7.59 \cdot 10^{-5} \text{ eV}^2 & \Delta m_{31}^2 &= 2.51 \cdot 10^{-3} \text{ eV}^2 & s_{12}^2 &= 0.319 & s_{13}^2 &= 0.024 & s_{23}^2 &= 0.400 \end{aligned}$$

Figure 4.26: Probability $P_{\bar{\mu} \rightarrow \bar{\tau}}$ for a vertically incoming muon antineutrino generated in the atmosphere to reach the detector as a tau antineutrino, for various $\sin^2(\theta_{24})$. E is the neutrino energy.

The greater values a mixing angle takes, the more it forms the signature due to the other mixing angles (s. fig. 4.26). Caused by corrections due to the relative sign to Δm_{32}^2 , the transition probabilities of both mass hierarchies differ a little bit from each other (s. fig. B.22, fig. B.23).

4.4.2 $(\Delta m_{41}^2 < 0 \wedge \Delta m_{51}^2 > 0)$ or $(\Delta m_{41}^2 > 0 \wedge \Delta m_{51}^2 < 0)$

The oscillations are more independent than in case of equal signs, because they occur in separated channels. Hence both resonances look more like the resonance in the 3+1 model (s. fig. 4.8, fig. 4.27, cf. fig. 3.14).

They are about equally prominent, with their minimum values being equal. Therefore, the signature due to a mixing angle here depends less on which mass state it is associated with. There are slight differences due to the relative signs of Δm_{41}^2 or Δm_{51}^2 to Δm_{32}^2 , respectively (s. fig. B.24).

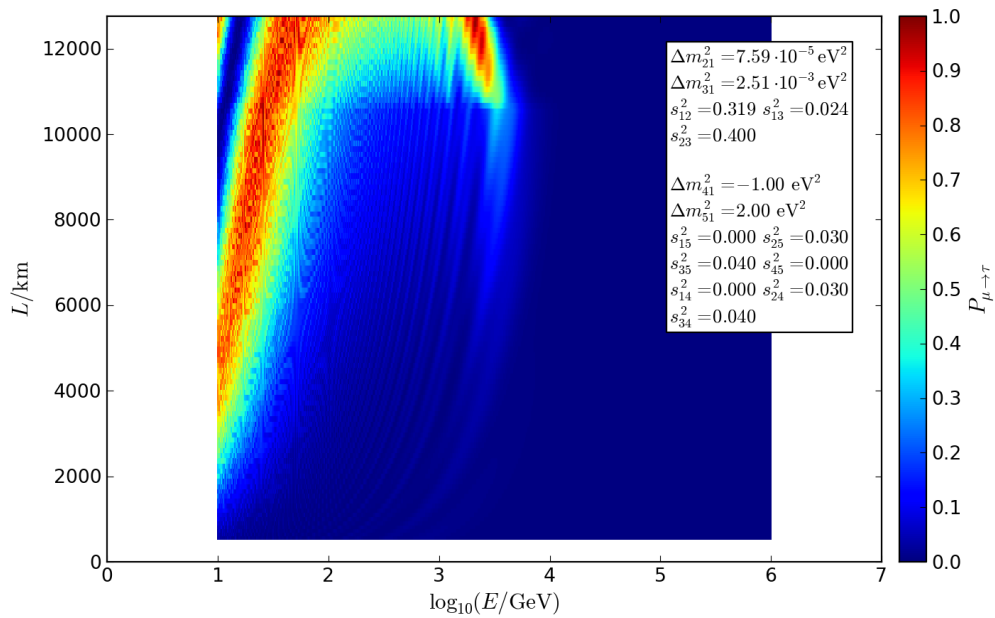


Figure 4.27: Probability $P_{\mu \rightarrow \tau}$ for a muon neutrino generated in the atmosphere to reach the detector as a tau neutrino. L is the path length through the Earth (s. fig. 2.2), E is the neutrino energy.

Chapter 5

Conclusion

5.1 3+1 model

In chapter 3 oscillation effects due to the addition of a single sterile state to the known states were studied. The angles θ_{24} , θ_{34} , and θ_{14} were step-by-step assumed to be non-vanishing, in order to examine the changes caused by them. Finally, there was a look at CP-violating phases. The effect caused by the existence of a single additional sterile state are summarized below.

For $\theta_{24} \neq 0$, $\theta_{34} = \theta_{14} = 0$, and $\Delta m_{41}^2 > 0$, a resonance in the TeV range between muon and sterile neutrinos occurs in the antiparticle channel, for $\Delta m_{41}^2 < 0$ almost the same resonance occurs in the particle channel. The situation is describable as a two-flavor oscillation. For other values of Δm_{41}^2 the signature stretches on the energy axis. There is a linear dependence of the transition probability on $|\Delta m_{41}^2|$, hence the shape on the logarithmic axis is kept. θ_{24} determines the shape of the signature. The greater values $\sin^2(\theta_{24})$ takes, the smaller the path length of the minimum of $P_{\bar{\mu} \rightarrow \bar{\mu}}$ or $P_{\mu \rightarrow \mu}$ is, respectively. Furthermore, the minimum is bigger and changes its shape non-linearly.

If θ_{34} assumes non-zero values, too, in addition a resonance of the probability $P_{\bar{\mu} \rightarrow \bar{\tau}}$ ($\Delta m_{41}^2 > 0$) or $P_{\mu \rightarrow \tau}$ ($\Delta m_{41}^2 < 0$) appears in the TeV range. It is not a direct result of oscillations between muon and tau neutrinos, but can be understood as a sequence of two two-flavor oscillations between muon and sterile neutrinos and then between sterile and tau neutrinos.

Furthermore, in this case the matter parameters $\theta_{23,\text{Mat}}$ and $\Delta m_{32,\text{Mat}}^2$ distinctly differ from the corresponding vacuum variables. Due to this there is a widening of the conventional oscillations in the particle channel ($\Delta m_{32}^2 > 0$) or in the antiparticle channel ($\Delta m_{32}^2 < 0$).

Because Δm_{21}^2 is much smaller than the other mass-squared differences, the angle θ_{14} is less important compared to the other mixing angles.

CP-violating phases do not affect the structures of the transition probabilities in the TeV range. This is in so far understandable as they can be understood as two-flavor oscillations. The matter parameters $\theta_{23,\text{Mat}}$ and $\Delta m_{32,\text{Mat}}^2$ depend on the phases δ_{24} and δ_{34} . Both

phases cause similar changes. Differences occur only for $\sin^2(\theta_{14}) \neq 0$. In this case, δ_{13} also leads to changes.

In order to describe the structures in the TeV range completely, it is enough to focus on a specific Δm_{41}^2 , because there is a linear dependence of the transition probabilities on Δm_{41}^2 .

5.2 3+2 model

The general impact of the mixing angles in the 3+2 model can be deduced from the 3+1 model.

For $\Delta m_{41}^2, \Delta m_{51}^2 > 0$ and $\sin^2(\theta_{24}), \sin^2(\theta_{25}) \neq 0$, resonant oscillations between sterile and muon neutrinos in the antiparticle channel is possible, and for $\Delta m_{41}^2, \Delta m_{51}^2 < 0$ in the particle channel. Provided that in addition $\sin^2(\theta_{34}), \sin^2(\theta_{35}) \neq 0$ applies, corresponding resonances between muon and tau neutrinos occur. Furthermore, in this case changes of the conventional oscillations as already seen in the 3+1 model appear.

The relative sign of Δm_{41}^2 and Δm_{51}^2 is an important parameter, because in case of unequal signs, the oscillations take place in separated channels, hence in sum more distinct effects are possible. If they occur in the same channel, they influence each other.

Furthermore, the ratio $\Delta m_{41}^2 \div \Delta m_{51}^2$ is an interesting parameter. For equal relative mass-squared differences and equal mixing angles, the signatures in the TeV range stretch on the energy scale with linear dependence on $\Delta m_{41}^2, \Delta m_{51}^2$.

For every combination of mixing angles in the 3+1 model, a counterpart in the 3+2 model with mass-squared differences of the sterile states very close to each other can be found.

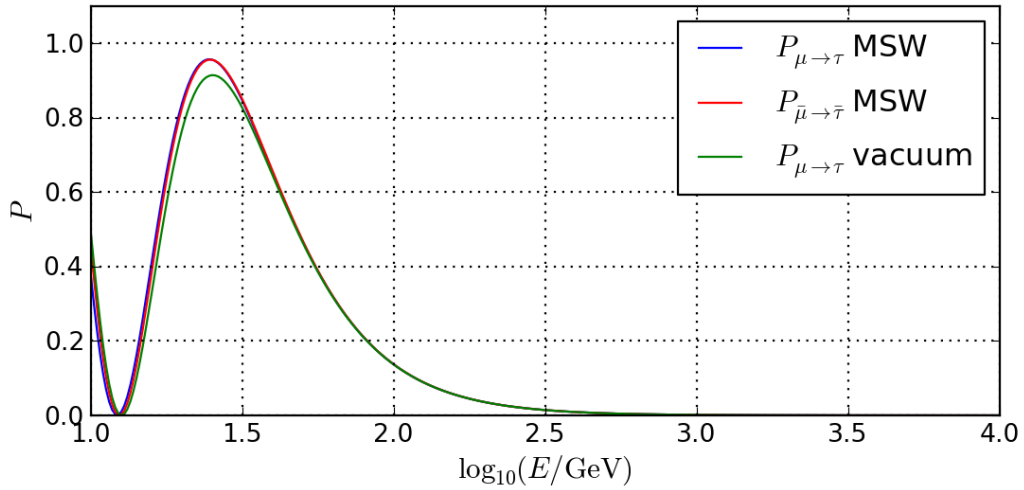
The signature due to a mixing angle depends on which sterile neutrino type is associated with it, especially if the signs of Δm_{41}^2 and Δm_{51}^2 are equal. Mixing angles referring to the sterile state with the smaller absolute value of its mass-squared difference cause more distinct effects. The mixing angles of each sterile state influence the probabilities due to the mixing angles of the other one. Therefore, further reductions of the parameter space are not possible.

Sterile states s_2 with $|\Delta m_{51}^2| \gg 1 \text{ eV}^2$ do not modify signatures in the TeV range due to sterile states s_1 with $|\Delta m_{41}^2| \approx 1 \text{ eV}^2$.

Appendix A

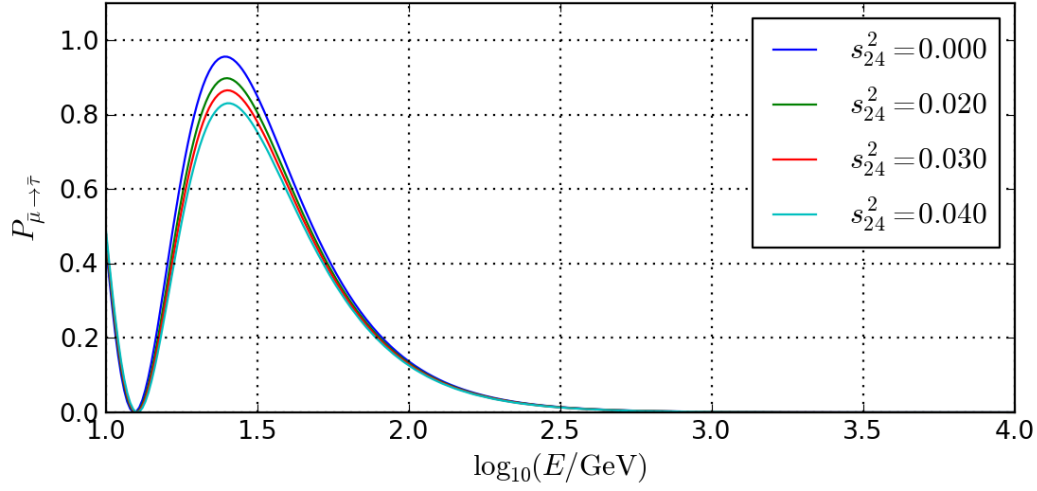
3+1 model

A.1 $\sin^2(\theta_{14}) = \sin^2(\theta_{24}) = \sin^2(\theta_{34}) = 0$



$$\begin{aligned} \Delta m_{41}^2 &= 1.00 \text{ eV}^2 & s_{14}^2 &= 0.000 & s_{24}^2 &= 0.000 & s_{34}^2 &= 0.000 \\ \Delta m_{21}^2 &= 7.59 \cdot 10^{-5} \text{ eV}^2 & \Delta m_{31}^2 &= 2.51 \cdot 10^{-3} \text{ eV}^2 & s_{12}^2 &= 0.319 & s_{13}^2 &= 0.024 & s_{23}^2 &= 0.400 \end{aligned}$$

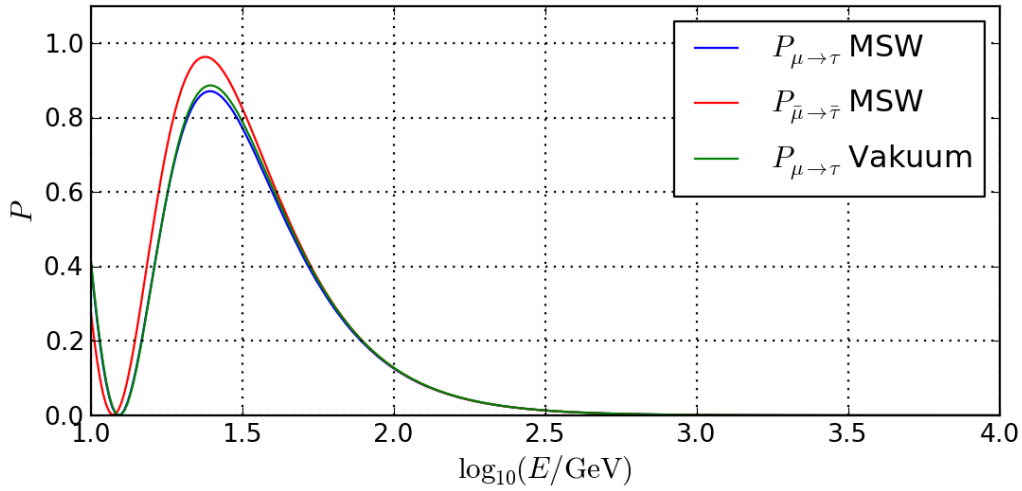
Figure A.1: Comparison between the probabilities $P_{\mu \rightarrow \tau}$ and $P_{\bar{\mu} \rightarrow \bar{\tau}}$ for a vertically incoming muon neutrino or antineutrino generated in the atmosphere to reach the detector as a tau neutrino or antineutrino. E is the neutrino energy.

A.2 $\sin^2(\theta_{24}) \neq 0$, where $\sin^2(\theta_{34}) = \sin^2(\theta_{14}) = 0$


$$\Delta m_{41}^2 = 1.00 \text{ eV}^2 \quad s_{14}^2 = 0.000 \quad s_{34}^2 = 0.000$$

$$\Delta m_{21}^2 = 7.59 \cdot 10^{-5} \text{ eV}^2 \quad \Delta m_{31}^2 = 2.51 \cdot 10^{-3} \text{ eV}^2 \quad s_{12}^2 = 0.319 \quad s_{13}^2 = 0.024 \quad s_{23}^2 = 0.400$$

Figure A.2: Probability $P_{\bar{\mu} \rightarrow \bar{\tau}}$ for a vertically incoming muon antineutrino generated in the atmosphere to reach the detector as a tau antineutrino, for various $\sin^2(\theta_{24})$. E is the neutrino energy.



$$\Delta m_{41}^2 = 1.00 \text{ eV}^2 \quad s_{14}^2 = 0.000 \quad s_{24}^2 = 0.030 \quad s_{34}^2 = 0.000$$

$$\Delta m_{21}^2 = 7.59 \cdot 10^{-5} \text{ eV}^2 \quad \Delta m_{31}^2 = -2.35 \cdot 10^{-3} \text{ eV}^2 \quad s_{12}^2 = 0.319 \quad s_{13}^2 = 0.024 \quad s_{23}^2 = 0.400$$

Figure A.3: Comparison between the probabilities $P_{\mu \rightarrow \tau}$ and $P_{\bar{\mu} \rightarrow \bar{\tau}}$ for a vertically incoming muon neutrino or antineutrino generated in the atmosphere to reach the detector as a tau neutrino or antineutrino. E is the neutrino energy.

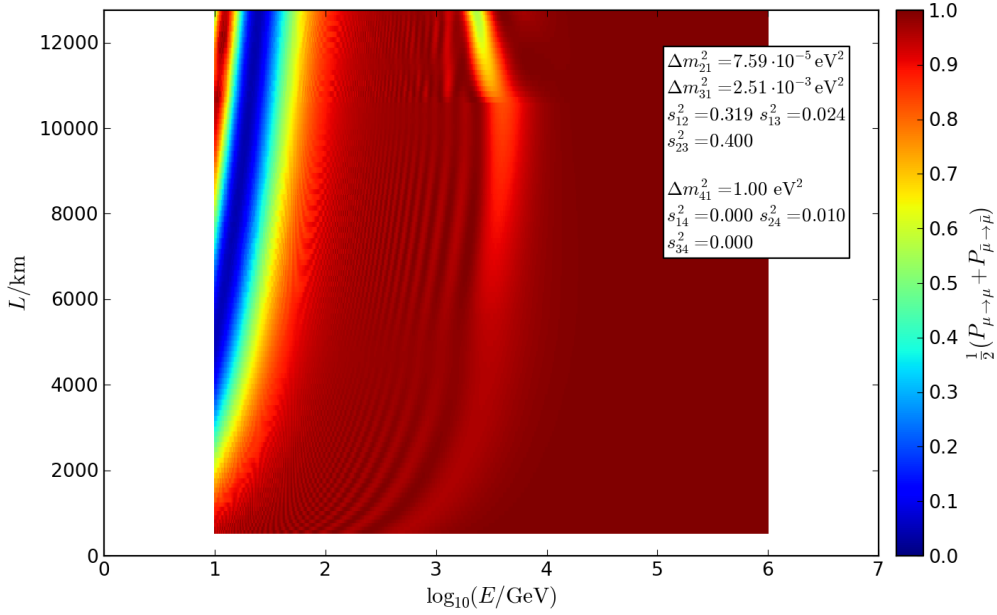


Figure A.4: Probability $\frac{1}{2} (P_{\mu \rightarrow \mu} + P_{\bar{\mu} \rightarrow \bar{\mu}})$, averaged over muon neutrinos and antineutrinos, for a particle generated in the atmosphere to reach the detector in the same state in which it was generated. L is the path length through the Earth (s. fig. 2.2), E is the neutrino energy.

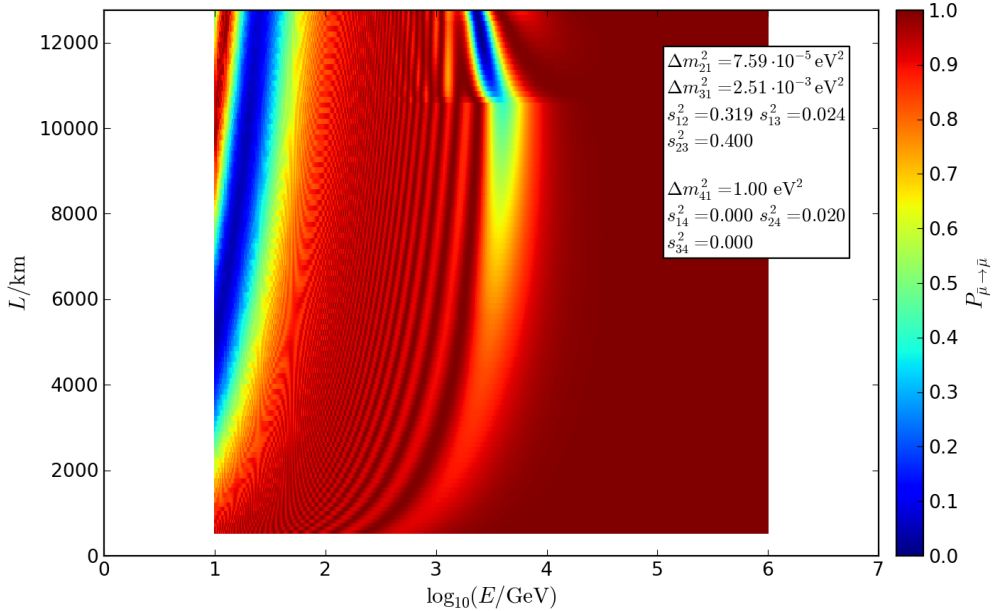


Figure A.5: Probability $P_{\bar{\mu} \rightarrow \bar{\mu}}$ for a muon antineutrino generated in the atmosphere to reach the detector as a muon antineutrino. L is the path length through the Earth (s. fig. 2.2), E is the neutrino energy.

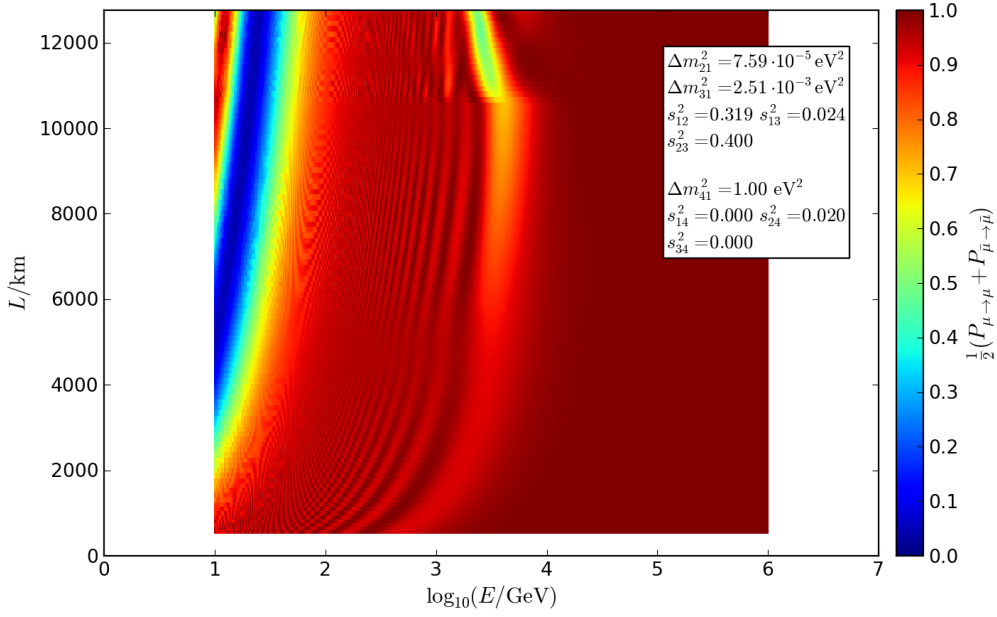


Figure A.6: Probability $\frac{1}{2} (P_{\mu \rightarrow \mu} + P_{\bar{\mu} \rightarrow \bar{\mu}})$, averaged over muon neutrinos and antineutrinos, for a particle generated in the atmosphere to reach the detector in the same state in which it was generated. L is the path length through the Earth (s. fig. 2.2), E is the neutrino energy.

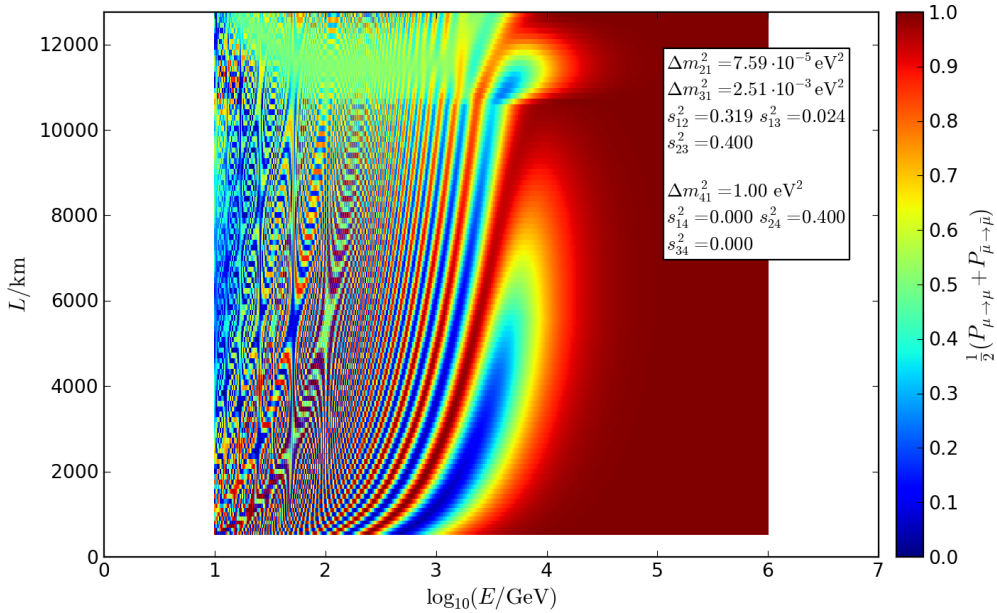


Figure A.7: Probability $\frac{1}{2} (P_{\mu \rightarrow \mu} + P_{\bar{\mu} \rightarrow \bar{\mu}})$, averaged over muon neutrinos and antineutrinos, for a particle generated in the atmosphere to reach the detector in the same state in which it was generated. L is the path length through the Earth (s. fig. 2.2), E is the neutrino energy.

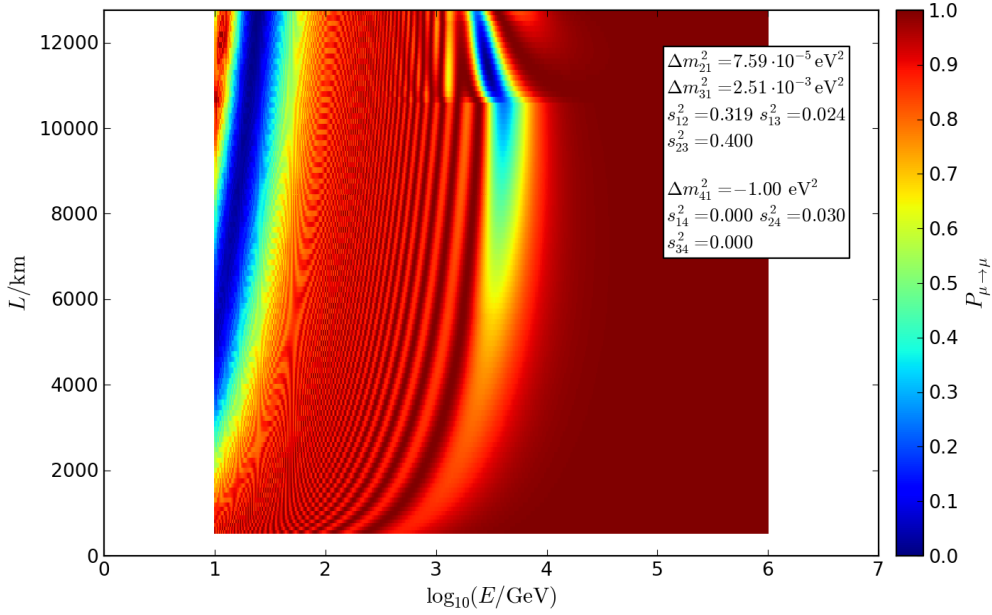


Figure A.8: Probability $P_{\mu \rightarrow \mu}$ for a muon neutrino generated in the atmosphere to reach the detector as a muon neutrino. L is the path length through the Earth (s. fig. 2.2), E is the neutrino energy.

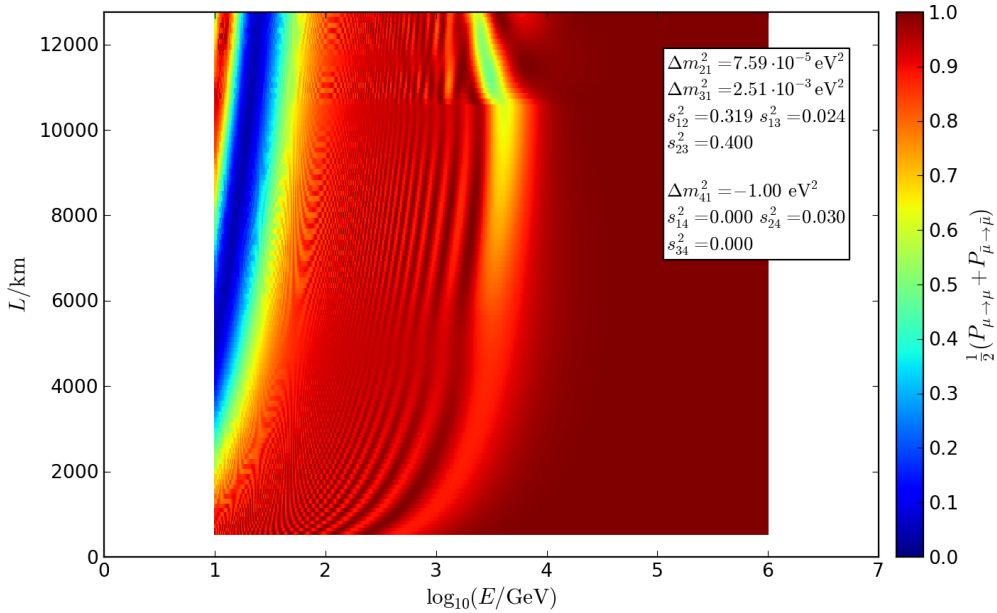


Figure A.9: Probability $\frac{1}{2}(P_{\mu \rightarrow \mu} + P_{\bar{\mu} \rightarrow \bar{\mu}})$, averaged over muon neutrinos and antineutrinos, for a particle generated in the atmosphere to reach the detector in the same state in which it was generated. L is the path length through the Earth (s. fig. 2.2), E is the neutrino energy.

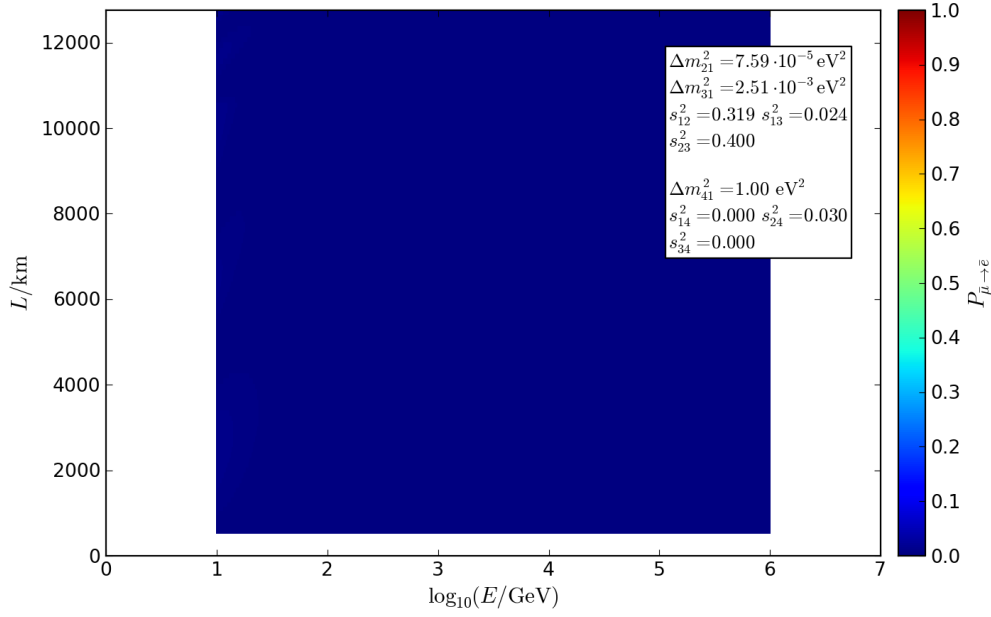


Figure A.10: Probability $P_{\bar{\mu} \rightarrow \bar{e}}$ for a muon antineutrino generated in the atmosphere to reach the detector as an electron antineutrino. L is the path length through the Earth (s. fig. 2.2), E is the neutrino energy.

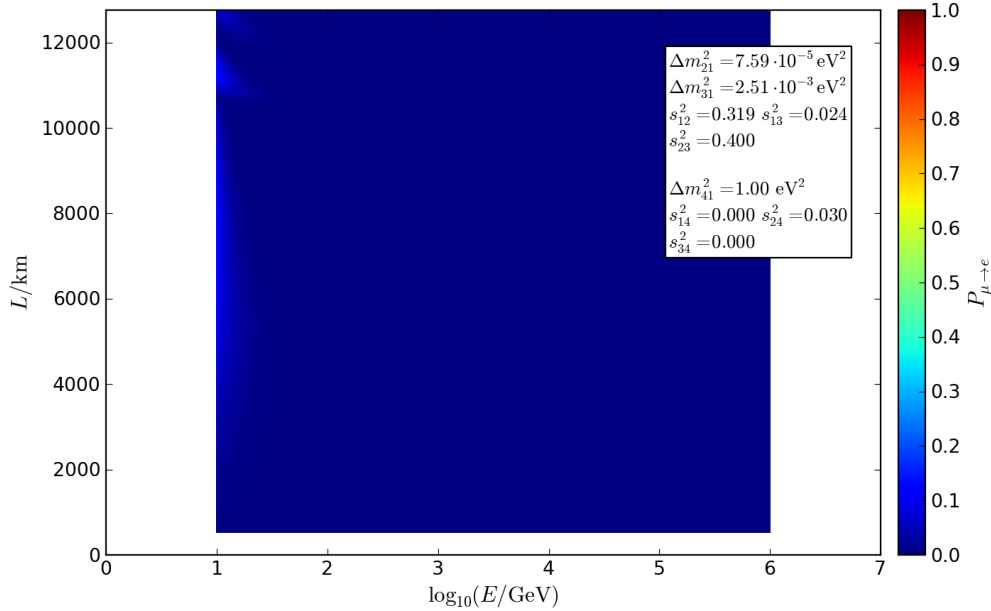


Figure A.11: Probability $P_{\mu \rightarrow e}$ for a muon neutrino generated in the atmosphere to reach the detector as an electron neutrino. L is the path length through the Earth (s. fig. 2.2), E is the neutrino energy.

A.3 $\sin^2(\theta_{34}) \neq 0$, where $\sin^2(\theta_{24}) = \sin(\theta_{14}) = 0$

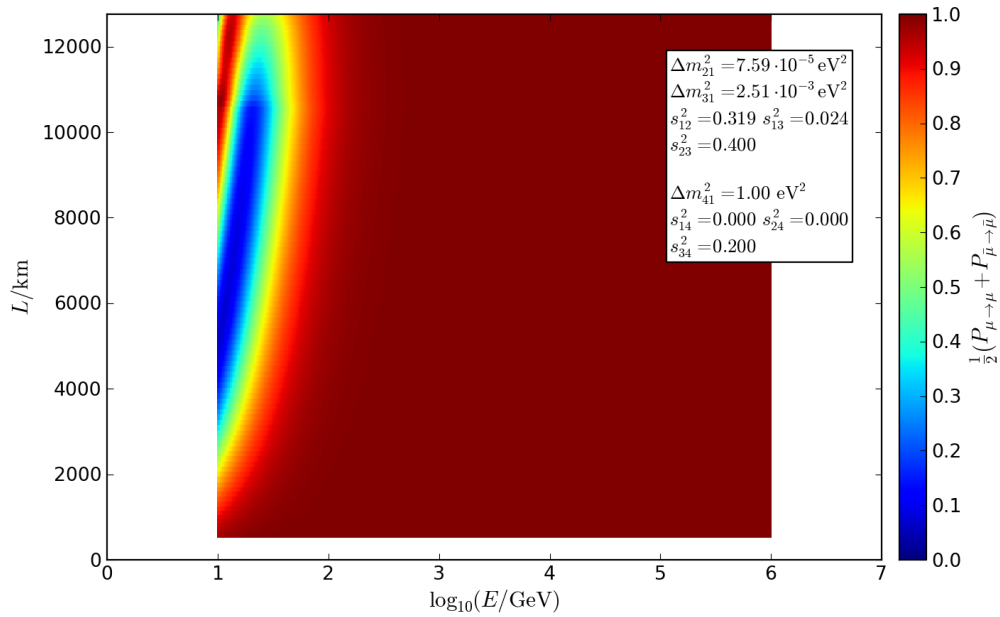
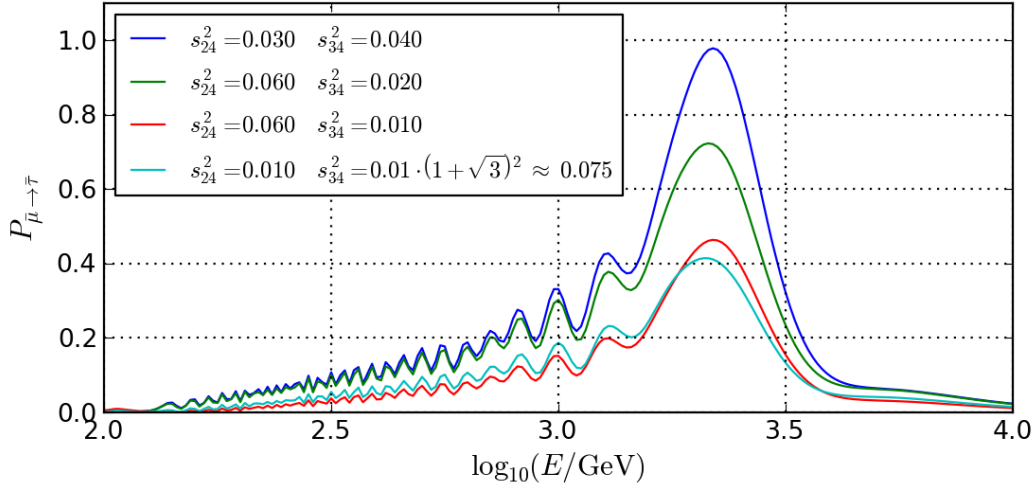


Figure A.12: Probability $\frac{1}{2}(P_{\mu \rightarrow \mu} + P_{\bar{\mu} \rightarrow \bar{\mu}})$, averaged over muon neutrinos and antineutrinos, for a particle generated in the atmosphere to reach the detector in the same state in which it was generated. L is the path length through the Earth (s. fig. 2.2), E is the neutrino energy.

A.4 $\sin^2(\theta_{24}), \sin^2(\theta_{34}) \neq 0$, where $\sin^2(\theta_{14}) = 0$


$$\begin{aligned} \Delta m_{41}^2 &= 1.00 \text{ eV}^2 & s_{14}^2 &= 0.000 \\ \Delta m_{21}^2 &= 7.59 \cdot 10^{-5} \text{ eV}^2 & \Delta m_{31}^2 &= 2.51 \cdot 10^{-3} \text{ eV}^2 & s_{12}^2 &= 0.319 & s_{13}^2 &= 0.024 & s_{23}^2 &= 0.400 \end{aligned}$$

Figure A.13: Probability $P_{\bar{\mu} \rightarrow \bar{\tau}}$ for a vertically incoming muon antineutrino generated in the atmosphere to reach the detector as a tau antineutrino. E is the neutrino energy. It is illustrated that neither $\sin^2(\theta_{24}) + \sin^2(\theta_{34})$ nor $\sin(\theta_{24}) + \sin(\theta_{34})$ or $\sin^2(\theta_{24}) \cdot \sin^2(\theta_{34})$ are decisive quantities.

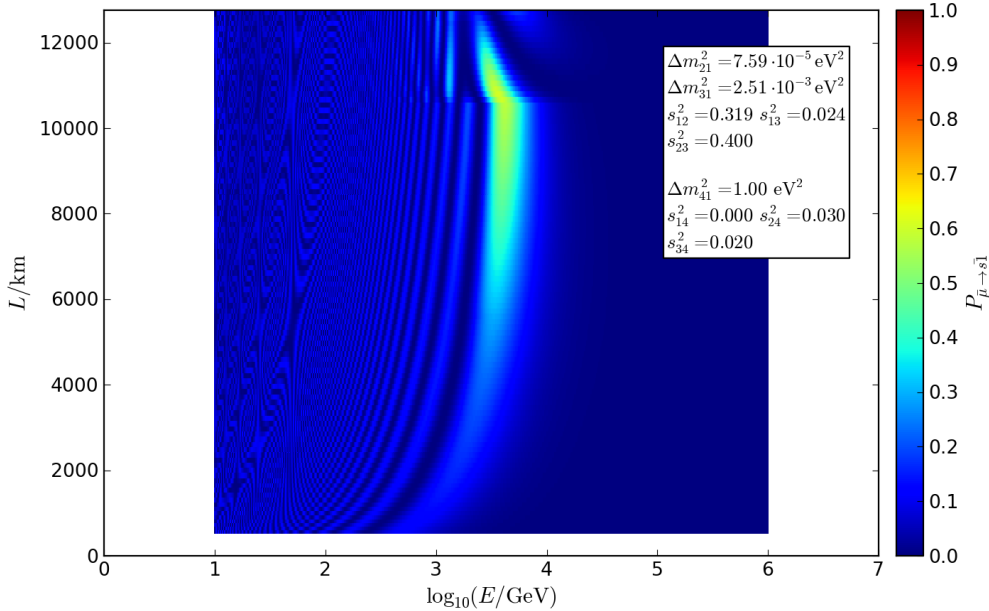


Figure A.14: Probability $P_{\bar{\mu} \rightarrow s1}$ for a muon antineutrino generated in the atmosphere to reach the detector as a sterile antineutrino. L is the path length through the Earth (s. fig. 2.2), E is the neutrino energy.

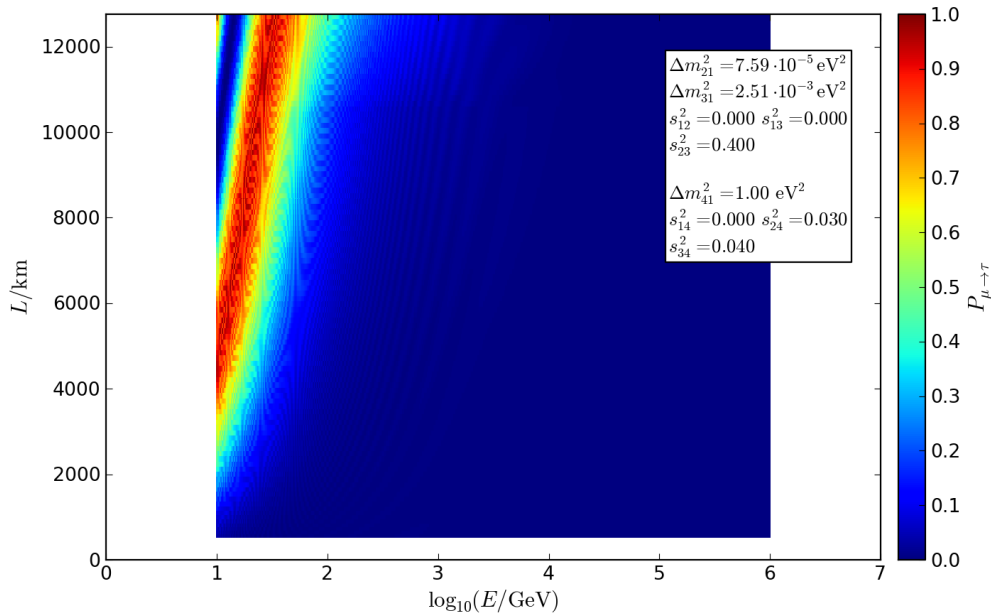


Figure A.15: Probability $P_{\mu \rightarrow \tau}$ for a muon neutrino generated in the atmosphere to reach the detector as a tau neutrino. L is the path length through the Earth (s. fig. 2.2), E is the neutrino energy.

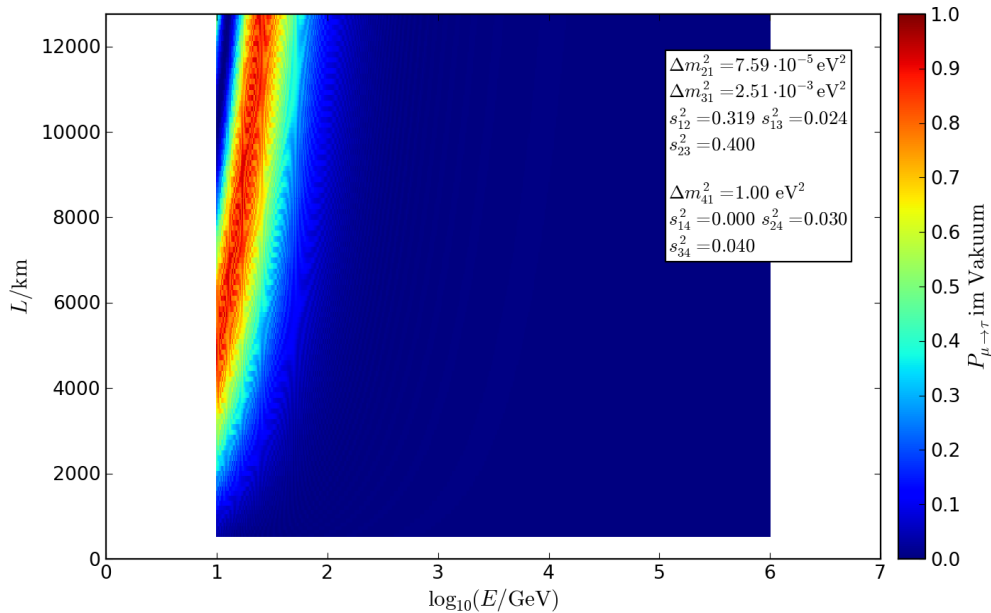


Figure A.16: Probability $P_{\mu \rightarrow \tau}$ for a muon neutrino generated in the atmosphere to reach the detector as a tau neutrino, when assuming vacuum propagation. L is the path length through the Earth (s. fig. 2.2), E is the neutrino energy.

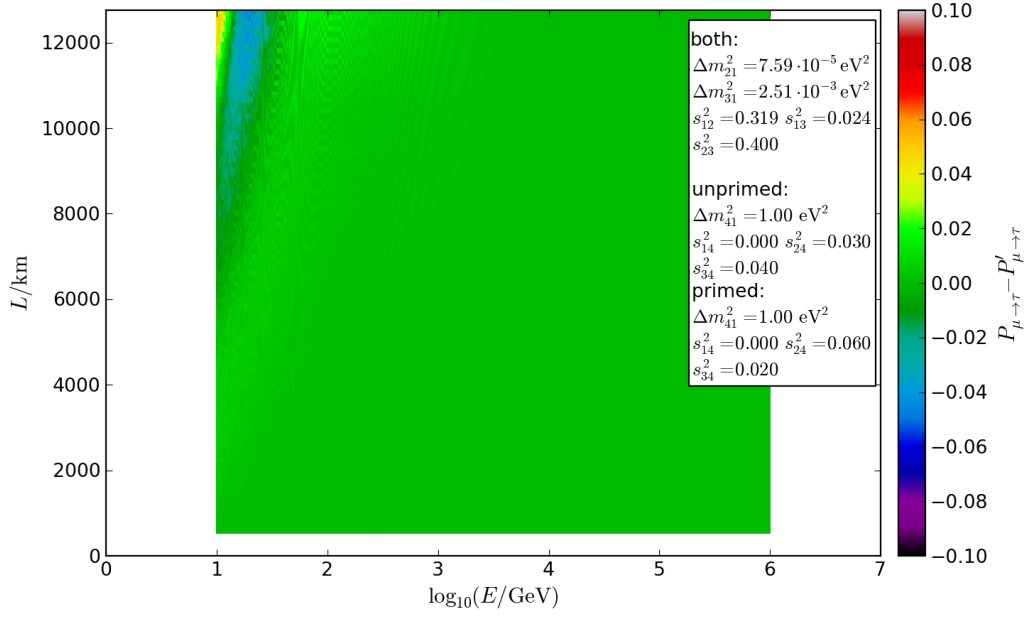


Figure A.17: Difference $\frac{1}{2}(P_{\mu \rightarrow \mu} + P_{\bar{\mu} \rightarrow \bar{\mu}}) - \frac{1}{2}(P'_{\mu \rightarrow \mu} + P'_{\bar{\mu} \rightarrow \bar{\mu}})$ between the probabilities, averaged over muon neutrinos and antineutrinos, for a particle generated in the atmosphere to reach the detector in the same state in which it was generated, between $\sin^2(\theta_{14}) = 0.00$, $\sin^2(\theta_{24}) = 0.03$, $\sin^2(\theta_{34}) = 0.04$ (unprimed) and $\sin^2(\theta_{14}) = 0.00$, $\sin^2(\theta_{24}) = 0.06$, $\sin^2(\theta_{34}) = 0.02$ (primed). L is the path length through the Earth (s. fig. 2.2), E is the neutrino energy.

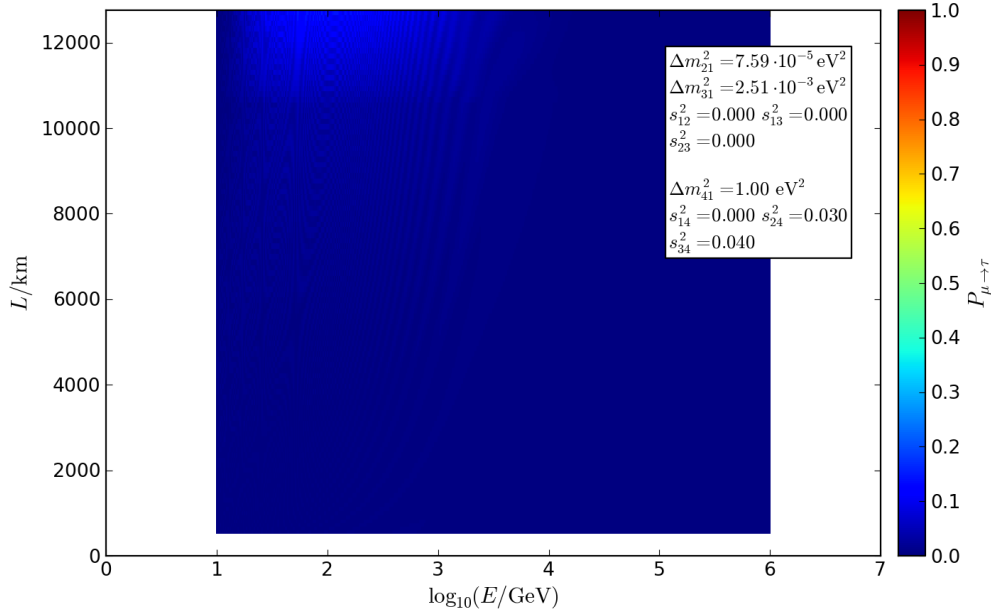


Figure A.18: Probability $P_{\mu \rightarrow \tau}$ for a muon neutrino generated in the atmosphere to reach the detector as a tau neutrino. L is the path length through the Earth (s. fig. 2.2), E is the neutrino energy.

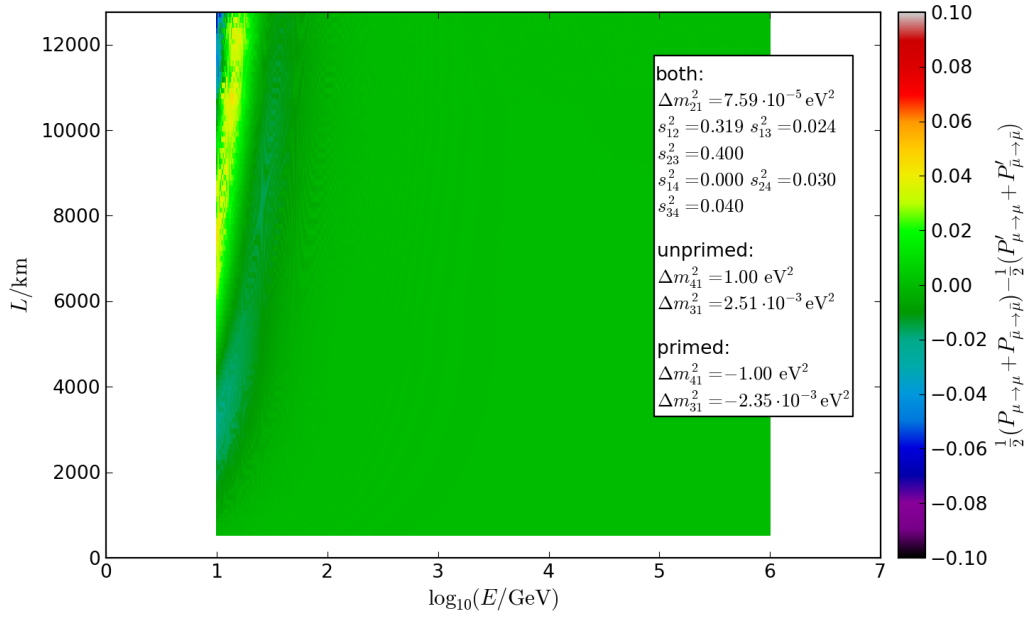


Figure A.19: Difference $\frac{1}{2} (P_{\mu \rightarrow \mu} + P_{\bar{\mu} \rightarrow \bar{\mu}}) - \frac{1}{2} (P'_{\mu \rightarrow \mu} + P'_{\bar{\mu} \rightarrow \bar{\mu}})$ between the probabilities, averaged over muon neutrinos and antineutrinos, for a particle generated in the atmosphere to reach the detector in the same state in which it was generated, between $\Delta m_{32}^2, \Delta m_{41}^2 > 0$ (unprimed) and $\Delta m_{32}^2, \Delta m_{41}^2 < 0$ (primed). L is the path length through the Earth (s. fig. 2.2), E is the neutrino energy.

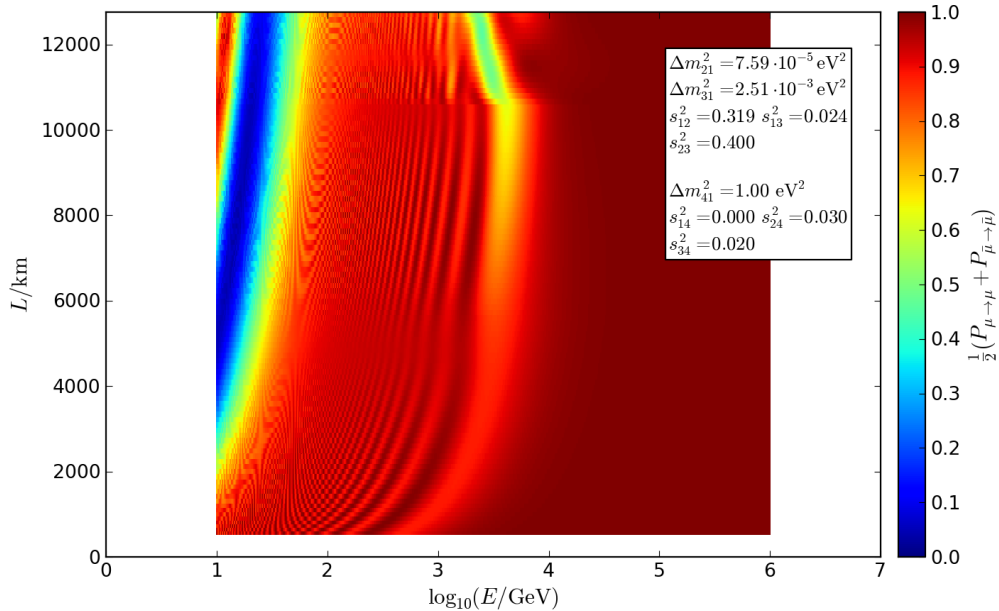


Figure A.20: Probability $\frac{1}{2} (P_{\mu \rightarrow \mu} + P_{\bar{\mu} \rightarrow \bar{\mu}})$, averaged over muon neutrinos and antineutrinos, for a particle generated in the atmosphere to reach the detector in the same state in which it was generated. L is the path length through the Earth (s. fig. 2.2), E is the neutrino energy.

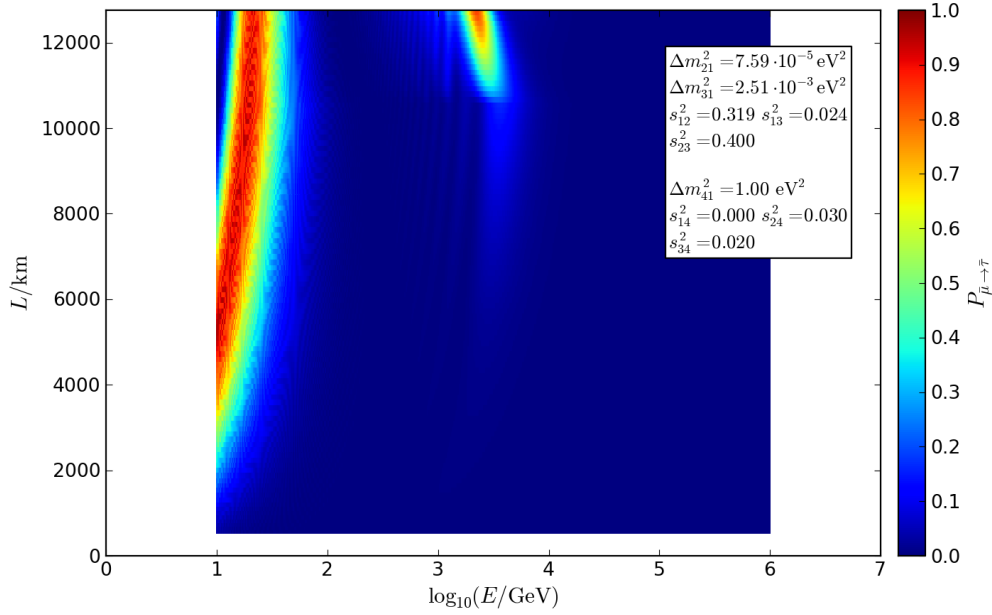


Figure A.21: Probability $P_{\bar{\mu} \rightarrow \bar{\tau}}$ for a muon antineutrino generated in the atmosphere to reach the detector as a tau antineutrino. L is the path length through the Earth (s. fig. 2.2), E is the neutrino energy.

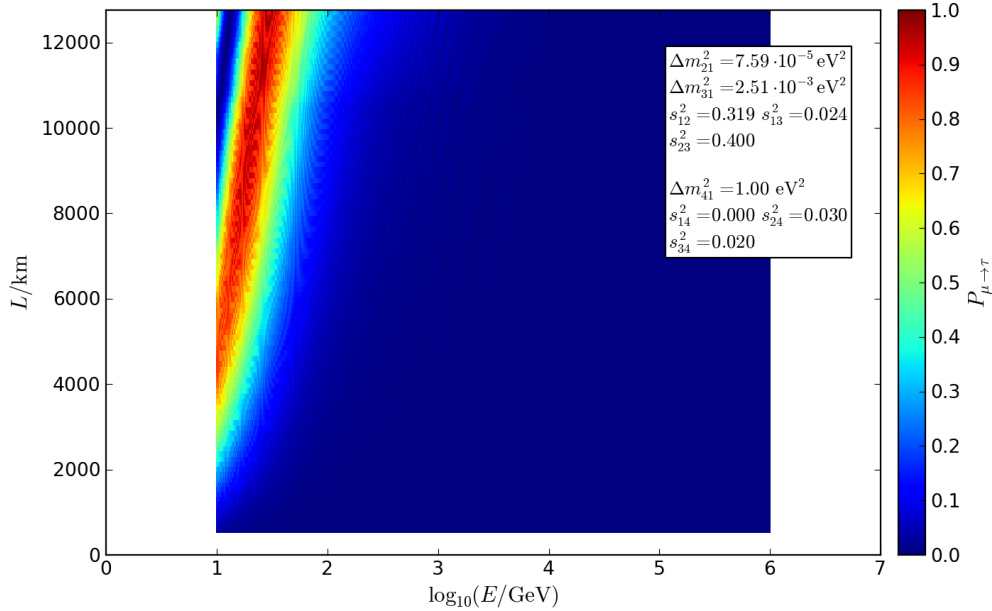


Figure A.22: Probability $P_{\mu \rightarrow \tau}$ for a muon neutrino generated in the atmosphere to reach the detector as a tau neutrino. L is the path length through the Earth (s. fig. 2.2), E is the neutrino energy.

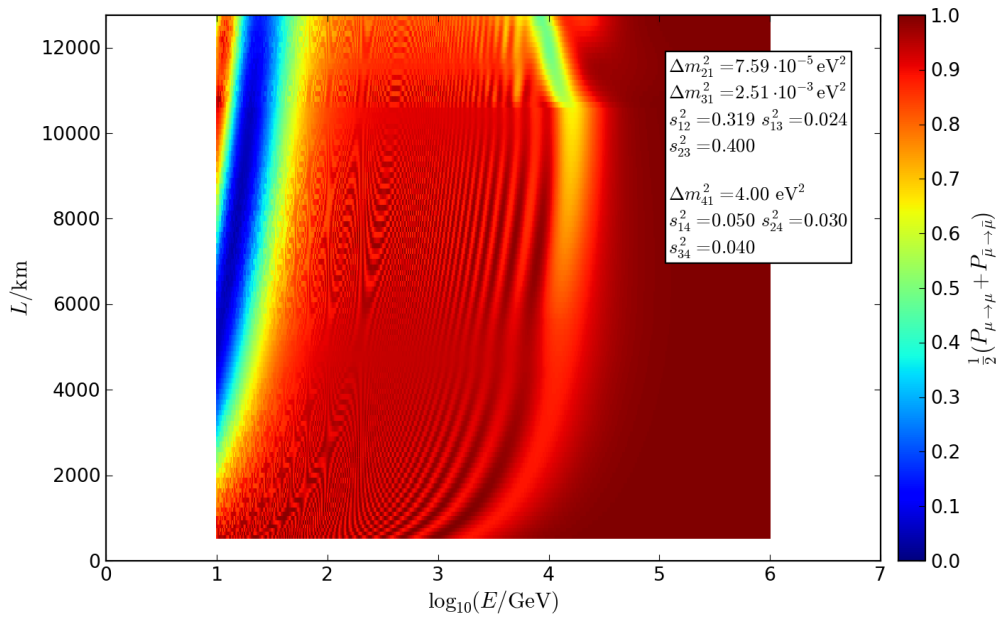


Figure A.23: Probability $\frac{1}{2}(P_{\mu \rightarrow \mu} + P_{\bar{\mu} \rightarrow \bar{\mu}})$, averaged over muon neutrinos and antineutrinos, for a particle generated in the atmosphere to reach the detector in the same state in which it was generated. L is the path length through the Earth (s. fig. 2.2), E is the neutrino energy.

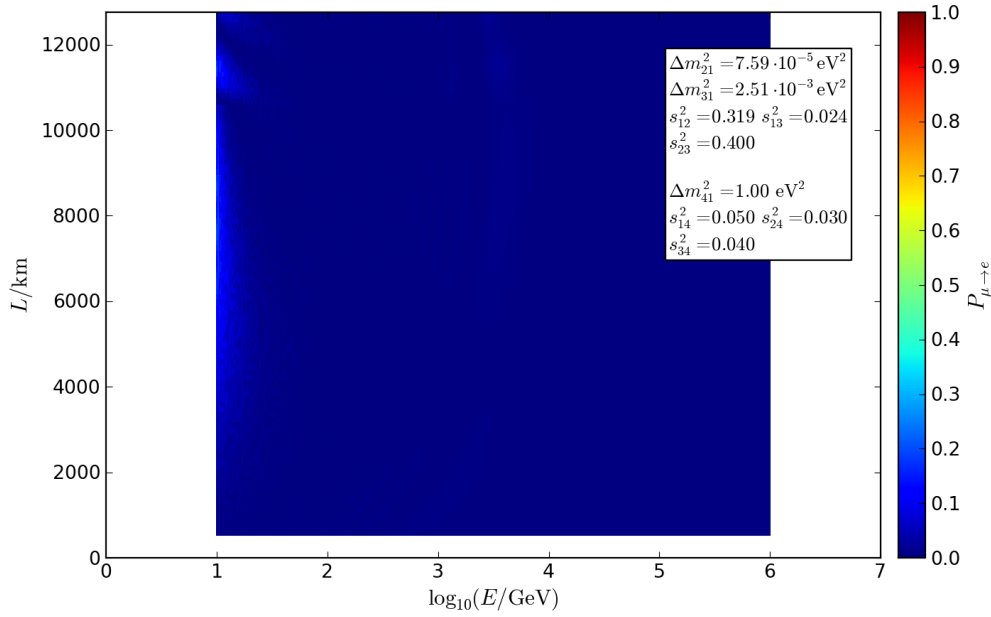
A.5 $\sin^2(\theta_{24}), \sin^2(\theta_{34}), \sin^2(\theta_{14}) \neq 0$


Figure A.24: Probability $P_{\mu \rightarrow e}$ for a muon neutrino generated in the atmosphere to reach the detector as an electron neutrino. L is the path length through the Earth (s. fig. 2.2), E is the neutrino energy.

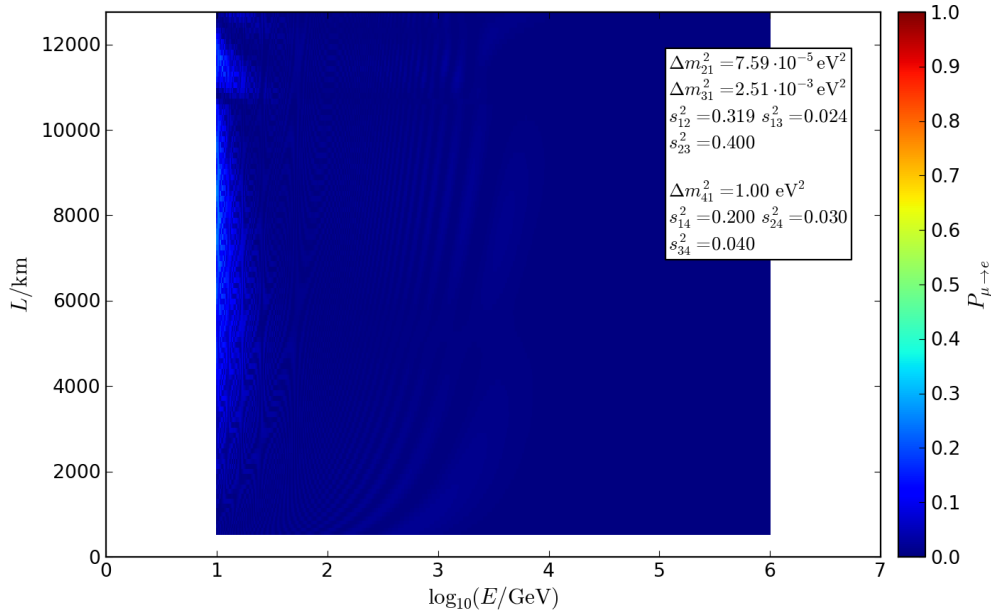


Figure A.25: Probability $P_{\mu \rightarrow e}$ for a muon neutrino generated in the atmosphere to reach the detector as an electron neutrino. L is the path length through the Earth (s. fig. 2.2), E is the neutrino energy.

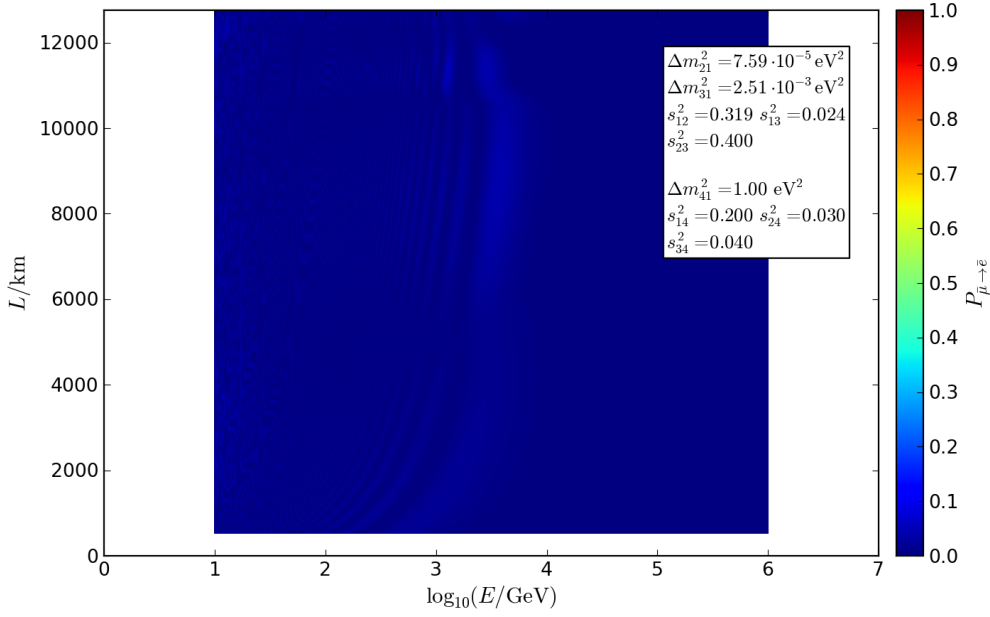


Figure A.26: Probability $P_{\bar{\mu} \rightarrow \bar{e}}$ for a muon antineutrino generated in the atmosphere to reach the detector as an electron antineutrino. L is the path length through the Earth (s. fig. 2.2), E is the neutrino energy.

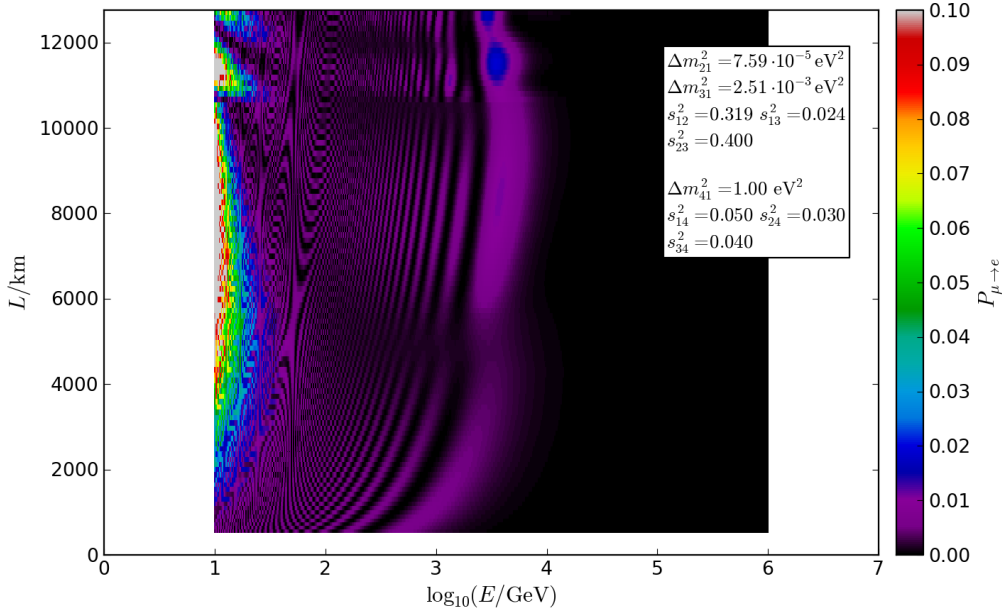


Figure A.27: Probability $P_{\mu \rightarrow e}$ for a muon neutrino generated in the atmosphere to reach the detector as an electron neutrino. L is the path length through the Earth (s. fig. 2.2), E is the neutrino energy.

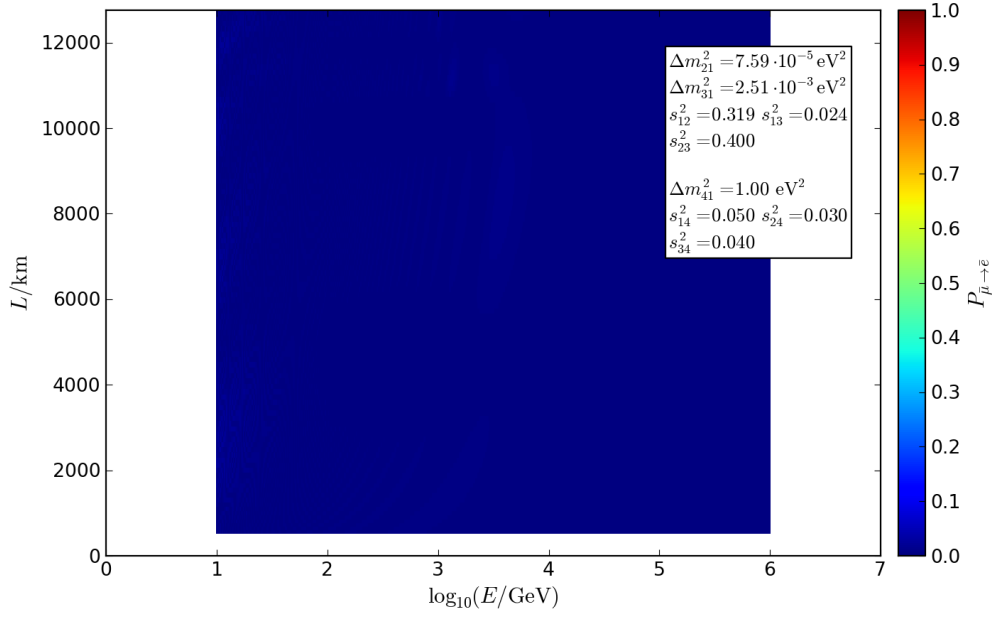


Figure A.28: Probability $P_{\bar{\mu} \rightarrow \bar{e}}$ for a muon antineutrino generated in the atmosphere to reach the detector as an electron antineutrino. L is the path length through the Earth (s. fig. 2.2), E is the neutrino energy.

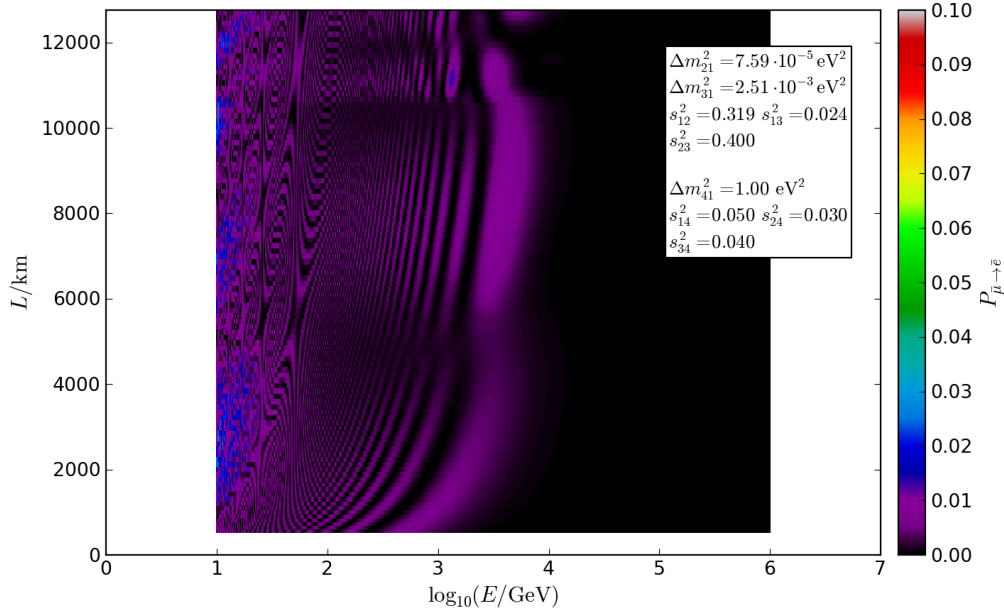
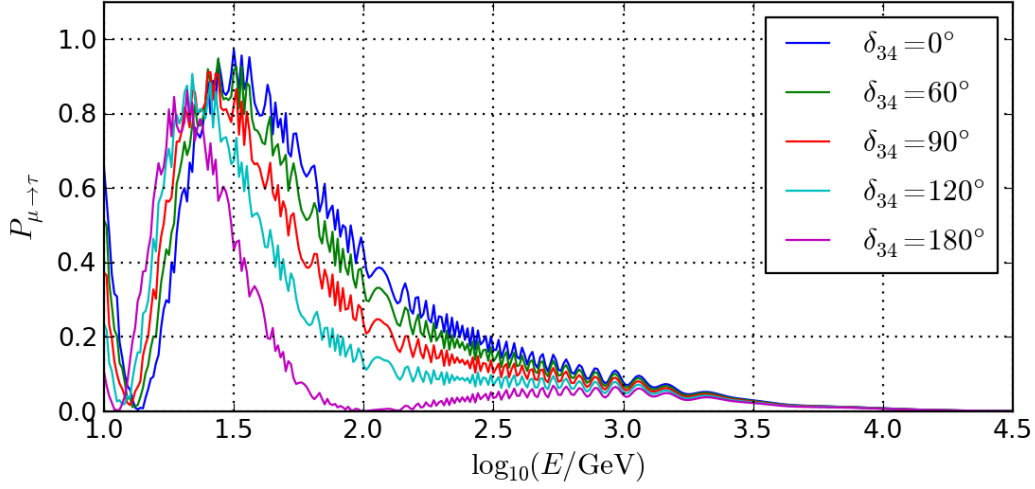


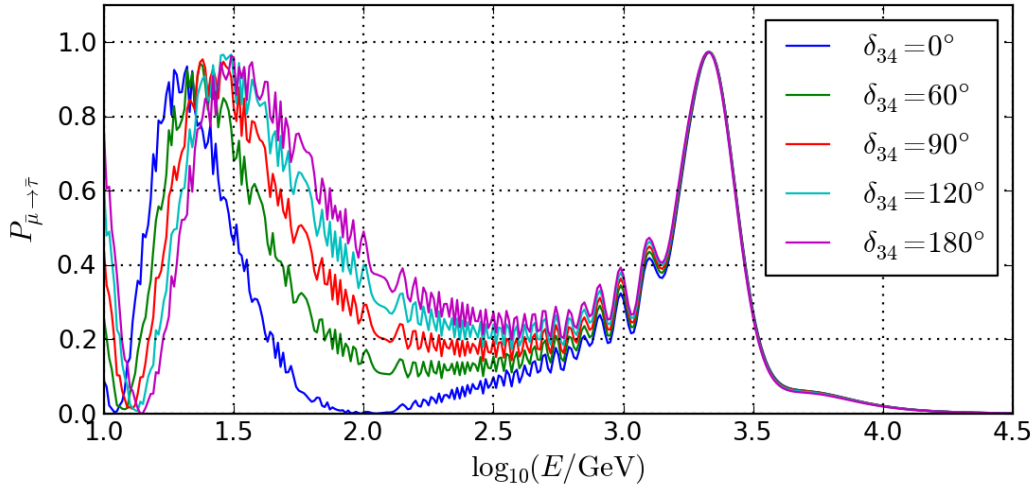
Figure A.29: Probability $P_{\bar{\mu} \rightarrow \bar{e}}$ for a muon antineutrino generated in the atmosphere to reach the detector as an electron antineutrino. L is the path length through the Earth (s. fig. 2.2), E is the neutrino energy.

A.6 CP-violating phases



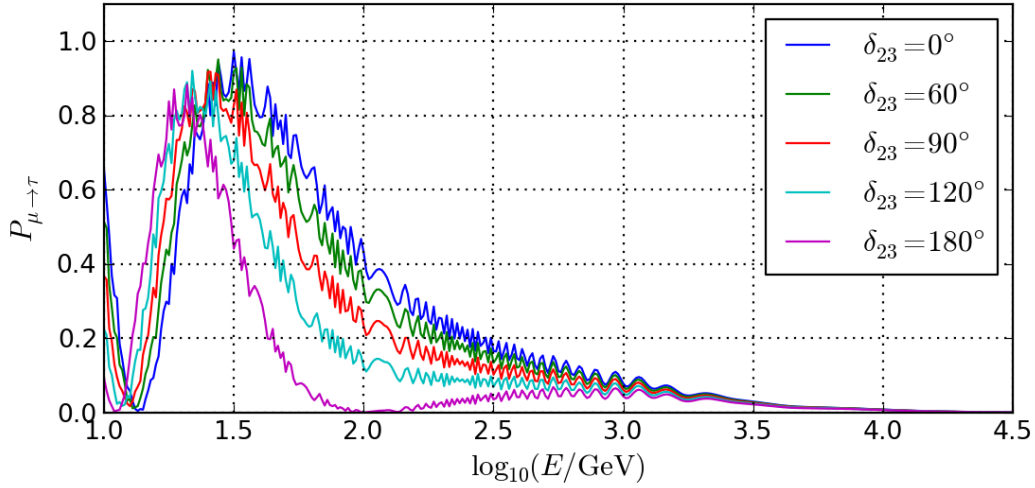
$$\begin{aligned} \Delta m_{41}^2 &= 1.00 \text{ eV}^2 & s_{14}^2 &= 0.050 & s_{24}^2 &= 0.030 & s_{34}^2 &= 0.040 & \delta_{13} &= 0^\circ & \delta_{24} &= 0^\circ \\ \Delta m_{21}^2 &= 7.59 \cdot 10^{-5} \text{ eV}^2 & \Delta m_{31}^2 &= 2.51 \cdot 10^{-3} \text{ eV}^2 & s_{12}^2 &= 0.319 & s_{13}^2 &= 0.024 & s_{23}^2 &= 0.400 \end{aligned}$$

Figure A.30: Probability $P_{\mu \rightarrow \tau}$ for a vertically incoming muon neutrino generated in the atmosphere to reach the detector as a tau neutrino, for various $\delta_{34} \neq 0^\circ$ with $\delta_{24} = \delta_{13} = 0^\circ$. E is the neutrino energy.



$$\begin{aligned} \Delta m_{41}^2 &= 1.00 \text{ eV}^2 & s_{14}^2 &= 0.050 & s_{24}^2 &= 0.030 & s_{34}^2 &= 0.040 & \delta_{13} &= 0^\circ & \delta_{24} &= 0^\circ \\ \Delta m_{21}^2 &= 7.59 \cdot 10^{-5} \text{ eV}^2 & \Delta m_{31}^2 &= 2.51 \cdot 10^{-3} \text{ eV}^2 & s_{12}^2 &= 0.319 & s_{13}^2 &= 0.024 & s_{23}^2 &= 0.400 \end{aligned}$$

Figure A.31: Probability $P_{\bar{\mu} \rightarrow \bar{\tau}}$ for a vertically incoming muon antineutrino generated in the atmosphere to reach the detector as a tau antineutrino, for various $\delta_{34} \neq 0^\circ$ with $\delta_{24} = \delta_{13} = 0^\circ$. E is the neutrino energy.



$$\begin{aligned} \Delta m_{41}^2 &= 1.00 \text{ eV}^2 & s_{14}^2 &= 0.050 & s_{24}^2 &= 0.030 & s_{34}^2 &= 0.040 & \delta_{14} &= 0^\circ & \delta_{24} &= 0^\circ \\ \Delta m_{21}^2 &= 7.59 \cdot 10^{-5} \text{ eV}^2 & \Delta m_{31}^2 &= 2.51 \cdot 10^{-3} \text{ eV}^2 & s_{12}^2 &= 0.319 & s_{13}^2 &= 0.024 & s_{23}^2 &= 0.400 \end{aligned}$$

Figure A.32: Probability $P_{\mu \rightarrow \tau}$ for a vertically incoming muon neutrino generated in the atmosphere to reach the detector as a tau neutrino, for various $\delta_{23} \neq 0^\circ$ with $\delta_{24} = \delta_{13} = 0^\circ$. E is the neutrino energy.

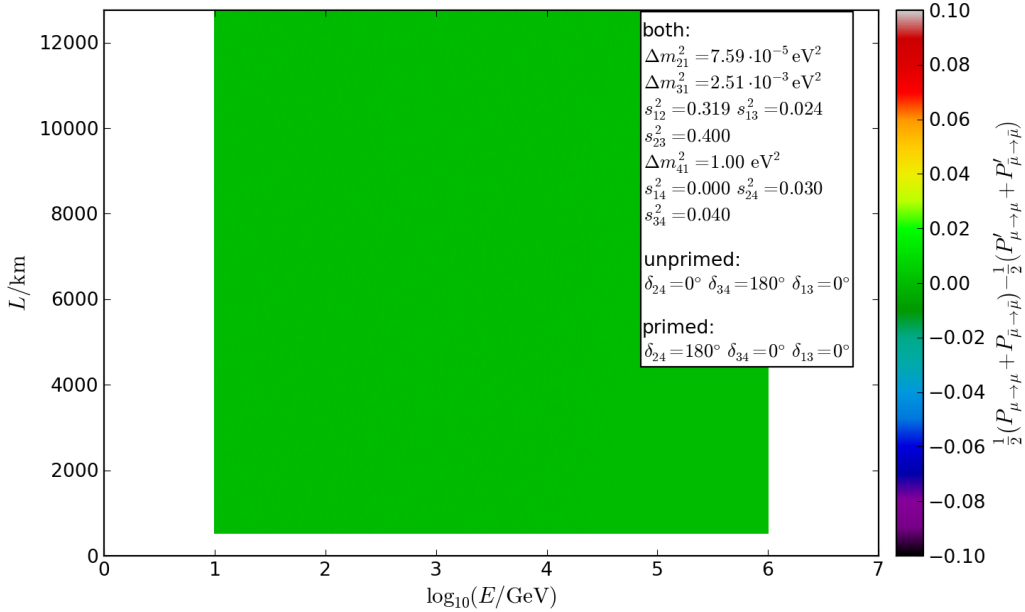


Figure A.33: Difference $\frac{1}{2} (P_{\mu \rightarrow \mu} + P_{\bar{\mu} \rightarrow \bar{\mu}}) - \frac{1}{2} (P'_{\mu \rightarrow \mu} + P'_{\bar{\mu} \rightarrow \bar{\mu}})$ between the probabilities, averaged over muon neutrinos and antineutrinos, for a particle generated in the atmosphere to reach the detector in the same state in which it was generated, between $\delta_{34} = 180^\circ$, $\delta_{24} = \delta_{13} = 0^\circ$ (unprimed) and $\delta_{24} = 180^\circ$, $\delta_{34} = \delta_{13} = 0^\circ$ (primed). L is the path length through the Earth (s. fig. 2.2), E is the neutrino energy.

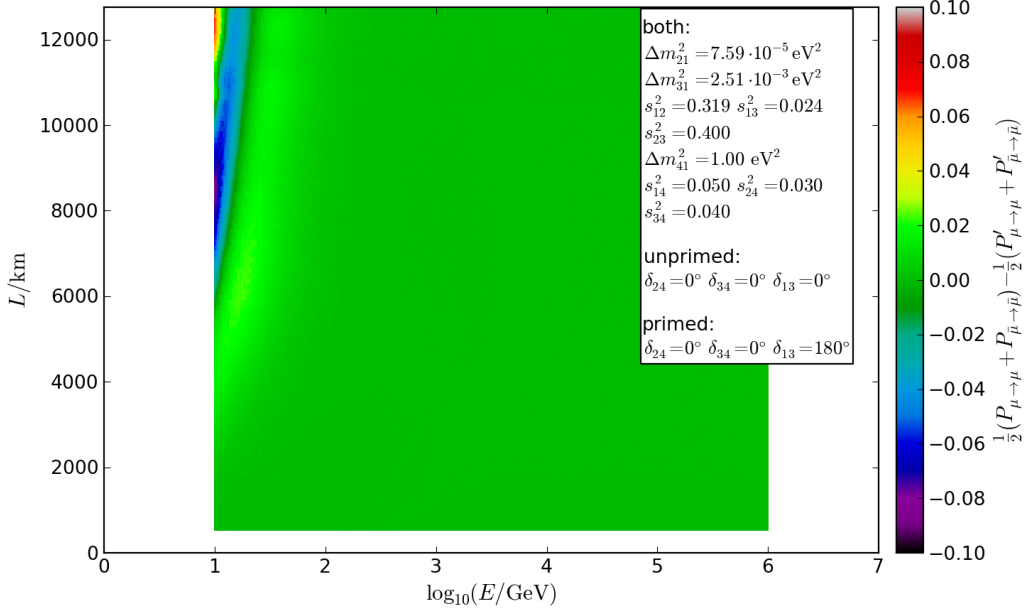


Figure A.34: Difference $\frac{1}{2} (P_{\mu \rightarrow \mu} + P_{\bar{\mu} \rightarrow \bar{\mu}}) - \frac{1}{2} (P'_{\mu \rightarrow \mu} + P'_{\bar{\mu} \rightarrow \bar{\mu}})$ between the probabilities, averaged over muon neutrinos and antineutrinos, for a particle generated in the atmosphere to reach the detector in the same state in which it was generated, between $\delta_{34} = 0^\circ$, $\delta_{24} = \delta_{13} = 0^\circ$ (unprimed) and $\delta_{13} = 180^\circ$, $\delta_{34} = \delta_{24} = 0^\circ$ (primed). L is the path length through the Earth (s. fig. 2.2), E is the neutrino energy.

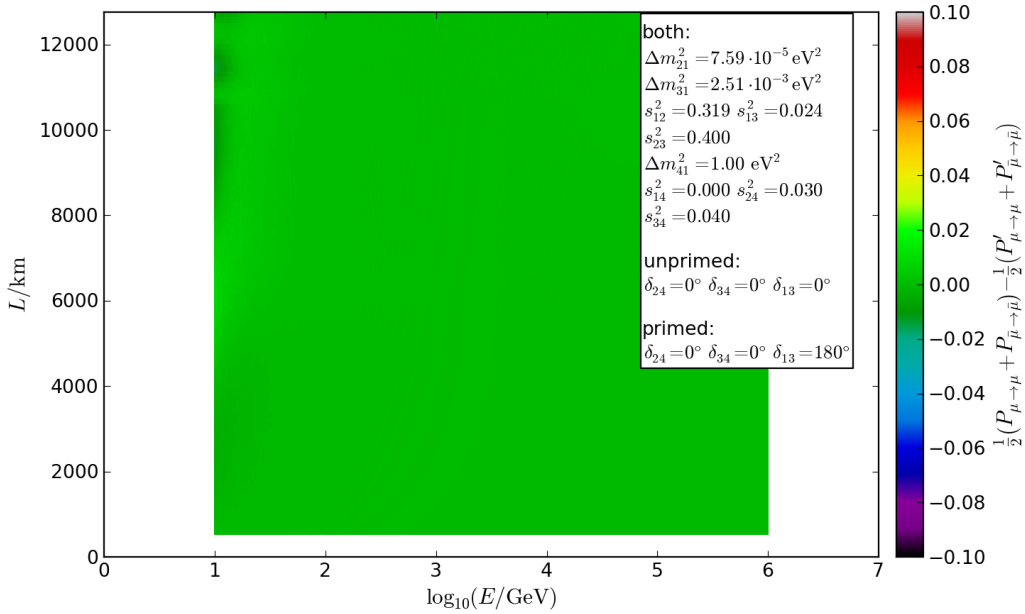
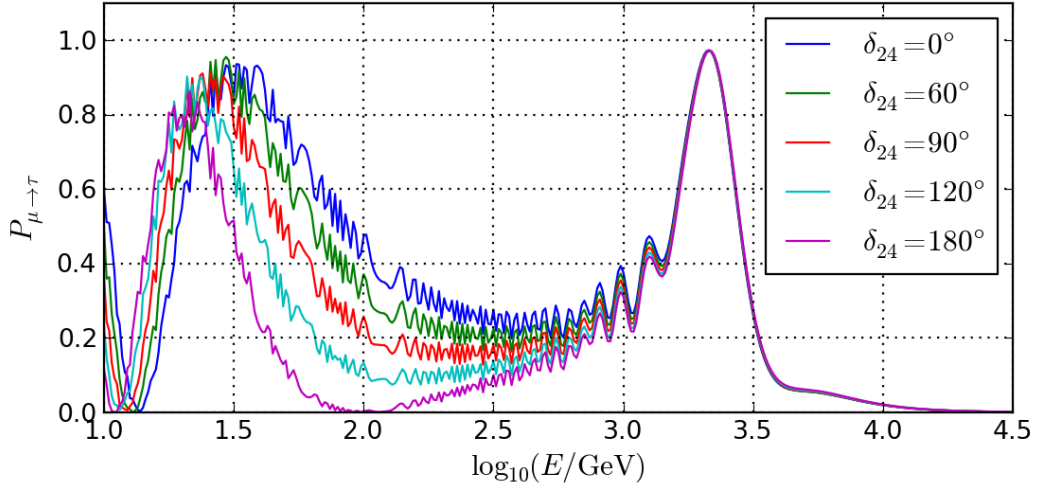
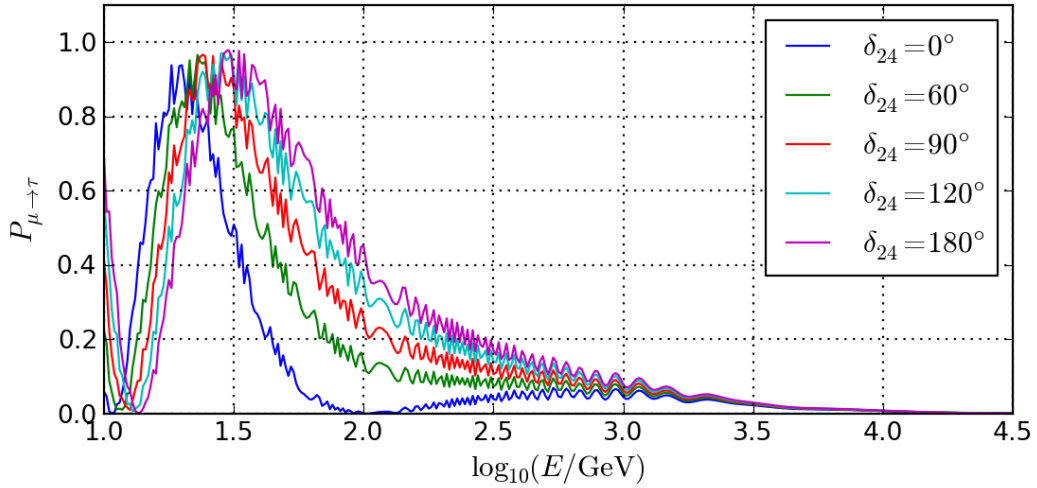


Figure A.35: Difference $\frac{1}{2} (P_{\mu \rightarrow \mu} + P_{\bar{\mu} \rightarrow \bar{\mu}}) - \frac{1}{2} (P'_{\mu \rightarrow \mu} + P'_{\bar{\mu} \rightarrow \bar{\mu}})$ between the probabilities, averaged over muon neutrinos and antineutrinos, for a particle generated in the atmosphere to reach the detector in the same state in which it was generated, between $\delta_{34} = 0^\circ$, $\delta_{24} = \delta_{13} = 0^\circ$ (unprimed) and $\delta_{13} = 180^\circ$, $\delta_{34} = \delta_{24} = 0^\circ$ (primed). L is the path length through the Earth (s. fig. 2.2), E is the neutrino energy.



$$\begin{aligned} \Delta m_{41}^2 &= -1.00 \text{ eV}^2 & s_{14}^2 &= 0.050 & s_{24}^2 &= 0.030 & s_{34}^2 &= 0.040 & \delta_{13} &= 0^\circ & \delta_{34} &= 0^\circ \\ \Delta m_{21}^2 &= 7.59 \cdot 10^{-5} \text{ eV}^2 & \Delta m_{31}^2 &= 2.51 \cdot 10^{-3} \text{ eV}^2 & s_{12}^2 &= 0.319 & s_{13}^2 &= 0.024 & s_{23}^2 &= 0.400 \end{aligned}$$

Figure A.36: Probability $P_{\mu \rightarrow \tau}$ for a vertically incoming muon neutrino generated in the atmosphere to reach the detector as a tau neutrino, for various $\delta_{24} \neq 0^\circ$ with $\delta_{34} = \delta_{13} = 0^\circ$. E is the neutrino energy.



$$\begin{aligned} \Delta m_{41}^2 &= 1.00 \text{ eV}^2 & s_{14}^2 &= 0.050 & s_{24}^2 &= 0.030 & s_{34}^2 &= 0.040 & \delta_{13} &= 0^\circ & \delta_{34} &= 0^\circ \\ \Delta m_{21}^2 &= 7.59 \cdot 10^{-5} \text{ eV}^2 & \Delta m_{31}^2 &= -2.35 \cdot 10^{-3} \text{ eV}^2 & s_{12}^2 &= 0.319 & s_{13}^2 &= 0.024 & s_{23}^2 &= 0.400 \end{aligned}$$

Figure A.37: Probability $P_{\mu \rightarrow \tau}$ for a vertically incoming muon neutrino generated in the atmosphere to reach the detector as a tau neutrino, for various $\delta_{24} \neq 0^\circ$ with $\delta_{34} = \delta_{13} = 0^\circ$. E is the neutrino energy.

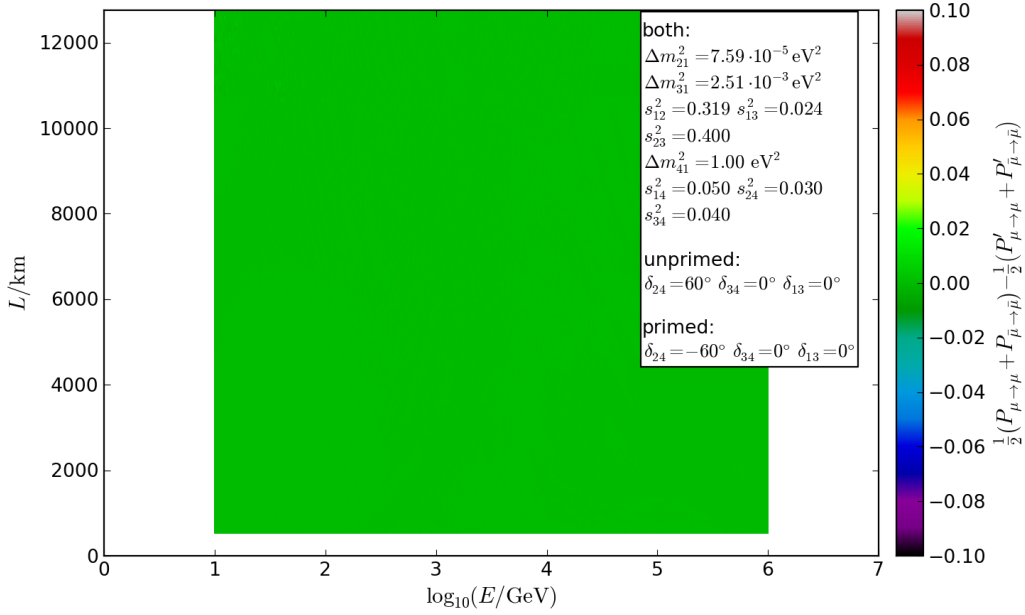
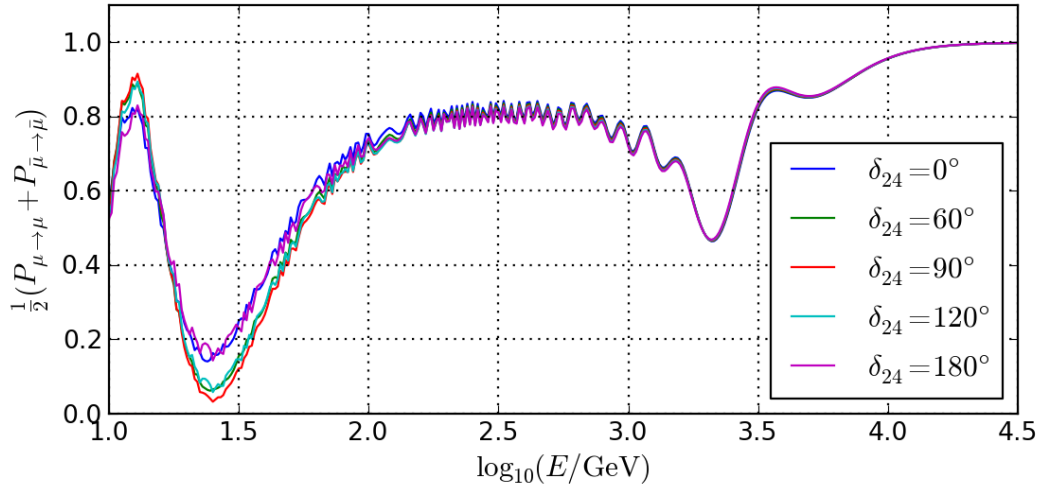


Figure A.38: Difference $\frac{1}{2} (P_{\mu \rightarrow \mu} + P_{\bar{\mu} \rightarrow \bar{\mu}}) - \frac{1}{2} (P'_{\mu \rightarrow \mu} + P'_{\bar{\mu} \rightarrow \bar{\mu}})$ between the probabilities, averaged over muon neutrinos and antineutrinos, for a particle generated in the atmosphere to reach the detector in the same state in which it was generated, between $\delta_{24} = 60^\circ$, $\delta_{34} = \delta_{13} = 0^\circ$ (unprimed) and $\delta_{24} = -60^\circ$, $\delta_{34} = \delta_{13} = 0^\circ$ (primed). L is the path length through the Earth (s. fig. 2.2), E is the neutrino energy.



$$\Delta m_{41}^2 = 1.00 \text{ eV}^2 \quad s_{14}^2 = 0.050 \quad s_{24}^2 = 0.030 \quad s_{34}^2 = 0.040 \quad \delta_{13} = 0^\circ \quad \delta_{34} = 0^\circ$$

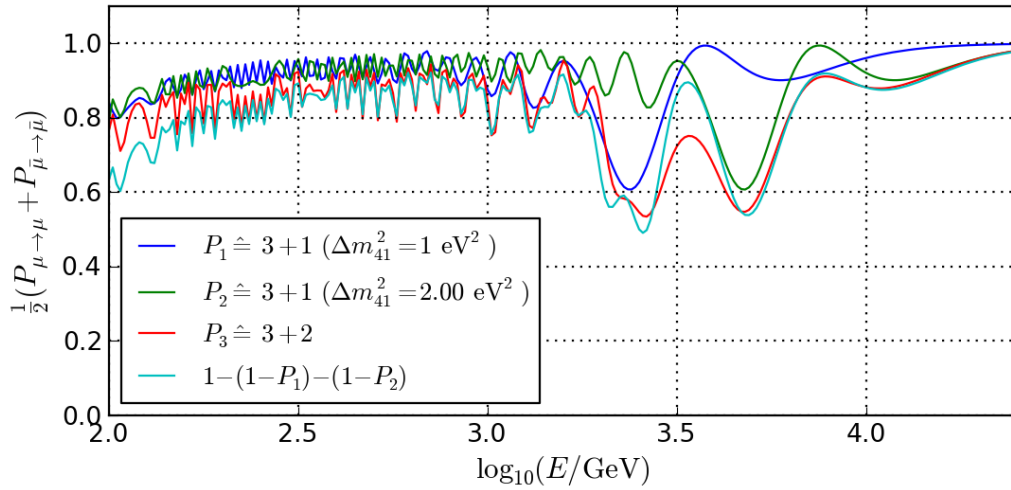
$$\Delta m_{21}^2 = 7.59 \cdot 10^{-5} \text{ eV}^2 \quad \Delta m_{31}^2 = 2.51 \cdot 10^{-3} \text{ eV}^2 \quad s_{12}^2 = 0.319 \quad s_{13}^2 = 0.024 \quad s_{23}^2 = 0.400$$

Figure A.39: Probability $\frac{1}{2} (P_{\mu \rightarrow \mu} + P_{\bar{\mu} \rightarrow \bar{\mu}})$, averaged over muon neutrinos and antineutrinos, for a vertically incoming particle generated in the atmosphere to reach the detector in the same state in which it was generated, for various $\delta_{24} \neq 0^\circ$ with $\delta_{34} = \delta_{13} = 0^\circ$. E is the neutrino energy.

Appendix B

3+2 model

B.1 Impact of the relative sign of Δm_{41}^2 and Δm_{51}^2



$$\begin{aligned} \Delta m_{41}^2 &= 1.00 \text{ eV}^2 & \Delta m_{51}^2 &= 2.00 \text{ eV}^2 & s_{24}^2 = s_{25}^2 &= 0.030 & s_{i4}^2 = s_{i5}^2 &= 0 \quad (i=1,3) \\ \Delta m_{21}^2 &= 7.59 \cdot 10^{-5} \text{ eV}^2 & \Delta m_{31}^2 &= 2.51 \cdot 10^{-3} \text{ eV}^2 & s_{12}^2 &= 0.319 & s_{13}^2 &= 0.024 & s_{23}^2 &= 0.400 \end{aligned}$$

Figure B.1: Probability $\frac{1}{2}(P_{\mu \rightarrow \mu} + P_{\bar{\mu} \rightarrow \bar{\mu}})$, averaged over muon neutrinos and antineutrinos, for a vertically incoming particle generated in the atmosphere to reach the detector in the same state in which it was generated. E is the neutrino energy.

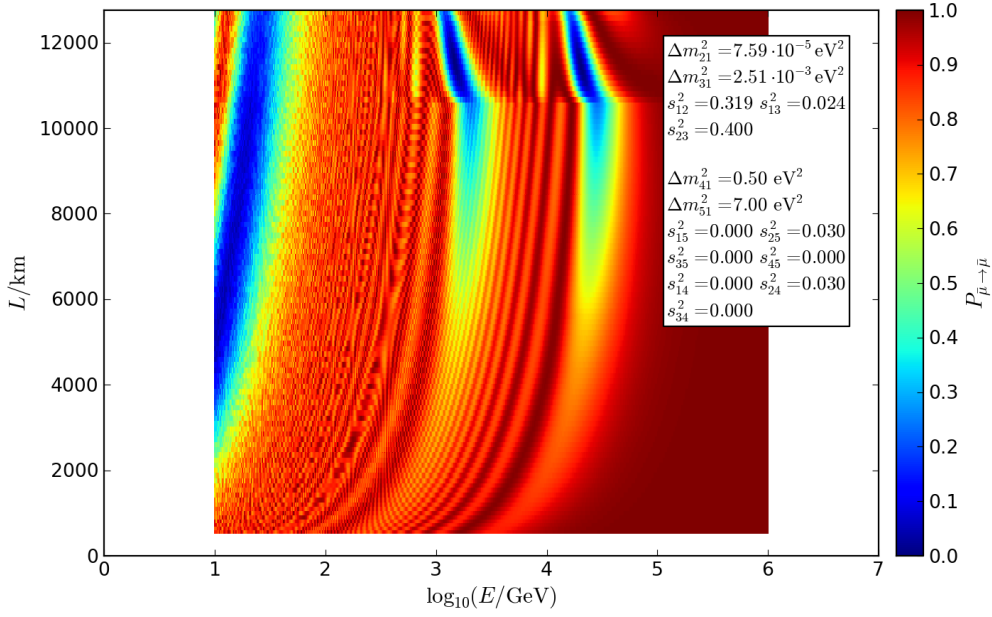


Figure B.2: Probability $P_{\bar{\mu} \rightarrow \bar{\mu}}$ for a muon antineutrino generated in the atmosphere to reach the detector as a muon antineutrino. L is the path length through the Earth (s. fig. 2.2), E is the neutrino energy.

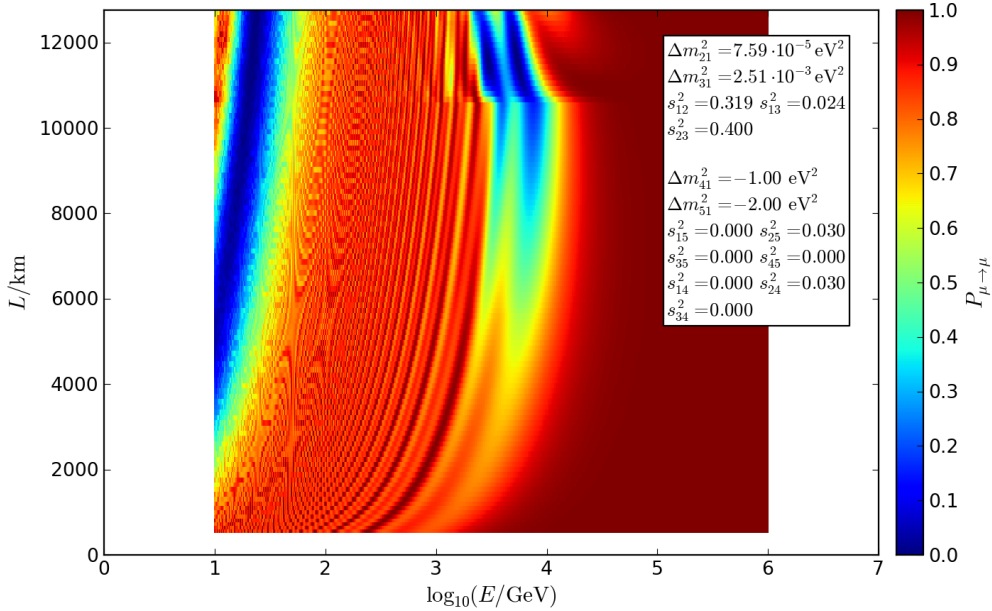


Figure B.3: Probability $P_{\mu \rightarrow \mu}$ for a muon neutrino generated in the atmosphere to reach the detector as a muon neutrino. L is the path length through the Earth (s. fig. 2.2), E is the neutrino energy.

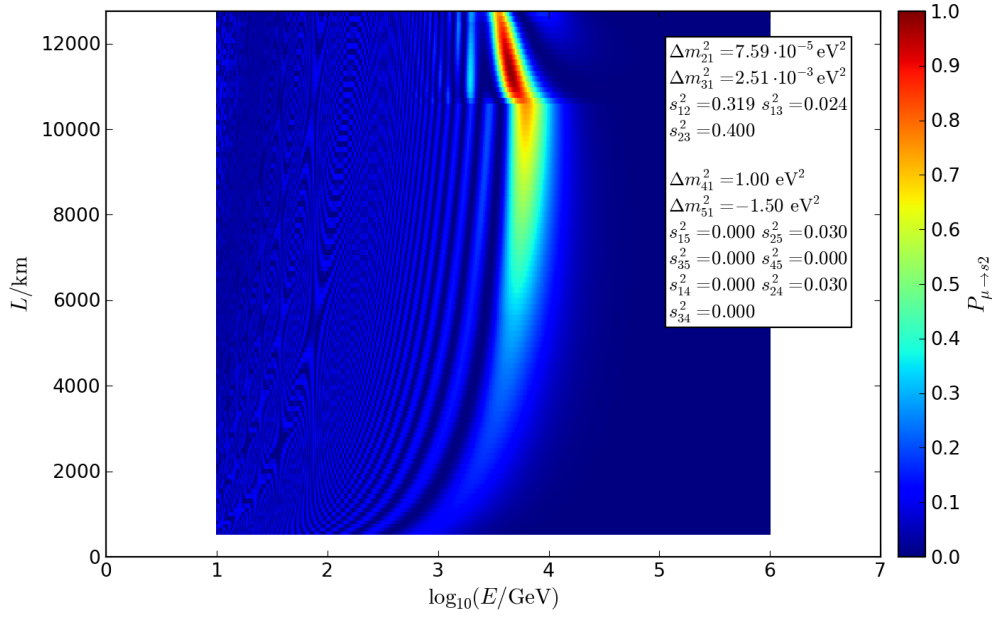


Figure B.4: Probability $P_{\mu \rightarrow s2}$ for a muon neutrino generated in the atmosphere to reach the detector in state $s2$. L is the path length through the Earth (s. fig. 2.2), E is the neutrino energy.

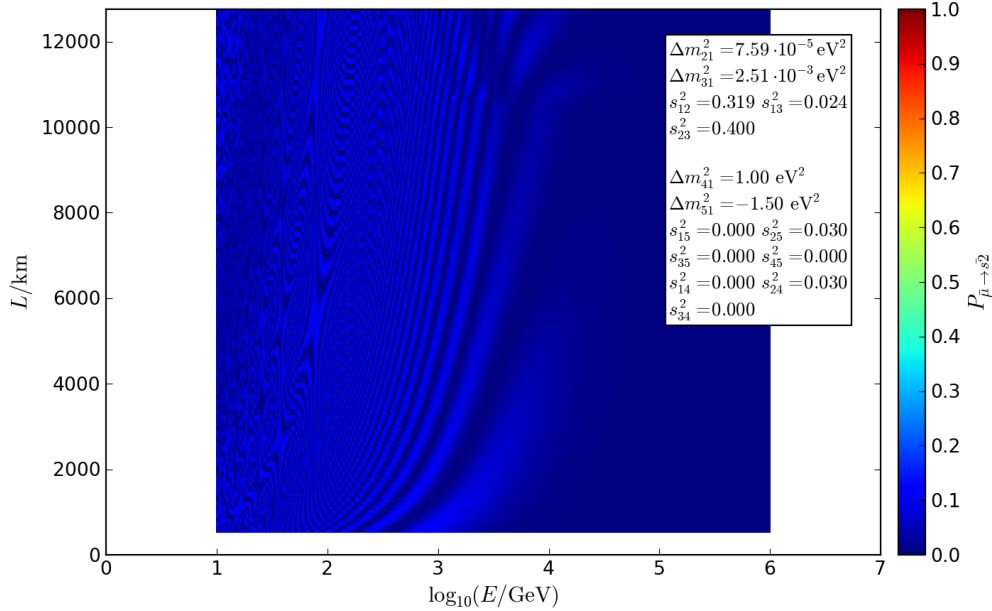


Figure B.5: Probability $P_{\bar{\mu} \rightarrow \bar{s}2}$ for a muon antineutrino generated in the atmosphere to reach the detector in state $\bar{s}2$. L is the path length through the Earth (s. fig. 2.2), E is the neutrino energy.

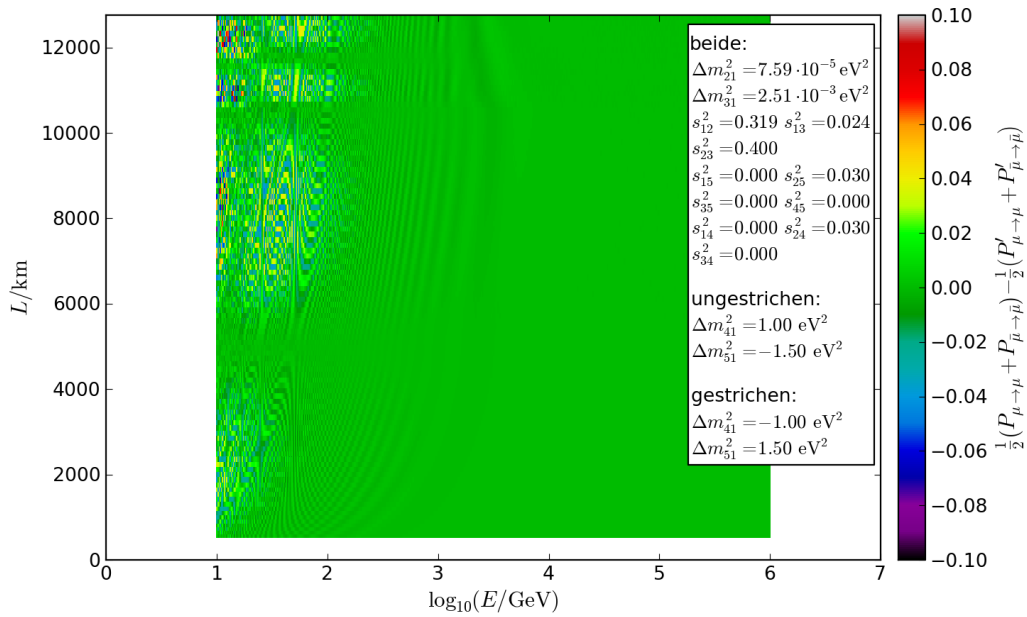


Figure B.6: Difference $\frac{1}{2}(P_{\mu \rightarrow \mu} + P_{\bar{\mu} \rightarrow \bar{\mu}}) - \frac{1}{2}(P'_{\mu \rightarrow \mu} + P'_{\bar{\mu} \rightarrow \bar{\mu}})$ between the probabilities, averaged over muon neutrinos and antineutrinos, for a particle generated in the atmosphere to reach the detector in the same state in which it was generated, between $\Delta m_{41}^2 = 1.00 \text{ eV}^2$, $\Delta m_{51}^2 = -1.50 \text{ eV}^2$ (unprimed) and $\Delta m_{41}^2 = -1.00 \text{ eV}^2$, $\Delta m_{51}^2 = 1.50 \text{ eV}^2$ (primed). L is the path length through the Earth (s. fig. 2.2), E is the neutrino energy.

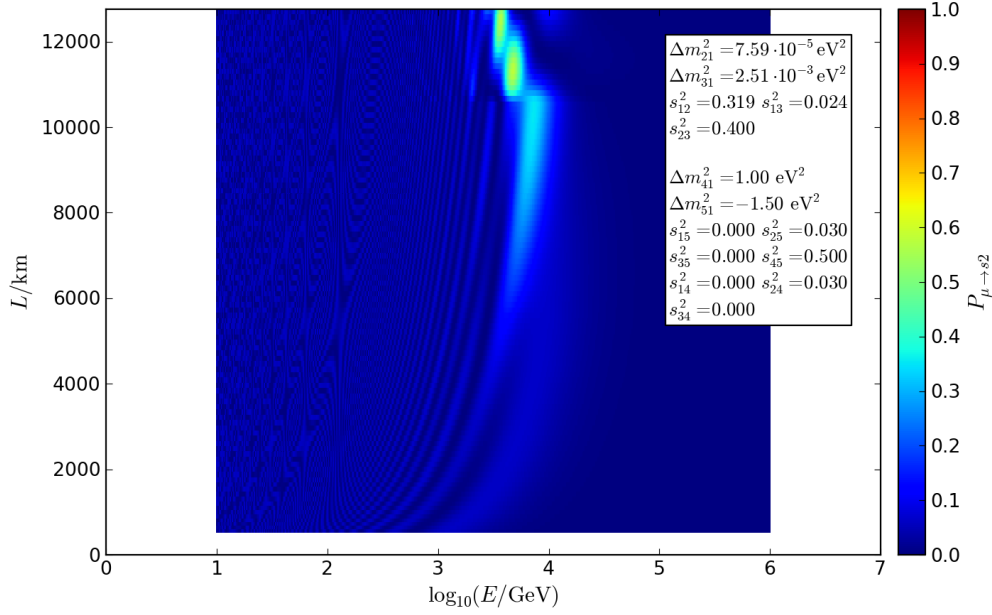


Figure B.7: Probability $P_{\mu \rightarrow s2}$ for a muon neutrino generated in the atmosphere to reach the detector in state $s2$. L is the path length through the Earth (s. fig. 2.2), E is the neutrino energy.

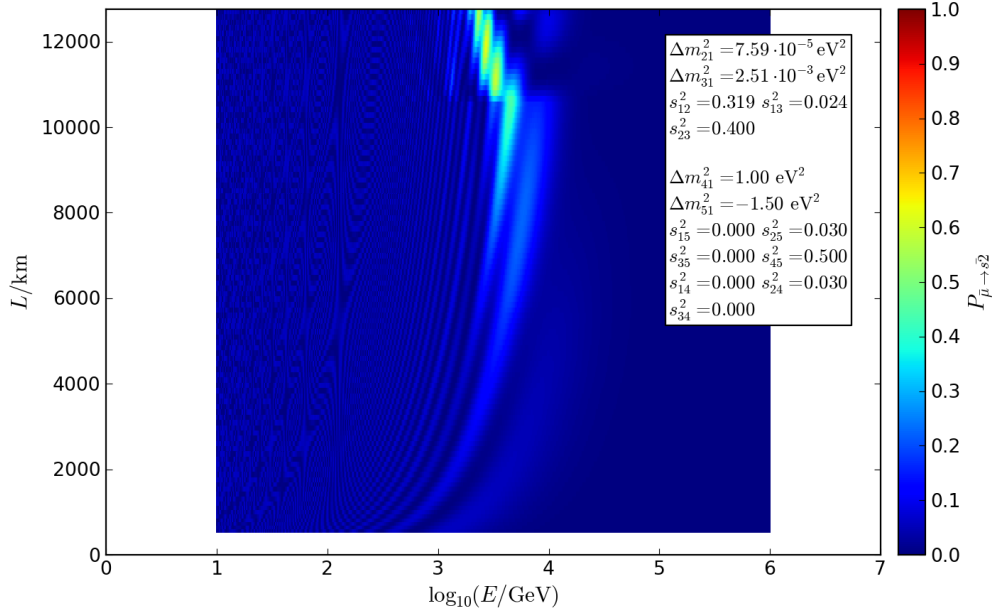


Figure B.8: Probability $P_{\bar{\mu} \rightarrow \bar{s}2}$ for a muon antineutrino generated in the atmosphere to reach the detector in state $\bar{s}2$. L is the path length through the Earth (s. fig. 2.2), E is the neutrino energy.

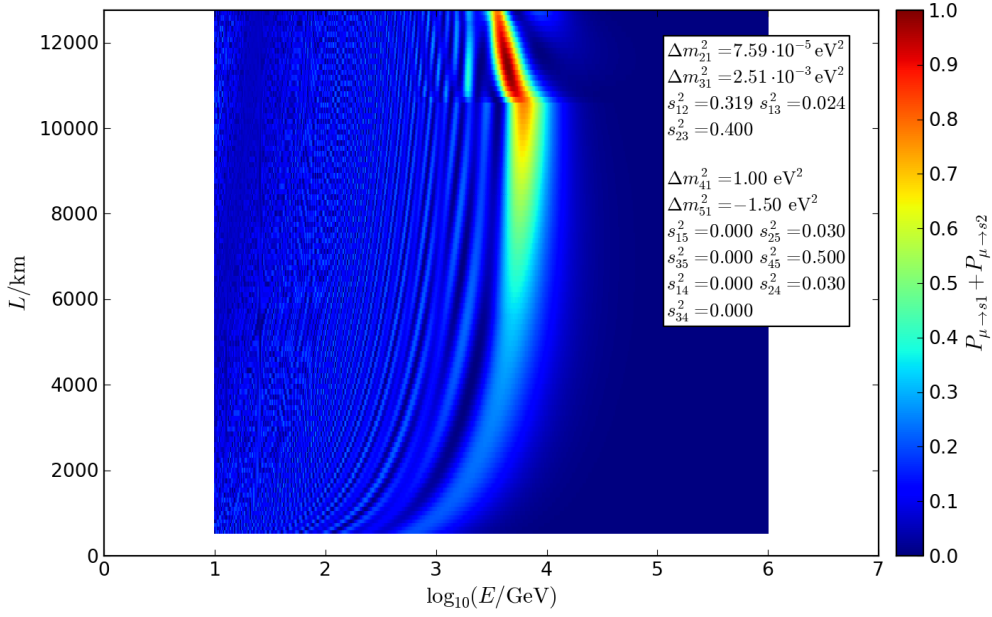


Figure B.9: Probability $P_{\mu \rightarrow s1} + P_{\mu \rightarrow s2}$ for a muon neutrino generated in the atmosphere to reach the detector in state $s1$ or $s2$. L is the path length through the Earth (s. fig. 2.2), E is the neutrino energy.

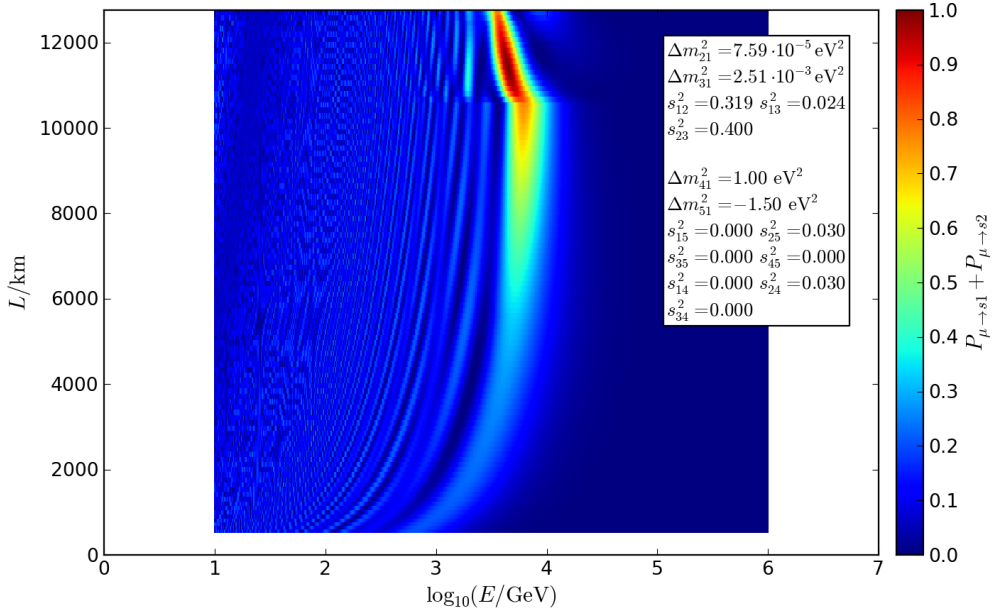


Figure B.10: Probability $P_{\mu \rightarrow s1} + P_{\mu \rightarrow s2}$ for a muon neutrino generated in the atmosphere to reach the detector in state $s1$ or $s2$. L is the path length through the Earth (s. fig. 2.2), E is the neutrino energy.

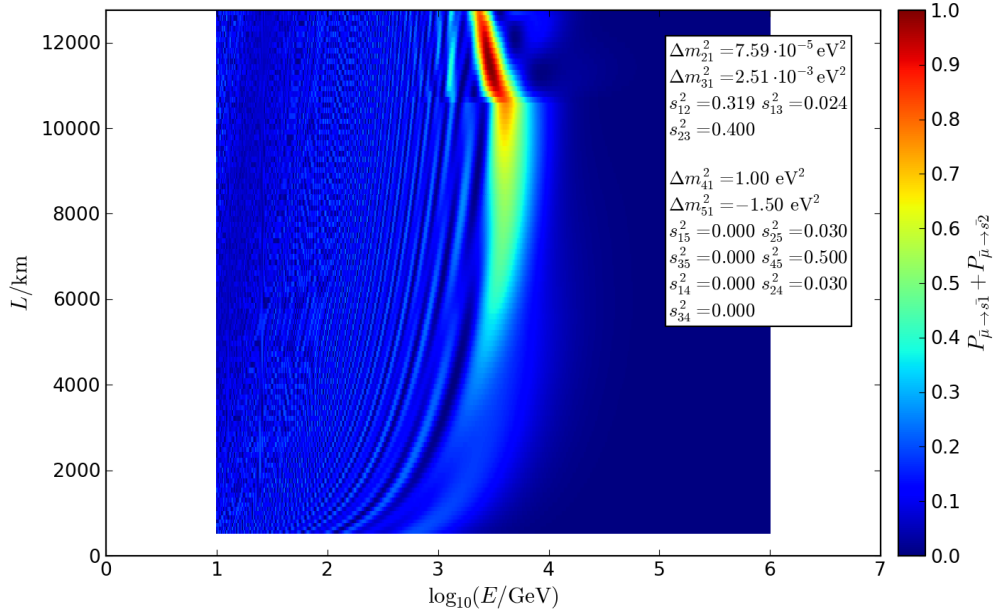


Figure B.11: Probability $P_{\bar{\mu} \rightarrow \bar{s}1} + P_{\bar{\mu} \rightarrow \bar{s}2}$ for a muon antineutrino generated in the atmosphere to reach the detector in state $\bar{s}1$ or $\bar{s}2$. L is the path length through the Earth (s. fig. 2.2), E is the neutrino energy.

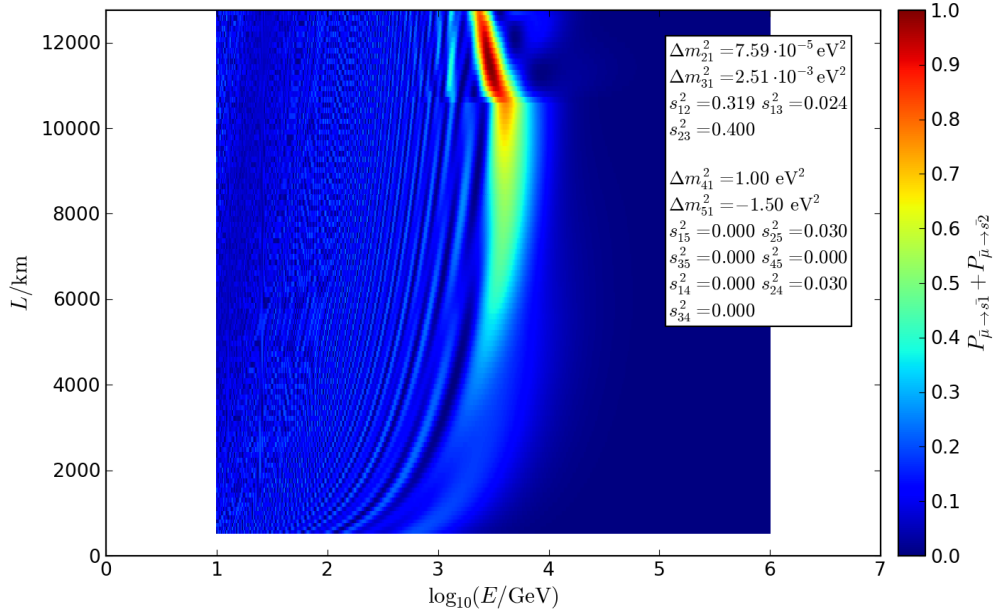


Figure B.12: Probability $P_{\bar{\mu} \rightarrow \bar{s}1} + P_{\bar{\mu} \rightarrow \bar{s}2}$ for a muon antineutrino generated in the atmosphere to reach the detector in state $\bar{s}1$ or $\bar{s}2$. L is the path length through the Earth (s. fig. 2.2), E is the neutrino energy.

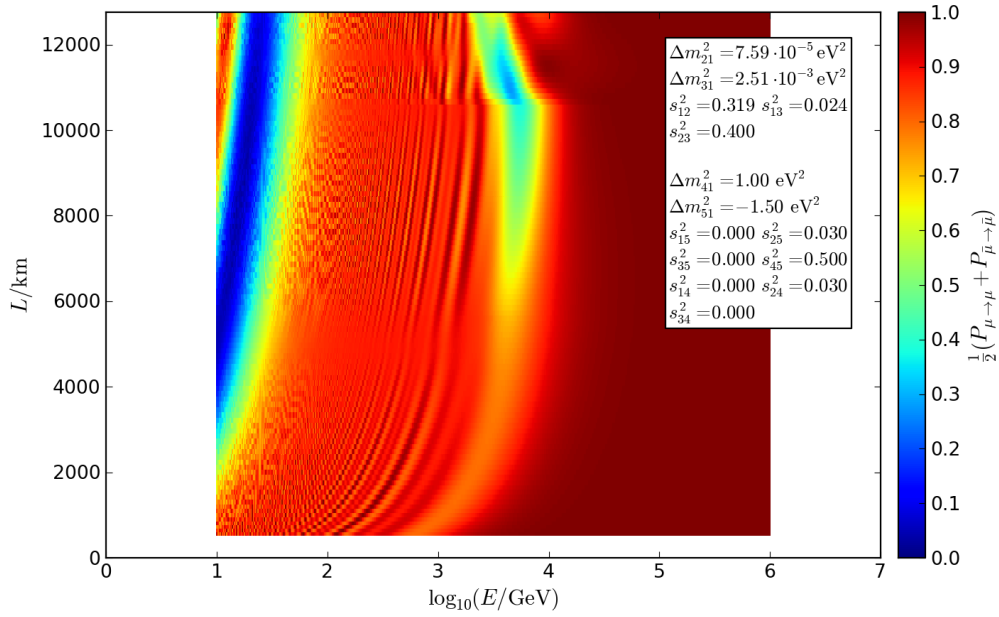


Figure B.13: Probability $\frac{1}{2}(P_{\mu \rightarrow \mu} + P_{\bar{\mu} \rightarrow \bar{\mu}})$, averaged over muon neutrinos and antineutrinos, for a particle generated in the atmosphere to reach the detector in the same state in which it was generated. L is the path length through the Earth (s. fig. 2.2), E is the neutrino energy.

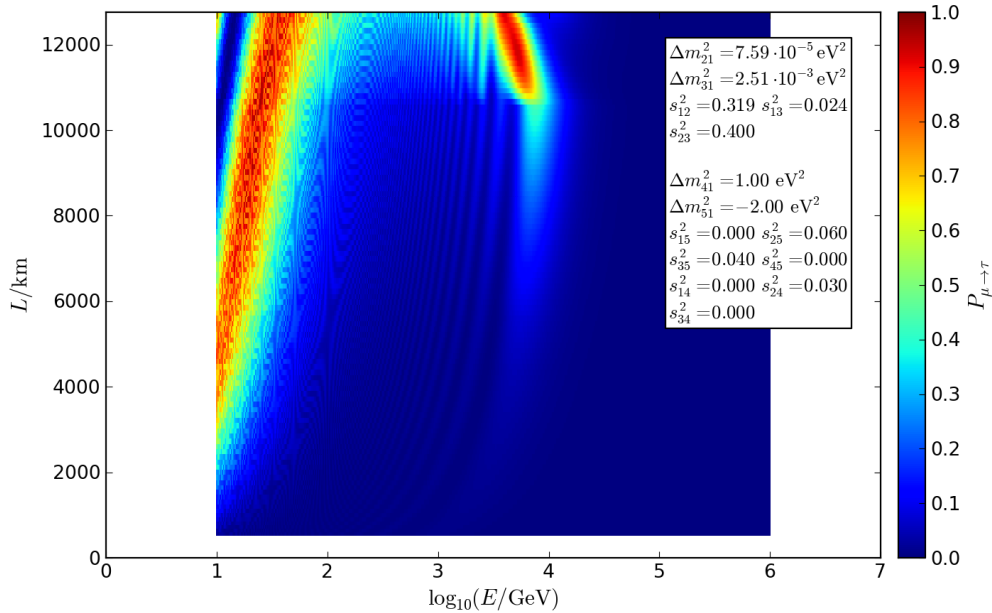


Figure B.14: Probability $P_{\mu \rightarrow \tau}$ for a muon neutrino generated in the atmosphere to reach the detector as a tau neutrino. L is the path length through the Earth (s. fig. 2.2), E is the neutrino energy.

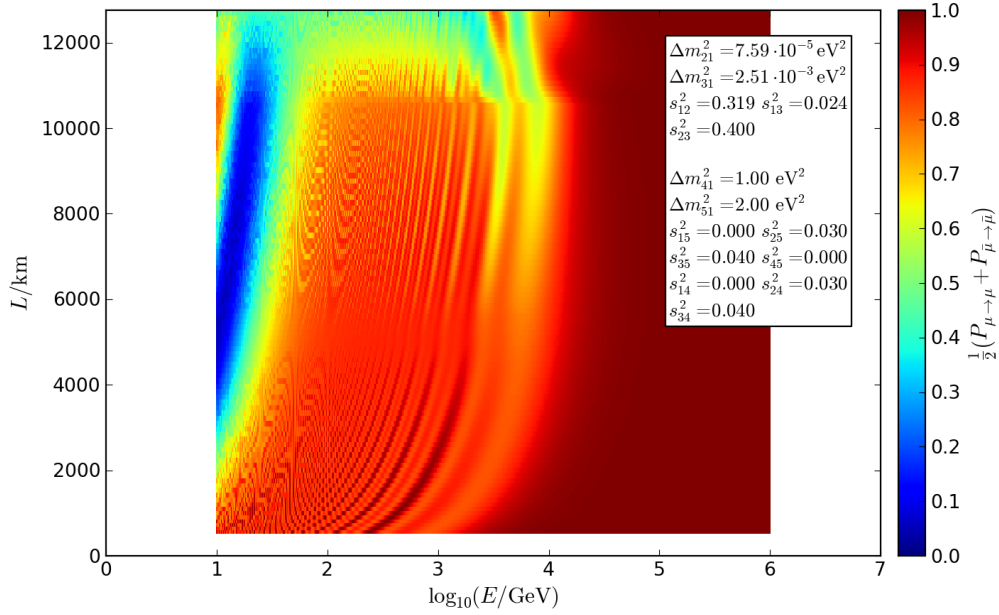


Figure B.15: Probability $\frac{1}{2}(P_{\mu \rightarrow \mu} + P_{\bar{\mu} \rightarrow \bar{\mu}})$, averaged over muon neutrinos and antineutrinos, for a particle generated in the atmosphere to reach the detector in the same state in which it was generated. L is the path length through the Earth (s. fig. 2.2), E is the neutrino energy.

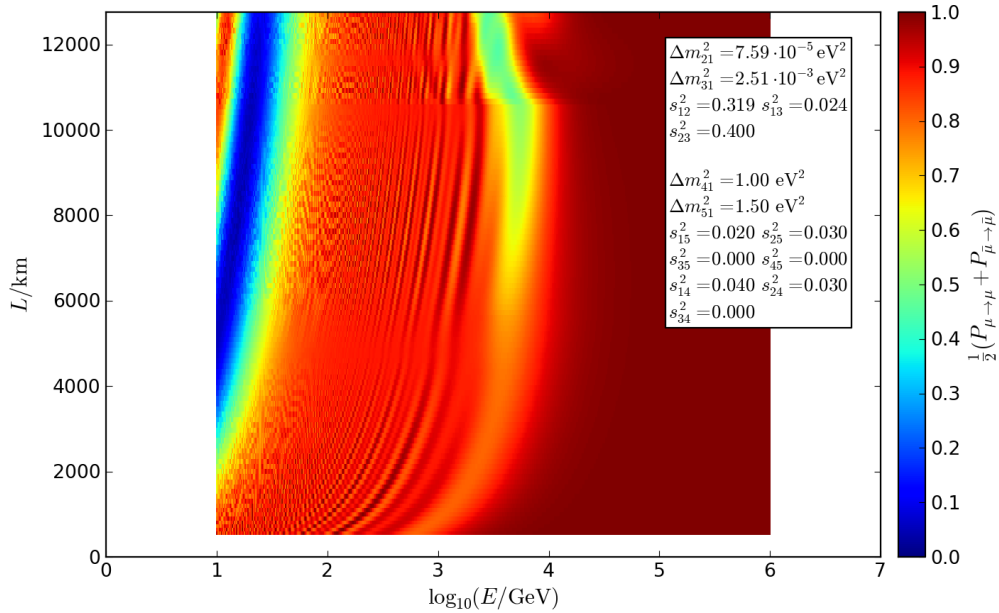


Figure B.16: Probability $\frac{1}{2}(P_{\mu \rightarrow \mu} + P_{\bar{\mu} \rightarrow \bar{\mu}})$, averaged over muon neutrinos and antineutrinos, for a particle generated in the atmosphere to reach the detector in the same state in which it was generated. L is the path length through the Earth (s. fig. 2.2), E is the neutrino energy.

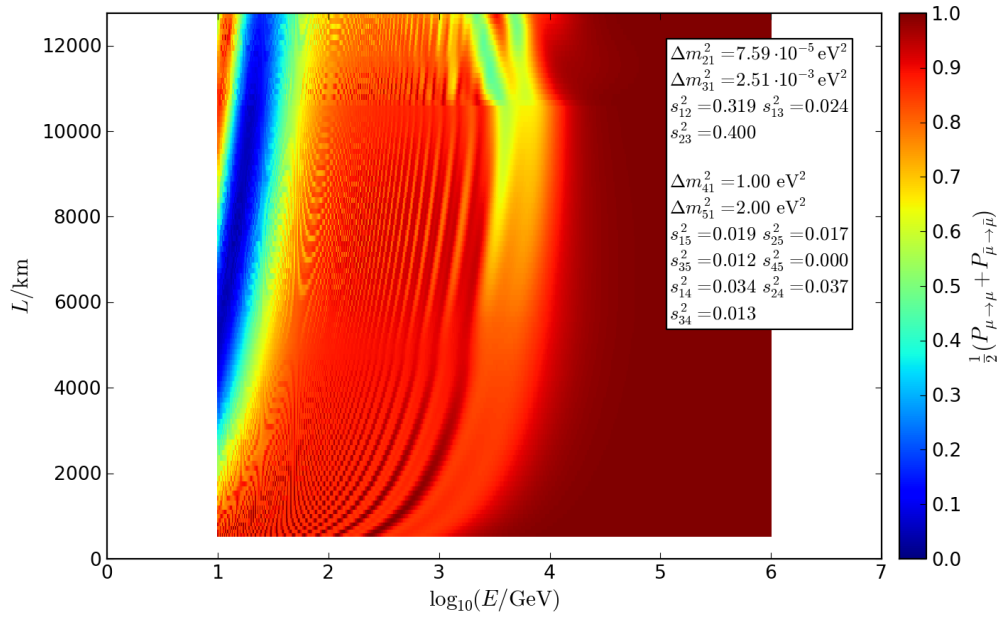
B.2 Impact of the ratio $\Delta m_{41}^2 \div \Delta m_{51}^2$


Figure B.17: Probability $\frac{1}{2}(P_{\mu \rightarrow \mu} + P_{\bar{\mu} \rightarrow \bar{\mu}})$, averaged over muon neutrinos and antineutrinos, for a particle generated in the atmosphere to reach the detector in the same state in which it was generated. L is the path length through the Earth (s. fig. 2.2), E is the neutrino energy.

B.3 Impact of the angle distribution

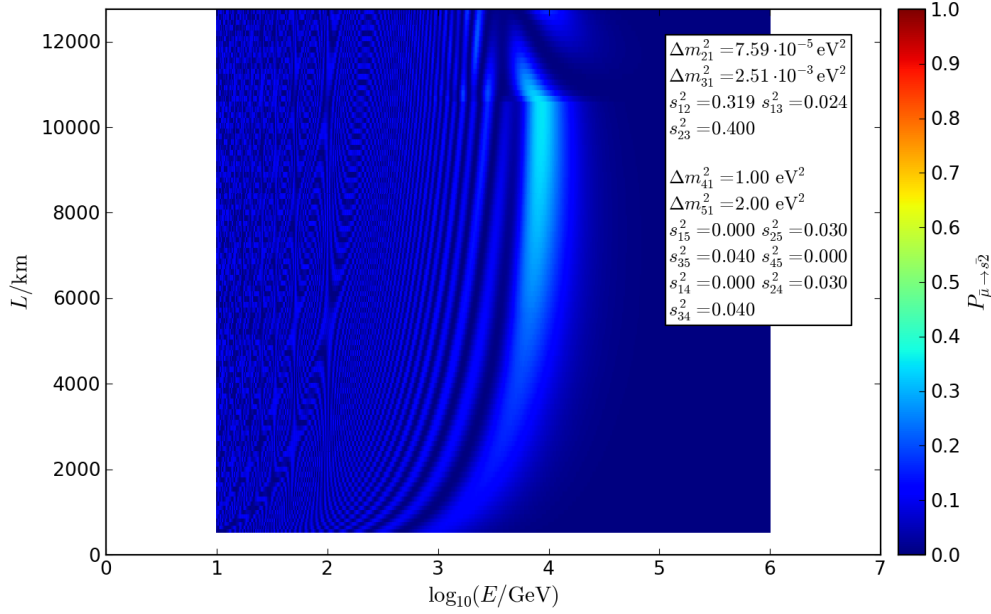


Figure B.18: Probability $P_{\bar{\mu} \rightarrow s2}$ for a muon antineutrino generated in the atmosphere to reach the detector in state $s2$. L is the path length through the Earth (s. fig. 2.2), E is the neutrino energy.

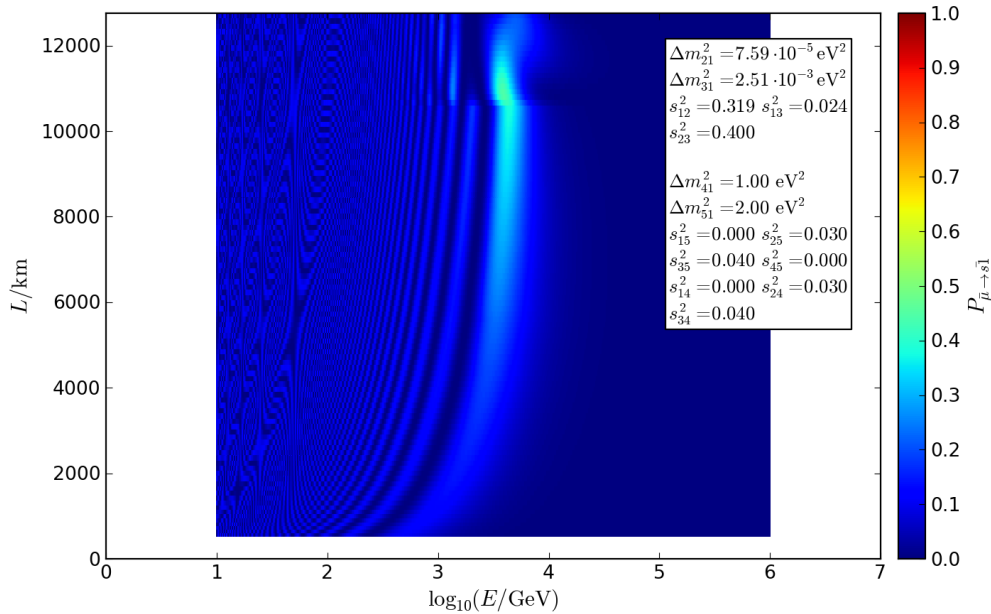


Figure B.19: Probability $P_{\bar{\mu} \rightarrow s1}$ for a muon antineutrino generated in the atmosphere to reach the detector in state $s1$. L is the path length through the Earth (s. fig. 2.2), E is the neutrino energy.

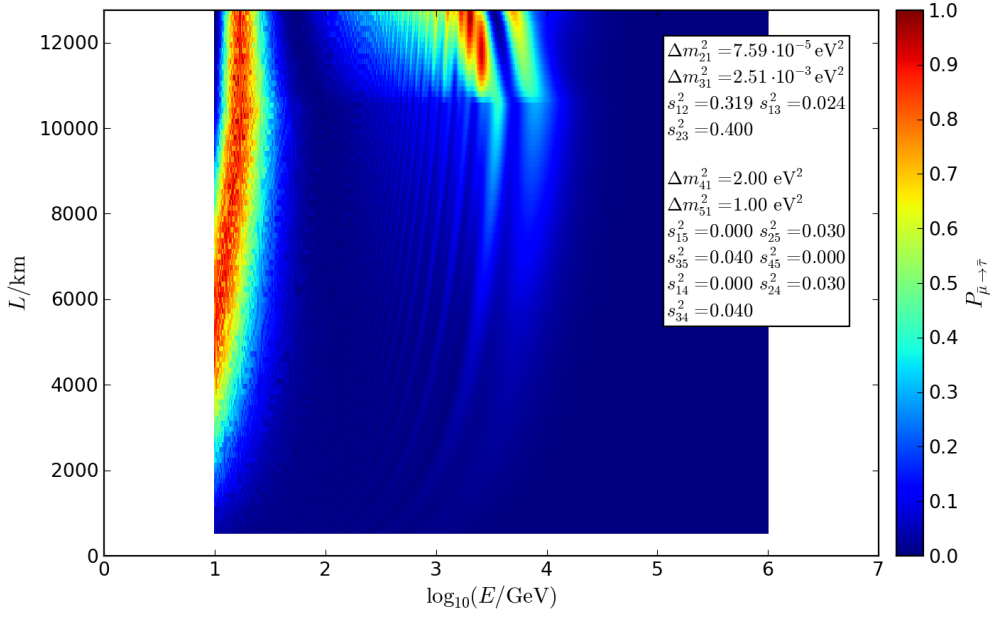


Figure B.20: Probability $P_{\bar{\mu} \rightarrow \bar{\tau}}$ for a muon antineutrino generated in the atmosphere to reach the detector as a tau antineutrino. L is the path length through the Earth (s. fig. 2.2), E is the neutrino energy.

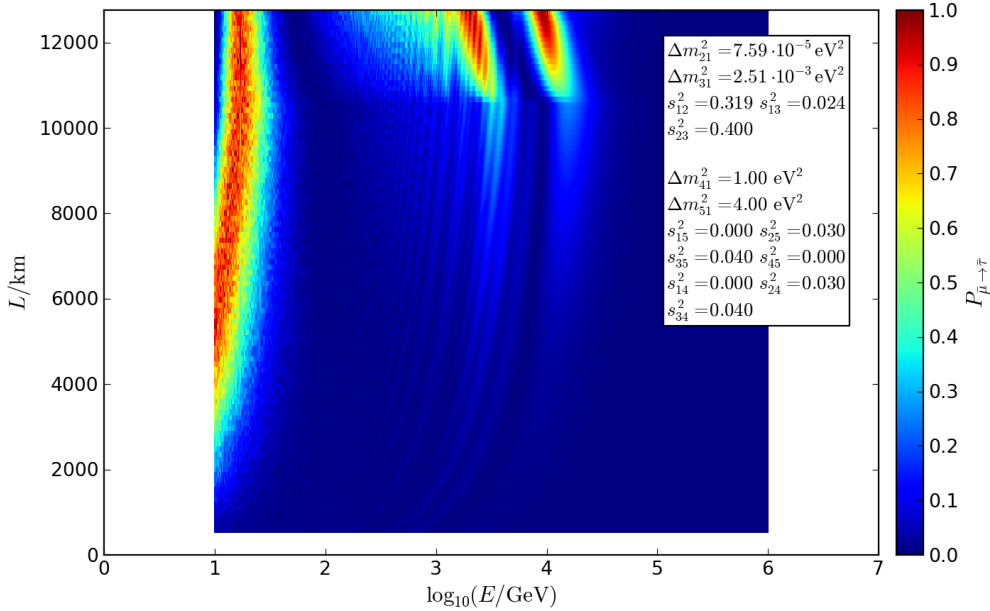


Figure B.21: Probability $P_{\bar{\mu} \rightarrow \bar{\tau}}$ for a muon antineutrino generated in the atmosphere to reach the detector as a tau antineutrino. L is the path length through the Earth (s. fig. 2.2), E is the neutrino energy.

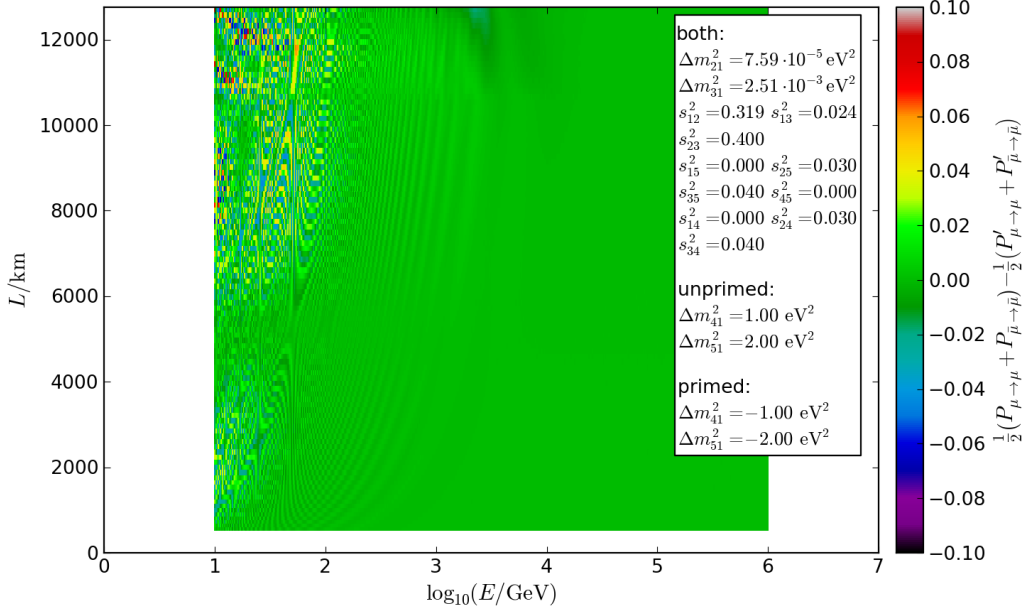


Figure B.22: Difference $\frac{1}{2}(P_{\mu \rightarrow \mu} + P_{\bar{\mu} \rightarrow \bar{\mu}}) - \frac{1}{2}(P'_{\mu \rightarrow \mu} + P'_{\bar{\mu} \rightarrow \bar{\mu}})$ between the probabilities, averaged over muon neutrinos and antineutrinos, for a particle generated in the atmosphere to reach the detector in the same state in which it was generated, between $\Delta m_{51}^2, \Delta m_{41}^2 > 0$ (unprimed) and $\Delta m_{51}^2, \Delta m_{41}^2 < 0$ (primed). L is the path length through the Earth (s. fig. 2.2), E is the neutrino energy.

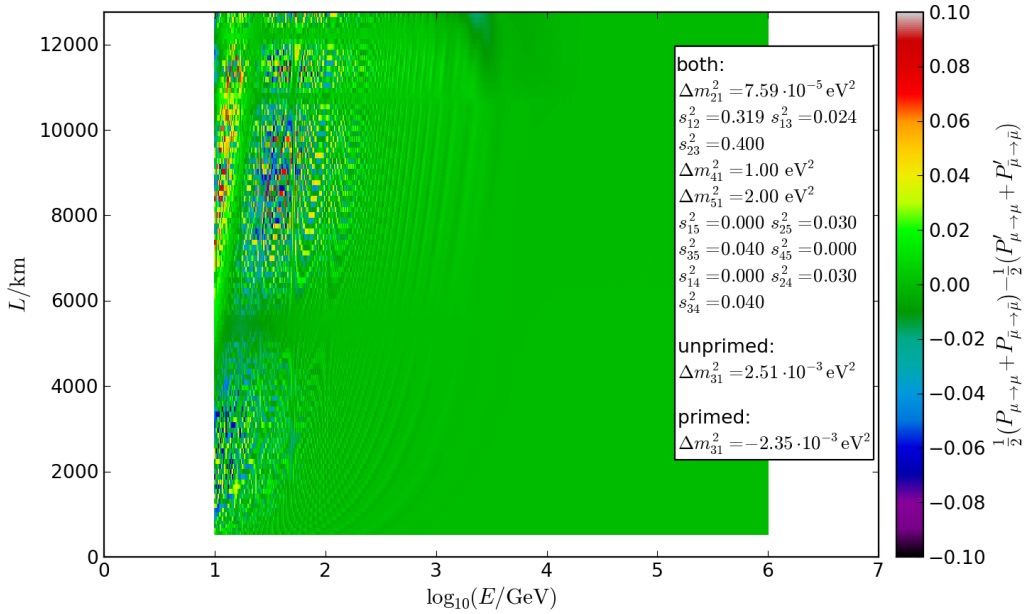


Figure B.23: Difference $\frac{1}{2}(P_{\mu \rightarrow \mu} + P_{\bar{\mu} \rightarrow \bar{\mu}}) - \frac{1}{2}(P'_{\mu \rightarrow \mu} + P'_{\bar{\mu} \rightarrow \bar{\mu}})$ between the probabilities, averaged over muon neutrinos and antineutrinos, for a particle generated in the atmosphere to reach the detector in the same state in which it was generated, between $\Delta m_{32}^2 > 0$ (unprimed) and $\Delta m_{32}^2 < 0$ (primed). L is the path length through the Earth (s. fig. 2.2), E is the neutrino energy.

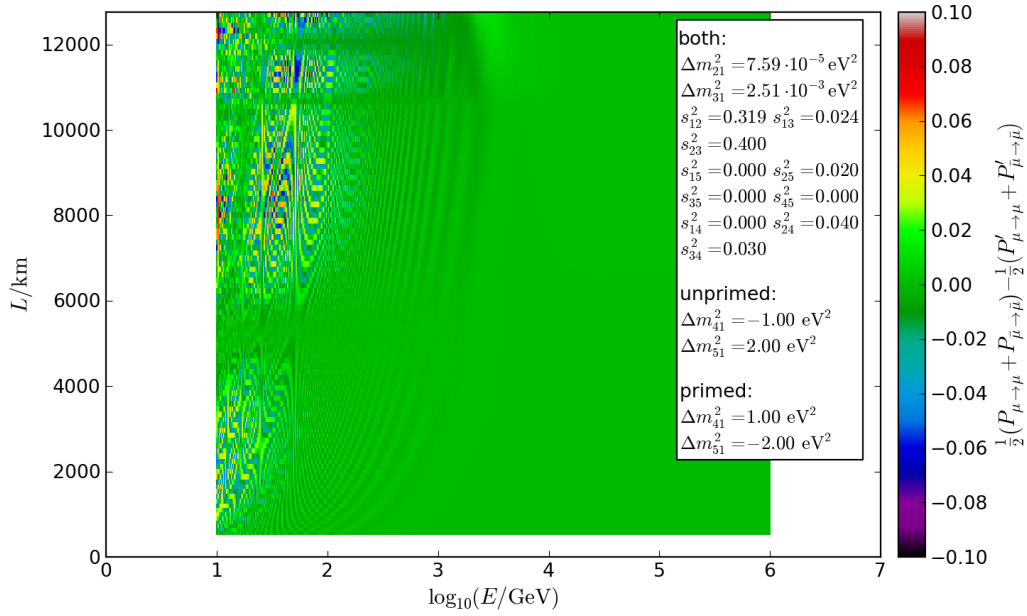


Figure B.24: Difference $\frac{1}{2} (P_{\mu \rightarrow \mu} + P_{\bar{\mu} \rightarrow \bar{\mu}}) - \frac{1}{2} (P'_{\mu \rightarrow \mu} + P'_{\bar{\mu} \rightarrow \bar{\mu}})$ between the probabilities, averaged over muon neutrinos and antineutrinos, for a particle generated in the atmosphere to reach the detector in the same state in which it was generated, between $\Delta m_{41}^2 < 0$, $\Delta m_{51}^2 > 0$ (unprimed) and $\Delta m_{41}^2 > 0$, $\Delta m_{51}^2 < 0$ (primed). L is the path length through the Earth (s. fig. 2.2), E is the neutrino energy.

Bibliography

- [1] Nakamura, K. *et al.* (Particle Data Group): “Review of Particle Physics”. *J. Phys. G*, vol. 37(075021), **2010**. and 2011 partial update for the 2012 edition.
- [2] Fritzsche, H. and Xing, Z.-z.: “Parametrization of flavor mixing in the standard model”. *Phys. Rev. D*, vol. 57(1), **1998**. doi:10.1103/PhysRevD.57.594.
- [3] Gaisser, T. K.: *Cosmic Rays and Particle Physics*. Cambridge Univ. Press, Cambridge, **1990**.
- [4] Kuo, T. K. and Pantaleone, J.: “Neutrino oscillation in matter”. *Review of Modern Physics*, vol. 61(4), **1989**. doi:10.1103/RevModPhys.61.937.
- [5] Choubey, S.: “Signature of sterile species in atmospheric neutrino data at neutrino telescopes”. *JHEP*, vol. 0712, p. 014, **2007**. doi:10.1088/1126-6708/2007/12/014.
- [6] Abazajian, K., Acero, M., Agarwalla, S., Aguilar-Arevalo, A., Albright, C. *et al.*: “Light Sterile Neutrinos: A White Paper”, **2012**. arXiv:1204.5379v1 [hep-ph].
- [7] Beringer, J. *et al.* (Particle Data Group): “Review of Particle Physics”. *Phys. Rev. D*, vol. 86(01001), **2012**.
- [8] Dziewonski, A. M. and Anderson, D. L.: “Preliminary reference Earth model”. *Physics of the Earth and Planetary Interiors*, vol. 25(4), pp. 297 – 356, **1981**. ISSN 0031-9201. doi:10.1016/0031-9201(81)90046-7.
URL <http://www.sciencedirect.com/science/article/pii/0031920181900467>
- [9] Bahlburg, H. and Breitzkreuz, C.: *Grundlagen der Geologie*. Elsevier GmbH, Spektrum Akademischer Verlag, **2004**.
- [10] Website. http://geophysics.ou.edu/solid_earth/prem.html; besucht am 26. Juli 2012 um 11 Uhr 17.
- [11] Ascher, D., Dubois, P. F., Hinsen, K., Hugunin, J., Oliphant, T. *et al.*: “NumPy: Scientific computing with Python”, **1995**–.
URL <http://www.numpy.org/>
- [12] Jones, E., Oliphant, T., Peterson, P. *et al.*: “SciPy: Open source scientific tools for Python”, **2001**–.
URL <http://www.scipy.org/>
- [13] Brown, P. N., Byrne, G. D., and Hindmarsh, A. C.: “VODE: a variable-coefficient ODE solver”. *SIAM J. Sci. Stat. Comput.*, vol. 10(5), pp. 1038–1051, **September 1989**. ISSN 0196-5204. doi:10.1137/0910062.
URL <http://dx.doi.org/10.1137/0910062>

- [14] Argüelles, C. A. and Kopp, J.: “Sterile neutrinos and indirect dark matter searches in IceCube”. *Journal of Cosmology and Astroparticle Physics*, vol. 2012(07), p. 016, **2012**.
URL <http://stacks.iop.org/1475-7516/2012/i=07/a=016>
- [15] Gaisser, T. K. and Stanev, T.: “Path length distributions of atmospheric neutrinos”. *Phys. Rev. D*, vol. 57, pp. 1977–1982, **Feb 1998**. doi:10.1103/PhysRevD.57.1977.
URL <http://link.aps.org/doi/10.1103/PhysRevD.57.1977>
- [16] Razzaque, S. and Smirnov, A. Y.: “Searches for sterile neutrinos with IceCube Deep-Core”. *Phys. Rev. D*, vol. 85, p. 093010, **May 2012**. doi:10.1103/PhysRevD.85.093010.
URL <http://link.aps.org/doi/10.1103/PhysRevD.85.093010>
- [17] Akhmedov, E., Razzaque, S., and Smirnov, A.: “Mass hierarchy, 2-3 mixing and CP-phase with huge atmospheric neutrino detectors”. *Journal of High Energy Physics*, vol. 2013, pp. 1–34, **2013**. doi:10.1007/JHEP02(2013)082.
URL <http://dx.doi.org/10.1007/JHEP02%282013%29082>
- [18] Akhmedov, E. K., Maltoni, M., and Smirnov, A. Y.: “Neutrino oscillograms of the Earth: effects of 1-2 mixing and CP-violation”. *Journal of High Energy Physics*, vol. 2008(06), p. 072, **2008**.
URL <http://stacks.iop.org/1126-6708/2008/i=06/a=072>
- [19] Nakamura, K. *et al.* (Particle Data Group): “Review of Particle Physics”. *J. Phys. G*, vol. 37(075021), **2010**.
- [20] An, F. *et al.*: “Observation of electron-antineutrino disappearance at Daya Bay”. *Phys.Rev.Lett.*, vol. 108, p. 171803, **2012**. doi:10.1103/PhysRevLett.108.171803.
- [21] BenTov, Y. and Zee, A.: “The Neutrino mixing matrix could (almost) be diagonal with entries ± 1 ”. *Phys.Lett.*, vol. B714, pp. 80–84, **2012**. doi:10.1016/j.physletb.2012.06.060.
- [22] Jain, A. K., Figueiredo, M., and Zerubia, J.: *Energy Minimization Methods in Computer Vision and Pattern Recognition*. Springer, **2001**.
- [23] Komatsu, E. *et al.*: “Seven-Year Wilkinson Microwave Anisotropy Probe (WMAP) Observations: Cosmological Interpretation”. *Astrophys.J.Suppl.*, vol. 192, p. 18, **2011**. doi:10.1088/0067-0049/192/2/18.
- [24] Razzaque, S. and Smirnov, A. Y.: “Searches for sterile neutrinos with IceCube Deep-Core”. *Phys.Rev.*, vol. D85, p. 093010, **2012**. doi:10.1103/PhysRevD.85.093010.